

The Spin Structure of the Neutron^{*}

Steven T. Churchwell

Stanford Linear Accelerator Center
Stanford University
Stanford, CA 94309

SLAC-Report-673
February 1998

Prepared for the Department of Energy
under contract number DE-AC03-76SF00515

Printed in the United States of America. Available from the National Technical Information Service, U.S. Department of Commerce, 5285 Port Royal Road, Springfield, VA 22161.

^{*} Ph.D. thesis, University of Massachusetts Amherst, Amherst, MA 01003.

THE SPIN STRUCTURE OF THE NEUTRON

A Dissertation Presented

by

STEVEN T. CHURCHWELL

Submitted to the Graduate School of the
University of Massachusetts Amherst in partial fulfillment
of the requirements for the degree of

DOCTOR OF PHILOSOPHY

February 1998

Department of Physics and Astronomy

THE SPIN STRUCTURE OF THE NEUTRON

A Dissertation Presented

by

STEVEN T. CHURCHWELL

Approved as to style and content:

Gerald A. Peterson, Chair

Ross S. Hicks

John F. Dubach

Michael F. Skrutskie

John F. Donoghue, Department Head
Department of Physics and Astronomy

ACKNOWLEDGMENTS

The experiment described in this thesis was the collaborative achievement of a great many people. I would like to thank each and every member of the E154 collaboration for helping to make the experiment a success. In addition, thanks go to the SLAC operators and technicians without whom the experiment could never have run. I thank the spokesperson, Emlyn Hughes, for allowing me to join the collaboration. Finally, I am deeply indebted to my fellow graduate students in the collaboration for making the experiment and analysis run smoothly, for the many fruitful discussions about a wide variety of topics, and for general companionship.

I am also very grateful for all the support and assistance I have received from members of the UMass Nuclear Physics Group. I would like to extend extra special thanks to my advisor, Gerry Peterson, for all he has done to help get me to this point in my career.

I could never have finished writing this thesis without the assistance of my family. I thank Monique Knaggs in particular, for helping to proofread the document and providing me with all the time needed for writing. I dedicate this work to my daughter Astrid for showing me the joy of life, and giving me the added incentive necessary to complete this thesis.

ABSTRACT

THE SPIN STRUCTURE OF THE NEUTRON

FEBRUARY 1998

STEVEN T. CHURCHWELL

B.A., EARLHAM COLLEGE

M.A., UNIVERSITY OF MASSACHUSETTS AMHERST

Ph.D., UNIVERSITY OF MASSACHUSETTS AMHERST

Directed by: Professor Gerald A. Peterson

A description of SLAC experiment E154, a precision measurement of the neutron's longitudinal spin structure function g_1^n , is presented. Deep inelastic electron scattering was used to measure the structure function in the kinematic range $0.014 < x < 0.7$, and $1 < Q^2 < 17 \text{ GeV}^2$. A measurement of the transverse spin structure function g_2^n was also made, but with significantly lower statistical precision. Electrons with an average polarization of $82 \pm 2\%$ and an energy of 48.3 GeV were scattered off polarized ^3He nuclei having an average polarization of 38%. Two independent magnetic spectrometers set at scattering angles of 2.75° and 5.5° were used to acquire about 100 million events during a two month run in late 1995. The data were analyzed to yield the integral over the measured region: $\int_{0.014}^{0.7} g_1^n(x) dx = -0.036 \pm 0.004(\text{stat}) \pm 0.005(\text{syst})$, which is several standard deviations below the Ellis-Jaffe sum rule predictions. When these data were combined with the proton g_1^p structure function data from the SMC and E143 experiments, the Bjorken sum rule over the measured x range was found to be within 10% of the predicted value. The integral of the g_2^n data, dominated by the statistical uncertainty, was found to be $\int_{0.014}^{0.7} g_2^n(x) dx = 0.19 \pm 0.17(\text{stat}) \pm 0.02(\text{syst})$, in agreement with the Burkhardt-Cottingham sum rule prediction. The g_1^n structure function data at low x were found to be inconsistent with the traditional asymptotic forms, bringing into question the methods used in the past.

TABLE OF CONTENTS

	<u>PAGE</u>
ACKNOWLEDGMENTS	iv
ABSTRACT	v
LIST OF TABLES	x
LIST OF FIGURES	xii
 CHAPTER	
1. INTRODUCTION	1
1.1 The Quark-Parton Model	3
1.2 General Fixed Target Scattering	5
1.2.1 Cross Section	6
1.3 Deep Inelastic Scattering	7
1.4 Bjorken x	7
1.5 Scaling	8
1.6 Sum Rules	8
1.7 Open Questions	9
1.8 Experiment E154	9
 2. SPIN STRUCTURE	 10
2.1 Electron Scattering	10
2.1.1 Virtual Photon Absorption	15
2.1.2 The Asymmetries	17
2.1.3 Cross Sections using F_1 , F_2 , g_1 , and g_2	19
2.1.4 Scaling Behavior of the Structure Functions	20
2.1.5 Interpretations of the Structure Functions	22
2.2 Q^2 Evolution	23
2.3 Sum Rules	25
2.3.1 The Bjorken Sum Rule	25

2.3.2	The Ellis-Jaffe Sum Rule	27
2.3.3	The Burkhardt-Cottingham Sum Rule	28
2.4	Measuring the Structure Functions	29
2.5	Neutron Targets	31
2.6	Status of Experiments	33
3.	THE SLAC 50 GEV BEAM	36
3.1	Introduction	36
3.1.1	Accelerator Operation	37
3.2	Polarized Source	37
3.3	The SLAC Accelerator	40
3.4	The A-line	42
3.4.1	Synchrotron Radiation Energy Loss	43
3.4.2	Spin Precession and Beam Energy	44
3.4.3	Quadrupole Magnets	46
3.5	Beam Line Optics Calculations	47
3.6	A-Line Optics During E154	51
3.7	Beam Monitoring and Systematics	55
3.7.1	Beam Monitors	56
3.7.1.1	Bad Spill Monitor	56
3.7.1.2	Good Spill Monitor	57
3.7.1.3	Lead-Glass Monitor	58
3.7.1.4	Wire Array Monitor	59
3.7.1.5	Analysis of Wire Array Data	60
3.7.1.6	Toroids	62
3.8	Møller Polarimeter	62
3.8.1	Theory of Møller Scattering	63
3.8.2	Physical Layout	64
3.8.3	Møller Target	66
3.8.4	Møller Detector	68
3.8.5	Møller Data and Analysis	69
3.8.5.1	Averaging Runs	73
3.8.6	Sign of the Beam Polarization	73
3.8.7	Energy Scan	74
3.8.8	Source Laser Wavelength Scan	74
3.8.9	Møller Results and Uncertainties	75

4. THE E154 EXPERIMENT	78
4.1 The E154 Polarized Target	78
4.1.1 Polarizing ^3He	80
4.1.2 Measuring the ^3He Polarization	84
4.1.2.1 Problems Achieving High Polarization	86
4.1.3 Polarization History	87
4.1.4 The Exploding Target Problem	87
4.2 The Dilution Factor	89
4.2.1 Dilution Factor Model	89
4.2.2 Radiative Corrections	91
4.2.3 Experimental Measurement of the Dilution Factor	92
4.2.4 Dilution Factor Error Analysis	93
4.3 E154 Spectrometers	93
4.3.1 Magnetic Optics of the Spectrometers	102
4.3.1.1 The 2.75° Spectrometer Optics	102
4.3.1.2 The 5.5° Spectrometer Optics	103
4.4 Detector Systems	104
4.4.1 Čerenkov Detectors	104
4.4.1.1 Čerenkov Detector Operation	105
4.4.1.2 Wavelength Shifters	106
4.4.1.3 Čerenkov Electronics	106
4.4.2 Hodoscopes	106
4.4.3 Lead Glass Shower Counter Arrays	108
4.5 Spectrometer Electronics	109
4.5.1 Trigger Electronics	112
4.6 Data Acquisition Systems	113
4.6.1 Checkpoints	114
4.6.2 Data Rates	115
4.6.3 Data Storage	116
5. DATA ANALYSIS	117
5.1 Outline	117
5.2 Raw Data Analysis	118
5.2.1 Čerenkov Analysis	119

5.2.1.1	Čerenkov Timing Error	120
5.2.1.2	Čerenkov Pulse-Height Timing Correction	121
5.2.1.3	Time-of-Flight Timing Correction	122
5.2.2	Hodoscope Analysis	122
5.2.3	Shower Counter Analysis	123
5.2.3.1	Cells and Energy Sharing	123
5.2.3.2	Building Shower Clusters	125
5.2.4	Shower Counter Neural Network	127
5.2.4.1	Timing Correction for Shower Energies	128
5.2.5	Tracking	129
5.2.6	Tracking Performance	134
5.3	Data Summary Tape Production	135
5.3.1	Run Selection for the Asymmetries	137
5.3.2	Beam Cuts	138
5.3.3	Electron Definitions	139
5.4	Asymmetry Corrections	141
5.4.1	Pion Asymmetry	141
5.4.2	Positron Asymmetry	142
5.4.3	Dead-Time Corrections	143
5.4.4	Electroweak Correction	143
5.4.5	Radiative Corrections	144
5.5	Systematic Studies	147
5.6	Combining Runs	147
5.7	The Neutron Structure Functions	148
6.	INTERPRETATIONS	153
6.1	Q^2 Evolution	153
6.2	The $x \rightarrow 1$ Extrapolation	154
6.3	The $x \rightarrow 0$ Extrapolation	155
6.4	Sum Rule Results	157
6.4.1	Comparison to the Ellis-Jaffe Sum Rule	157
6.4.2	Comparison to the Bjorken Sum Rule	158
6.4.3	Comparison to the Burkhardt-Cottingham Sum Rule	160
6.5	Spin Decomposition of the Neutron	160
6.6	Determining α_s	161
6.7	Conclusions	162
6.8	The Future	163

APPENDIX: RUNS USED IN THE ANALYSIS 165
BIBLIOGRAPHY 170

LIST OF TABLES

1.1	The six quarks, and some of their properties	3
2.1	Parameters for the 15 parameter fit to $F_2(x)$	31
2.2	The DIS spin structure function experiments, with kinematic ranges, and structure functions measured. The superscript d refers to the deuteron, and the dates are for publication times.	34
3.1	Magic beam energies for which the electron polarization is longitudinal in ESA, and the corresponding beam energy when synchrotron energy losses are taken into account.	46
3.2	A-line quadrupole magnet fields as a function of run number. All units are kG·m/m. The breaks in the run numbers correspond to unanalyzed special runs.	54
3.3	Møller target foil parameters	67
3.4	Uncertainties contributing to the Møller measurement of the beam polarization.	76
3.5	Run ranges during which the beam and source characteristics were reasonably stable. The average polarization from the Møller measurements taken in each range are shown with statistical uncertainties only.	76
4.1	Target cell dimensions in mm. ‘OD’ refers to the outer diameter, ‘Wall’ is the wall thickness of the main target cell tube, the ‘Start’ column under ‘Flare’ measures the distance from the center of the cell to the start of the flare, and the two lengths under ‘Pumping Cell’, ‘L.1’ and ‘L.2’, refer to the length of the straight part of the pumping cell wall, and the total length, respectively.	81
4.2	Target cell usage during E154. The upper entries are for the polarized ^3He cells, and the lower four entries list the corresponding reference cells.	82

4.3	The dilution factor f : results and uncertainties for the 2.75° spectrometer.	94
4.4	The dilution factor f : results and uncertainties for the 5.5° spectrometer.	95
5.1	Track classes: all definitions include hodoscope hits.	130
5.2	Beam cuts for the asymmetry determination. The units for the good and bad spill are ADC counts, the units for the toroids are 10^{10} electrons/spill, and the units for the wire array are mm. The only cuts of any real significance were the toroid cuts, which eliminated the witness pulses.	140
5.3	Radiative corrections and errors to both the parallel and perpendicular asymmetries for the two E154 spectrometers. Values in all columns except the first are multiplied by 100.	146
5.4	The neutron A_1 and A_2 asymmetries with statistical and systematic errors for the combined spectrometers at measured Q^2 (assuming no Q^2 dependence).	149
5.5	The neutron g_1 and g_2 structure functions with statistical and systematic errors for the combined spectrometers at measured Q^2 (assuming no Q^2 dependence).	149
6.1	The neutron structure function g_1 with statistical and systematic errors for the combined spectrometers evolved to $Q^2 = 5 \text{ GeV}^2$ assuming g_1^n/F_1^n is independent of Q^2	154
A.2	Runs used for the asymmetry analysis from target DAVE	165
A.3	Runs used for the asymmetry analysis from target RIKER	165
A.4	Runs used for the asymmetry analysis from target BOB	166
A.5	Runs used for the asymmetry analysis from target SMC.	166
A.6	Runs used for the asymmetry analysis from target GENERALS.	167
A.7	Runs used for the asymmetry analysis from target HERMES.	167
A.8	Runs used for the asymmetry analysis from target PRELIMS.	168
A.9	Runs used for the asymmetry analysis from target CHANCE.	168
A.10	Runs used for the asymmetry analysis from target PICARD.	169
A.11	Runs used for measuring the positron background with the spectrometer magnet currents reversed. The target was PICARD.	169
A.12	Runs used for measuring A_\perp . The target was PICARD.	169

LIST OF FIGURES

1.1	Schematic of a fixed target scattering experiment.	5
2.1	Feynman diagram for one photon exchange deep inelastic electron scattering. The incident (scattered) electron, shown as the upper lines, carries four-momentum k^μ (k'^μ) and spin s^μ (s'^μ). The target, shown as the lower lines, enters with four-momentum P^μ and spin S^μ , and after the scattering exits as some unknown state of X hadrons. The interaction proceeds via a single photon exchange, shown as the wavy line, which transfers four-momentum q^μ to the target.	11
2.2	World results on $xg_1^n(x)$ before E154	35
3.1	The Stanford Linear Accelerator Center (not to scale). Electrons are generated in the source on the left side of the figure, accelerated in the 2 mile linac (straight portion), then steered through the Beam Switch Yard (BSY) into one of the experimental areas. The hexagonal 'ring' is being upgraded to become the SLAC B-factory, and the Stanford Linear Collider experiment hall is labeled as SLC. E154 used the larger of the two end stations, ESA.	36
3.2	The SLAC polarized electron source laser system	38
3.3	The pseudo random bit generator schematic. Arrows show the direction of information flow. The upper set of squares represents a 33-bit shift register, and the lower symbol is an exclusive 'OR' logic gate.	40
3.4	Schematic (not to scale) of the A-line magnetic elements. Several small magnets between the accelerator and Q10 are not shown, including the pulsed magnets which add a $1/2^\circ$ bend. Only the momentum-defining slits, SL10, are shown. The quadrupoles Q30 and Q38 were not used during most of E154.	42
3.5	Beam x - y cross-sections (spots) at the roller screens, the target and the wire array generated by TURTLE using $\delta = 0.1\%$. Dimensions are in mm.	51

3.6	Beam x - y cross-sections (spots) at the roller screens, the target and the wire array generated by TURTLE using $\delta = 0.5\%$. Dimensions are in mm.	52
3.7	Beam x - y cross sections (spots) and correlations between input momenta and target coordinates generated by TURTLE using $\delta = 1.0\%$. Dimensions are in mm for the X and Y coordinates, and 0.1% for the momentum coordinate.	53
3.8	Results from the Q41 quadrupole field scan of runs 3385-3390. The two curves are the TRANSPORT results, with the lower curve having an input emittance in x half as large as the upper curve. The X's are the beam 'widths,' or spatial extent (in \hat{x}) measured with the wire array.	55
3.9	Typical data from the x (left figure) and y (right figure) wire arrays for a small spot with the MINUIT fit superimposed.	61
3.10	The Møller system viewed from the side. The vertical dimension is shown scaled by a factor of 200 larger than the horizontal dimension for clarity. The gray bands show the scattering angle acceptances for Møller electrons in the laboratory reference frame.	65
3.11	The Møller system viewed from above. The vertical dimension is expanded by a factor of ten compared to the horizontal dimension. The scattering angle values shown are for the center-of-mass reference frame.	66
3.12	The Møller Detector Package. The main beam line is shown as the circle on the right. The gray band labeled 'Møller stripe' in the figure is the region where elastically scattered Møller electrons are expected after being deflected to the left by the Møller magnet. There is a symmetrically placed stripe below the beam axis for scattering 'down' rather than 'up'. The upper and lower detectors are clearly visible, including the actuator for moving the upper silicon pad detector array horizontally.	70
3.13	Møller data showing the sum of right and left helicities for run number 3349. The top figure corresponds to the upper Møller detector, and the four lower figures show data from the four lower detectors. In each instance, larger scattering angles are to the left.	71
3.14	Møller data showing the difference between right and left beam helicity count rates for run number 3349.	72
3.15	Beam polarization vs. beam energy in ESA. The parameters of the fit are described in the text.	75

3.16	Beam polarization in percent vs. run number. The straight horizontal lines show averages for run ranges over which the beam characteristics were similar.	77
4.1	The E154 polarized ^3He target system.	79
4.2	A polarized ^3He target cell (Picard). All dimensions are in mm. Other cells were very similar in size and shape. Relevant dimensions for all cells used are listed in Table 4.1.	80
4.3	Rubidium energy levels.	83
4.4	'Spin-up' of target cell 'Picard'.	84
4.5	Target polarizations as a function of run number. As can be seen, the majority of runs had positive polarizations corresponding to the ^3He magnetic moment pointing downstream in the beam line. Most of the 'spin-ups' are not very obvious, because no data runs were taken on the polarized target cells until the polarization reached a reasonable value.	87
4.6	Dilution factors for targets 'Dave', 'Riker', and 'Bob'. Dilution factors for the 2.75° spectrometer are shown in the left column and for the 5.5° spectrometer in the right.	96
4.7	Dilution factors for targets 'SMC', 'Generals', and 'Hermes'. Dilution factors for the 2.75° spectrometer are shown in the left column and for the 5.5° spectrometer in the right.	97
4.8	Dilution factors for target cells 'Prelims', 'Chance', and 'Picard'. Dilution factors for the 2.75° spectrometer are shown in the left column and for the 5.5° spectrometer in the right.	98
4.9	The E154 spectrometers.	100
4.10	The x and Q^2 coverage of the two E154 spectrometers for an incident beam energy of 48.3 GeV.	101
4.11	A schematic of the detector systems for the 2.75° spectrometer. The scale is in meters, measured from the target position.	107
4.12	Arrangement of the shower counter blocks shown with the spectrometer coordinate system axes. Particles entered the detector from the left, traveling in the \hat{z} direction, and the phototubes (not shown) were on the downstream end of the blocks. The numbering of the blocks in 'block coordinates' is shown by the coordinate pairs for three of the corner blocks.	109

4.13	E154 electronics schematic for the 2.75° spectrometer branch. . . .	111
4.14	E154 trigger electronics schematic	113
5.1	Typical Čerenkov waveform. The left axis is in units of FADC ‘voltage’ which is roughly equivalent to mV. The horizontal axis is the time into the spill, and has units of ns.	119
5.2	Sketch of a typical signal from a shower counter block as a function of time. The discriminator thresholds for three levels are shown along with the corresponding Δt measurements. The ‘overshoot’ above ground at the end of the pulse is also shown. The vertical arrow shows where the end of the ADC integration window (gate) occurs. For shower signals which happen later in the spill, less charge will be subtracted from the integral of the charge due to the overshoot, because the signal will spend less time above ground before the end of the measurement window.	124
5.3	Beam’s view of the central nine blocks of a cluster, surrounded by the sixteen ‘second corona’ blocks (shaded).	127
5.4	E/P as a function of time in the spill for the 2.75° spectrometer (left) and the 5.5° spectrometer (right). Values are taken from run 2480. The error bars show the standard deviation of each E/P distribution, and were not utilized in making the fits.	129
5.5	Examples of hodoscope ‘mini-clusters’ in the tracking system. . . .	131
5.6	The neutron structure function determined from data where the target spin direction was downstream (forward) compared with the same determination from data where the target spin direction was pointing upstream.	150
5.7	The neutron A_1 asymmetry. The error bars are statistical only, and the gray band at the bottom represents the size of the systematic uncertainty.	151
5.8	The neutron structure function $xg_1(x)$. The error bars are statistical only, and the gray band at the bottom represents the size of the systematic uncertainty.	152
6.1	The low x extrapolations of the E154 data. Data from the SMC experiments are also plotted to show the trend of the world measurements at lower x	157

6.2	The integral of the neutron $g_1^n(x)$ structure function measurements as a function of x . Each plotted value is the integral from x to 1 of the measured data (with the extrapolation to $x = 1$ included). . . .	158
6.3	The integral of the difference between the neutron $g_1^n(x)$ and the proton $g_1^p(x)$ structure function measurements as a function of x . Each plotted value is the integral from that x to 1 of the measured data (with the extrapolation to $x = 1$ included). The proton data are from SLAC experiment E143, and the CERN SMC experiment for the low x values.	159
6.4	The neutron A_2 asymmetry, with the square root of R limit shown as the solid line.	161
6.5	The neutron g_2^n structure function data measured in E154. The g_2^{WW} parameterization shown is calculated from the E154 g_1^n data.	162

CHAPTER 1

INTRODUCTION

During the past century, the best description of how the physical world around us is constructed has changed dramatically. The myriad forms of matter are now viewed as a conglomeration of atoms from the roughly 100 known elements. Each of these atoms in turn is known to be constructed out of three smaller objects called protons, neutrons, and electrons. In the past 30 years remarkable progress has been made in understanding how protons and neutrons themselves are constructed from yet smaller building blocks known as quarks.

Quarks were first postulated by Gell-Mann [1] in 1965 to describe the baryon octet of particles. In 1969 several predictions were published [2], describing an expected ‘scaling’ of the nucleon structure functions in Deep Inelastic Scattering (DIS) analogous to the anomalies observed by Rutherford for alpha particles scattering off gold atoms. As Rutherford’s experiment provided the first evidence for substructure in atoms, the experimental verification of the scaling predictions [3, 4] was the first direct evidence for substructure in the nucleons. These early experiments launched a long series of deep inelastic scattering experiments of which the experiment described in this thesis is a continuation.

The early DIS experiments were carried out at the Stanford Linear Accelerator Center (SLAC), and used electron beams to probe the substructure of protons and neutrons, collectively called nucleons. These experiments used unpolarized targets and beams, and measured the spin-averaged cross sections. In 1976, the first results

from a deep inelastic electron scattering experiment using both a polarized beam and a polarized target were published [5], allowing experimental access for the first time to the spin structure of the proton. This provided a complementary picture of the inner workings of the nucleons relative to the unpolarized quark structure, and proved to be a powerful tool for checking theoretical predictions.

The first two experiments using polarized electrons and polarized targets [5, 6] measured the spin structure functions over a relatively small kinematic range by today's standards, and found no significant violations of the standard quark model predictions. However, in 1988 the European Muon Collaboration (EMC) published results from polarized deep inelastic muon scattering off protons at CERN (originally Conseil Europeen pour la Recherche Nucleaire - now the European Laboratory for Particle Physics) which led to the stunning conclusion that only about 20% of the spin of the proton could be attributed to the constituent quarks [7]. This was termed the 'spin crisis', and caused considerable debate about where the spin of the nucleons originated. In addition, two theoretical predictions based on some of the fundamentals of the standard model appeared to be violated. These were the Bjorken sum rule [8], and the Ellis-Jaffe sum rule [9].

During the past nine years since the EMC results were published, many experiments have been performed, both at CERN using polarized muons, and at SLAC using polarized electrons. A third laboratory, the Deutsches Elektronen Synchrotron (DESY), is now probing the spin structure of the nucleons using positron beams with internal gas jet targets in the HERA storage ring. The DESY experiment is named HERMES, and the first results from it have recently been published [10]. These experiments have mapped out the spin structure functions of the proton and neutron in great detail over very broad kinematic ranges. Interpreting these data, one finds that the constituent u , d , (and s) quarks only contribute about $28(\pm 16)\%$ of the spin [11]. There is a large negative contribution of about $-10(\pm 5)\%$ from

Table 1.1. The six quarks, and some of their properties

Flavor	Electric Charge	Bare Mass [MeV]
up	+2/3	5
down	-1/3	10
charm	+2/3	1,300
strange	-1/3	200
top	+2/3	180,000
bottom	-1/3	4,300

the strange quarks – the ‘strange sea’, and gluons, which mediate the strong forces between quarks, might contribute as much as 50% or more of the total spin [11].

1.1 The Quark-Parton Model

The quark-parton model describes matter in terms of quarks and gluons. It is a part of the Standard Model, and interprets the fundamental fields of Quantum Chromodynamics (QCD), the theory describing the strong interaction, as quarks and gluons. There are now six known quarks [12] which are listed with some of their properties in Table 1.1. An additional six anti-quarks with opposite values for electric charge also exist. Quarks, however, are not the only subnucleonic denizens. Also present are gluons which mediate the strong ‘color’ force between quarks. Gluons are spin-1 particles carrying one unit of color, the strong force analogue to electric charge in the electromagnetic force. Gluons come in three ‘colors’ which add together in vector fashion to form a ‘colorless’ object, such as a proton or neutron. All observable particles must be colorless due to the principle of quark confinement, which states that the strong force increases in strength as the separation between colored objects increases, to the point where it is energetically cheaper to produce a quark anti-quark pair than to allow the particles to separate further. Thus, unless an object has no color so it cannot feel the color force, it cannot be found alone, explaining why free quarks have never been found.

The picture of nucleons as composed of quarks and gluons is complicated still further by the addition of the other fundamental forces of nature to the theory. Each force is mediated by one or more gauge bosons. The electromagnetic force is mediated by photons which are certainly present in the nucleon, since the constituent quarks are charged objects. The weak nuclear force is mediated by three particles known as the W^\pm and the Z^0 . Unlike photons, these particles have large masses, and are hence less likely to be created by quantum fluctuations. With masses of about 81 GeV and 92 GeV, these particles can in general be neglected for momentum transfers which are significantly smaller, as is the case in most of the DIS experiments discussed here. A notable exception occurs in parity violating experiments because the parity violation is exclusively due to the weak nuclear force. The fourth force, gravity, is completely negligible at the scale of these experiments, being about 10^{40} times weaker than the strong color force.

QCD specifies the equations which describe how protons and neutrons are constructed and held together as particles; however, these equations have not been solved yet. Approximations may be made, such as considering only large momentum transfers where the strong coupling constant becomes small enough, due to asymptotic freedom, for perturbation theory - perturbative QCD or pQCD - to work. Asymptotic freedom is the opposite extreme from quark confinement. At very short distances, or equivalently, very high energies, the color force becomes relatively weak, allowing many of the traditional calculational approaches of Quantum Electrodynamics to work.

In recent years some progress has been made in solving the equations of QCD by computer using a lattice approach to space-time. There is a well developed formalism for these lattice calculations; however, they are not yet at a level where they can be used to predict the nucleon structure functions. Most contemporary lattice calculations use a lattice of about 50 to 100 points in each of the four space-

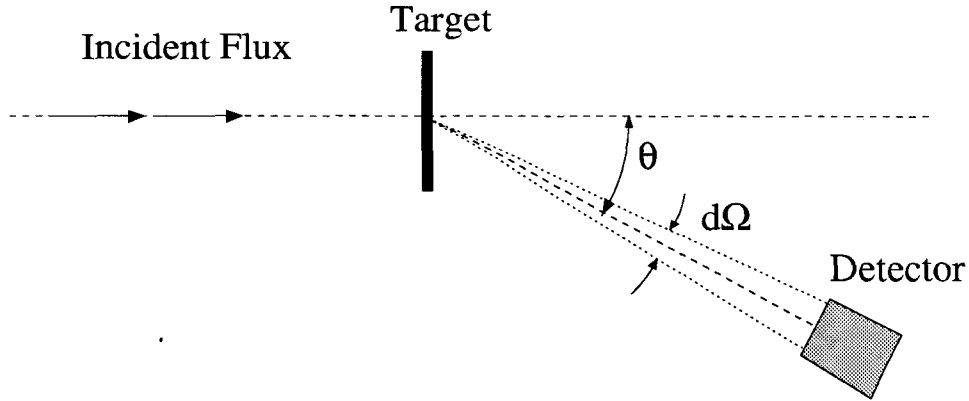


Figure 1.1. Schematic of a fixed target scattering experiment.

time dimensions, which simply is not enough to truly describe an extended object such as a nucleon [13].

1.2 General Fixed Target Scattering

High-energy particle physics relies heavily on particle scattering to investigate the properties of the subatomic particles. Two major classes of scattering experiments exist: colliding beam and fixed target experiments. Only fixed target experiments will be discussed here. A schematic of a fixed target scattering experiment is shown in Fig. 1.1. As the name suggests, the target being probed is fixed in the laboratory reference frame, and is bombarded by a beam of high energy particles labeled as incident flux in Fig. 1.1. Several types of particle beams may be utilized; however, the experiment described in this thesis used an electron beam exclusively, so the scattering formalism will be developed for electrons specifically.

Electron scattering is well suited for investigating the internal structure of nuclei since the electromagnetic interaction can be considered as completely understood allowing the extraction of structure information from the nucleus in question without concern for the interaction between the probe particle and the target. Also, the electron is, as far as is known, a point particle [14], so the interpretation of the

nuclear structure is much clearer. There are of course caveats to this. The electromagnetic interaction is normally thought of in terms of a perturbative expansion, where the additional terms beyond first order are ‘radiative corrections’ and must be understood. However, radiative corrections can be calculated quite accurately since the fine structure constant α for electrodynamics is small enough that the perturbative series converges quite rapidly. Additionally, the electron interacts with the target through the weak force with the exchange of a Z^0 particle (weak neutral current); however, in most cases of interest, where the Q^2 of the interaction is well below the Z^0 mass, and for non-parity violating experiments (see section 5.4.4), this contribution can be safely ignored [15].

1.2.1 Cross Section

In a typical fixed-target scattering experiment, like the one shown in Fig. 1.1, beam particles which are scattered from the target into a detector encompassing a small solid angle $d\Omega$ around a central scattering angle θ , are counted by the detector. The number of particles $d\mathcal{N}$, reaching the detector per unit time is directly related to the number of beam particles incident on the target through the relation

$$d\mathcal{N} = FN_t \frac{d\sigma(\theta)}{d\Omega} d\Omega, \quad (1.1)$$

where F is the incident flux of particles, N_t is the number of scattering centers in the target intercepted by the beam, and the constant of proportionality, $d\sigma(\theta)/d\Omega$ is defined as the differential scattering cross section [16]. The incident flux is defined as the number of particles crossing a unit area normal to the beam direction per unit time. For a uniform beam containing n_b particles per unit volume moving at velocity v_b relative to the target, the flux is [16]

$$F = n_b v_b. \quad (1.2)$$

Using the covariant normalization condition of $2E$ particles per unit volume V , the factors $FN_t \equiv \Phi$ may be written in an invariant form [17] as

$$\Phi \equiv \frac{1}{4\sqrt{(p_b \cdot p_t)^2 - m_b^2 m_t^2}}, \quad (1.3)$$

where the subscripts b and t refer to the beam and target particles respectively, p is the four-momentum, and m the mass of the particle.

1.3 Deep Inelastic Scattering

Deep inelastic scattering (DIS) refers to electron (or in general any particle) scattering at energies large enough that the energy and momentum transferred to the target nucleus are well beyond any resonances in the nucleon wave functions. In this region, the scattering process may be viewed as an incoherent sum of scatterings from the fundamental constituents, which are assumed to be quarks in the quark-parton model. The individual scatterings off quarks are incoherent because at the high momentum transfers of DIS, which probe extremely short distances, asymptotic freedom reigns, and the quarks effectively do not interact with each other. By contrast, at lower energies corresponding to larger distances of the order of the size of a nucleon and larger, quark confinement takes over and the strong force between the quarks grows extremely large, binding the constituent quarks together to form the more familiar protons and neutrons of nuclei.

1.4 Bjorken x

In discussing DIS, the momentum carried by a specific quark as a fraction of the parent nucleon's momentum will frequently be referred to. This is defined as Bjorken x , and can range from 0 to 1. The expectation value is $1/3$ since a nucleon is made of three quarks, each sharing the momentum. At the extremes, the quark

is carrying either none or all of the nucleon momentum - both options having a low probability. The definition is

$$x \equiv \frac{Q^2}{2M\nu}, \quad (1.4)$$

where Q^2 is the four-momentum transferred squared from the electron to the nucleon squared, M is the mass of the nucleon, and ν is the energy transferred to the nucleon.

1.5 Scaling

As described in Section 1, the prediction and experimental verification of scaling of the structure functions in Deep Inelastic Electron Scattering provided the first evidence for quarks inside the nucleons. The measured structure functions describe how the nucleons react to electromagnetic probes, and in general depend on both x and Q^2 . ‘Scaling’ refers to the way these structure functions become functions of x alone at large Q^2 . Scaling is now known to be violated, but in a very specific way, described by the Gribov-Lipatov-Altarelli-Parisi (GLAP) Q^2 evolution equations [18].

1.6 Sum Rules

Over the years several ‘sum rules’ have been developed. These are theoretical predictions relating integrals of the structure functions to other observable quantities. Of current interest with regard to the spin structure in the nucleons are the Bjorken sum rule [8], the Ellis-Jaffe sum rule [9], and the Burkhardt-Cottingham sum rule [19], each of which will be discussed in section 2.3.

1.7 Open Questions

With such blatant violations of well founded theoretical predictions as were observed by the EMC and succeeding experiments, measuring the spin structure functions in detail remains a high priority in particle physics. Obviously the goal of truly understanding the quark-gluon substructure of the nucleons is the primary focus of these experiments. The questions can be phrased as; “where does the spin of the nucleon come from? How is the spin distributed among the constituent quarks? And, how do the ‘sea’ quarks and gluons contribute?” These are parts of the puzzle which is the nucleon, and it was the goal of SLAC experiment E154 to shed more light on as many of these unknowns as possible for the neutron.

1.8 Experiment E154

Experiment E154 was designed to measure the neutron spin structure functions as accurately as possible, over the broadest kinematic range achievable. Polarized electrons accelerated by the Stanford linear accelerator to an energy of 48.3 GeV and having an average polarization of 82% (section 3.8) were scattered off a polarized ^3He target (section 4.1) which had an average polarization of 35% with a dilution factor close to one-half. The scattered electrons were detected by two separate spectrometers set at laboratory central scattering angles of 2.75° and 5.5° . These kinematic conditions provided a Bjorken x coverage from 0.014 to 0.7, and Q^2 from about 1 GeV^2 to 17 GeV^2 . Roughly 10^8 scattered electrons were detected during the two month running period in October and November of 1995. These data provided a precision measurement of the neutron spin structure, and facilitated improved comparisons to the theoretical models of the nucleons.

CHAPTER 2

SPIN STRUCTURE

2.1 Electron Scattering

The kinematic variables for fixed target deep inelastic electron scattering are shown in Fig. 2.1. The incoming electron enters with four-momentum $k^\mu \equiv (E, \vec{k})$ and spin four-vector s^μ . After the interaction the scattered electron carries off four-momentum $k'^\mu \equiv (E', \vec{k}')$ and spin s'^μ . Similarly, before the interaction the target has four-momentum $P^\mu \equiv (E_n, \vec{P}) = (M, \vec{0})$, and spin S^μ in the laboratory reference frame, and the produced fragments, labeled as X in Fig. 2.1, carry four-momentum $P^\mu + q^\mu$ afterwards, where $q^\mu \equiv (\nu, \vec{q})$ is the four-momentum transferred from the electron to the nucleon, $\nu \equiv E - E'$ is the energy transferred, and $\vec{q} \equiv \vec{k} - \vec{k}'$ is the three-momentum transferred.

Quantum electrodynamics (QED) describes this interaction as a perturbative series where the Feynman diagram of Fig. 2.1 merely describes the lowest order term. This first term involves a single ‘virtual photon’, shown as the wavy line in Fig. 2.1, which transfers four-momentum from the electron to the nucleon. The full interaction is the sum of an infinite series of interactions where each successive term contains an additional virtual photon. Each additional photon contributes a factor of $\alpha = (1/137)$ to the amplitude, so the series converges quite rapidly, and is generally truncated after the first term, which is called the Born approximation, or the one-photon exchange approximation. The additional terms will not be discussed except with regard to radiative corrections in section 5.4.5.

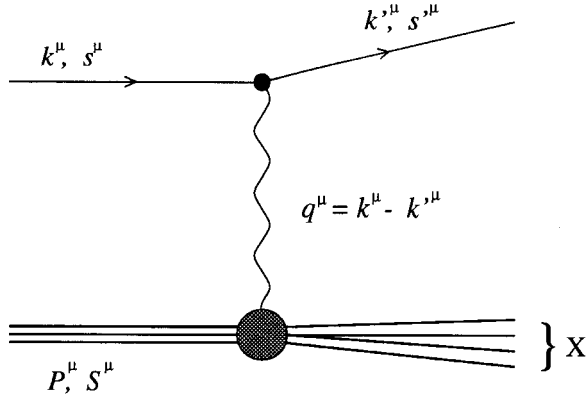


Figure 2.1. Feynman diagram for one photon exchange deep inelastic electron scattering. The incident (scattered) electron, shown as the upper lines, carries four-momentum k^μ (k'^μ) and spin s^μ (s'^μ). The target, shown as the lower lines, enters with four-momentum P^μ and spin S^μ , and after the scattering exits as some unknown state of X hadrons. The interaction proceeds via a single photon exchange, shown as the wavy line, which transfers four-momentum q^μ to the target.

Using Fermi's Golden rule, the cross section may be written using scattering amplitudes which are determined by quantum electrodynamics. The cross section takes the form [20]

$$d\sigma = \Phi |\langle f|\mathcal{M}|i\rangle|^2 \delta^4\left(P + q - \sum_{n=1}^X P_n\right) \frac{d^3k'}{2E'(2\pi)^3} \prod_{n=1}^X \frac{d^3P_n}{2E_n(2\pi)^3}. \quad (2.1)$$

The flux factor Φ was defined in Eq. (1.3), the delta function ensures energy and momentum conservation at the hadronic vertex, and the differentials describe the available phase space for the scattering process. The matrix element, $\langle f|\mathcal{M}|i\rangle$ is the scattering amplitude for the system to go from state $|i\rangle$ before the interaction to the state $|f\rangle$ after, and can be calculated using perturbation theory. The first order amplitude (one photon exchange) is [21]

$$i \langle f|\mathcal{M}|i\rangle = (-ie)^2 \langle k's'|j^\mu(0)|ks\rangle \left(\frac{-ig_{\mu\nu}}{q^2}\right) \langle XS'_X|J^\nu(0)|PS\rangle, \quad (2.2)$$

where e is the electric charge, $g_{\mu\nu}$ is the metric tensor, $|XS'_X\rangle$ is the final state of the hadronic products, and j^μ and J^ν are the leptonic and hadronic electromagnetic currents respectively.

In most experiments, only the scattered electron's four-momentum, k'^μ is measured, so both possible final electron spin states, s'^μ must be summed together. The same process is followed for the unobserved final state hadrons, and all possible states must be integrated over. Putting all the factors and sums together yields [21]

$$\begin{aligned}
d\sigma &= \frac{(2\pi)^4}{4EM} \frac{d^3k'}{2E'(2\pi)^3} \sum_X \sum_{s'_l, s'_X} \int \prod_{n=1}^X \frac{d^3P_n}{2E_n(2\pi)^3} \frac{e^4}{Q^4} \delta^4 \left(P + q - \sum_{m=1}^X P_m \right) \\
&\times \langle k s_l | j^\mu(0) | k' s'_l \rangle \langle k' s'_l | j^\nu(0) | k s_l \rangle \\
&\times \langle P S_n | J^\mu(0) | X S'_X \rangle \langle X S'_X | J^\nu(0) | P S_n \rangle,
\end{aligned} \tag{2.3}$$

where the flux factor has been explicitly evaluated in the laboratory reference frame as

$$\frac{1}{4\sqrt{(k \cdot P)^2 - m^2 M^2}} = \frac{1}{4EM}. \tag{2.4}$$

The second line of (2.3) can be identified as the leptonic tensor and written, including the sum over final state spins as

$$L^{\mu\nu} \equiv \sum_{s'_l} \langle k s_l | j^\mu(0) | k' s'_l \rangle \langle k' s'_l | j^\nu(0) | k s_l \rangle. \tag{2.5}$$

Since the electron is a point fermion, the individual matrix elements are specified in terms of the Dirac spinors and gamma matrices as [22]

$$\langle k' s'_l | j^\nu(0) | k s_l \rangle = \bar{u}(k', s'_l) \gamma^\nu u(k, s_l). \tag{2.6}$$

Combining both matrix elements, summing over the final state electron spins, using properties of the gamma matrices, and dropping factors involving the electron mass, the leptonic tensor may be converted to [21, 23]:

$$L^{\mu\nu} = 2[(k'^\mu k^\nu + k'^\nu k^\mu) - (k \cdot k') g^{\mu\nu} - i\epsilon^{\mu\nu\rho\sigma} q_\rho s_\sigma] \tag{2.7}$$

$$= L_S^{\mu\nu} + i L_A^{\mu\nu} \tag{2.8}$$

where $\epsilon^{\mu\nu\rho\sigma}$ is the Levi-Civita totally antisymmetric tensor, s_σ is the spin four-vector of the incoming electron, and $L_S^{\mu\nu}$ ($L_A^{\mu\nu}$) are the symmetric (antisymmetric) components of $L^{\mu\nu}$. Only the anti-symmetric part contains information about the electron spin. If the electron is longitudinally polarized, its spin four-vector is [24]

$$s^\mu = \frac{1}{m}(|\vec{k}|, 0, 0, E). \quad (2.9)$$

The hadronic matrix elements in Eq. (2.3) can be converted to a hadronic tensor in a completely analogous manner:

$$W_{\mu\nu}(P, q) \equiv \frac{1}{4\pi} \sum_{X, S'_X} (2\pi)^4 \delta^4(P + q - P_X) \langle PS | J^\mu(0) | X S'_X \rangle \langle X S'_X | J^\nu(0) | PS \rangle. \quad (2.10)$$

The hadronic tensor is not a product of simple point fermions as was the leptonic tensor. However, many properties including current conservation, hermiticity, translational invariance, and the time reversal and parity symmetries may be applied. Also, the tensor can only be constructed from the available tensors, $g_{\mu\nu}$, $\epsilon_{\mu\nu\rho\sigma}$, and four-vectors P_μ , q_μ , and S_σ . The most general form which fulfills all these requirements can be shown to be [21]

$$W_{\mu\nu} = W_{\mu\nu}^S + i W_{\mu\nu}^A, \quad (2.11)$$

where

$$W_{\mu\nu}^S = W_1 \left(-g_{\mu\nu} + \frac{q_\mu q_\nu}{q^2} \right) + \frac{W_2}{M^2} \left(P_\mu - \frac{P \cdot q}{q^2} q_\mu \right) \left(P_\nu - \frac{P \cdot q}{q^2} q_\nu \right), \quad (2.12)$$

and

$$W_{\mu\nu}^A = M G_1 \epsilon_{\mu\nu\lambda\sigma} q^\lambda S^\sigma + \frac{G_2}{M} \epsilon_{\mu\nu\lambda\sigma} q^\lambda (P \cdot q S^\sigma - S \cdot q P^\sigma). \quad (2.13)$$

The coefficients W_1 , W_2 , G_1 , and G_2 are the structure functions which describe the nucleon, and are analogous to the form factors of elastic scattering. They also depend on the energy and momentum transferred to the nucleon. As was done

with the leptonic tensor, $W_{\mu\nu}$ has been split into symmetric and antisymmetric components as shown in Eq. (2.11), and only the antisymmetric part is seen to contain information about the nucleon spin. Thus, the two structure functions, G_1 and G_2 of the antisymmetric piece are called the ‘spin structure functions.’ The goal of this experiment was the measurement of these spin structure functions for the neutron.

Combining everything to this point, the cross section in Eq. (2.3) can be rewritten in the following form [21]:

$$\frac{d^2\sigma}{dE' d\Omega} = \frac{e^4}{16\pi^2 Q^4} \left(\frac{E'}{E}\right) L^{\mu\nu} W_{\mu\nu}, \quad (2.14)$$

where the phase space factors have been integrated out as far as possible, the remaining differentials have been divided out to generate a differential cross section, and the momentum transfer squared, Q^2 is defined as

$$Q^2 \equiv -q_\mu q^\mu = 4EE' \sin^2\left(\frac{\theta}{2}\right). \quad (2.15)$$

The contraction of a symmetric tensor with an anti-symmetric tensor is zero, so only the combinations $L_S^{\mu\nu} W_{\mu\nu}^S$ and $L_A^{\mu\nu} W_{\mu\nu}^A$ result in non-zero cross sections. The contraction of the symmetric tensors produces the spin independent cross section, and in its most general form for deep inelastic electron scattering is [17, 21]

$$\frac{d^2\sigma}{dE' d\Omega} = \frac{4\alpha^2 E'^2}{Q^4} \left[\cos^2\left(\frac{\theta}{2}\right) W_2(\nu, Q^2) + 2 \sin^2\left(\frac{\theta}{2}\right) W_1(\nu, Q^2) \right], \quad (2.16)$$

where $\alpha \equiv e^2/4\pi\epsilon_0\hbar c$ is the fine structure constant.

The spin-dependent cross sections are handled slightly differently, and generally written in terms of the difference between cross sections of specific spin states. There are two distinct cases of interest [23],

$$\begin{aligned} \frac{d^2\Delta\sigma_{\parallel}}{dE' d\Omega} &\equiv \frac{d^2\sigma^{\uparrow\uparrow}}{dE' d\Omega} - \frac{d^2\sigma^{\uparrow\downarrow}}{dE' d\Omega} \\ &= \frac{4\alpha^2 E'}{Q^2 E} \left[MG_1(\nu, Q^2) (E + E' \cos\theta) - Q^2 G_2(\nu, Q^2) \right] \end{aligned} \quad (2.17)$$

for the spins of the electron and nucleon parallel and anti-parallel, and

$$\begin{aligned} \frac{d^2 \Delta\sigma_{\perp}}{dE' d\Omega} &\equiv \frac{d^2 \sigma^{\uparrow\leftarrow}}{dE' d\Omega} - \frac{d^2 \sigma^{\downarrow\leftarrow}}{dE' d\Omega} \\ &= \frac{4\alpha^2}{Q^2} \frac{E'}{E} E' \sin(\theta) \left[MG_1(\nu, Q^2) - 2EQ^2 G_2(\nu, Q^2) \right] \end{aligned} \quad (2.18)$$

for the nucleon spin perpendicular to the electron spin. The first arrow represents the electron helicity, and the second (double) arrow represents the target spin direction.

2.1.1 Virtual Photon Absorption

One of the main advantages of using electrons as probes is that the electron to virtual-photon vertex is completely understood. The quantities under investigation, the nucleon structure functions, contribute solely at the hadronic vertex of Fig. 2.1. It is thus informative to look at the virtual-photon nucleon scattering process in more detail. By the optical theorem [25], the total virtual photon absorption cross section is proportional to the imaginary part of the forward scattering amplitude,

$$\sigma = \frac{4\pi}{k} \text{Im} [\mathcal{M}(0)], \quad (2.19)$$

where k is the momentum, and $\mathcal{M}(0)$ is the forward scattering amplitude.

A spin-one virtual photon can be in any of three orthogonal spin states, while the struck spin-1/2 nucleon can be in either of two orthogonal spin states. Thus there are ten distinct combinations. They are labeled $\mathcal{M}_{ab,cd}$ where $a(c)$ represent the spin state projected along the momentum axis of the photon, \hat{q} , before (after) the interaction, and $b(d)$ is the spin of the nucleon projected along the same axis before (after) the interaction. Using parity and time reversal invariance most of these combinations are related, and only four independent helicity amplitudes which contribute the the virtual photon-nucleon cross section remain. These are usually

chosen to be [21]

$$\sigma_{3/2}^T = \frac{4\pi^2\alpha}{K} \mathcal{M}_{1\frac{1}{2},1\frac{1}{2}}, \quad (2.20)$$

$$\sigma_{1/2}^T = \frac{4\pi^2\alpha}{K} \mathcal{M}_{1-\frac{1}{2},1-\frac{1}{2}}, \quad (2.21)$$

$$\sigma_{1/2}^L = \frac{4\pi^2\alpha}{K} \mathcal{M}_{0\frac{1}{2},0\frac{1}{2}}, \quad (2.22)$$

$$\sigma_{1/2}^{TL} = \frac{4\pi^2\alpha}{K} \mathcal{M}_{0\frac{1}{2},0-\frac{1}{2}}, \quad (2.23)$$

where K is a factor representing the photon flux. The Hand convention [21] specifies it as

$$K = \frac{W^2 - M^2}{2M} = \nu - \frac{Q^2}{2M}, \quad (2.24)$$

where

$$W^2 \equiv M^2 + 2M\nu - Q^2 \quad (2.25)$$

is the invariant mass squared. The forward scattering amplitudes can be calculated from $W_{\mu\nu}$ in terms of the structure functions [26] as

$$\sigma_{3/2}^T = \frac{4\pi^2\alpha}{K} (W_1 + M\nu G_1 - Q^2 G_2), \quad (2.26)$$

$$\sigma_{1/2}^T = \frac{4\pi^2\alpha}{K} (W_1 - M\nu G_1 + Q^2 G_2), \quad (2.27)$$

$$\sigma_{1/2}^L = \frac{4\pi^2\alpha}{K} \left[W_2 \left(1 + \frac{\nu^2}{Q^2} \right) - W_1 \right], \quad (2.28)$$

$$\sigma_{1/2}^{TL} = \frac{4\pi^2\alpha}{K} \sqrt{Q^2} (M G_1 + \nu G_2). \quad (2.29)$$

The transverse virtual photoabsorption cross section is $\sigma_{3/2}^T$ ($\sigma_{1/2}^T$) when the total spin state of the photon-nucleon system, projected along the virtual photon propagation direction \hat{q} , is $3/2$ ($1/2$). The total transverse virtual photon absorption cross section is

$$\sigma^T = \frac{1}{2} (\sigma_{1/2}^T + \sigma_{3/2}^T) = \frac{4\pi^2\alpha}{K} W_1. \quad (2.30)$$

The corresponding cross section for a longitudinally polarized virtual photon is $\sigma_{1/2}^L$. The interference term between σ^T and σ^L , $\sigma_{1/2}^{TL}$ represents a helicity flip amplitude.

2.1.2 The Asymmetries

It is conceivable to try to extract the structure functions using Eqs. (2.16)-(2.18), directly; however, this would involve measuring absolute cross sections accurately, which is known to be a formidable task. For the spin structure functions it is abandoned in favor of an asymmetry measurement. Two asymmetries can be constructed allowing a separation of the structure function contributions analogous to a Rosenbluth separation. They are:

$$A_{\parallel}(x, Q^2) \equiv \frac{\sigma^{\uparrow\downarrow} - \sigma^{\downarrow\downarrow}}{\sigma^{\uparrow\downarrow} + \sigma^{\downarrow\downarrow}}, \quad (2.31)$$

and

$$A_{\perp}(x, Q^2) \equiv \frac{\sigma^{\uparrow\leftarrow} - \sigma^{\downarrow\leftarrow}}{\sigma^{\uparrow\leftarrow} + \sigma^{\downarrow\leftarrow}}, \quad (2.32)$$

where the shorthand notation

$$\sigma^{\uparrow\downarrow} \equiv \frac{d^2\sigma^{\uparrow\downarrow}}{d\Omega dE'} \quad (2.33)$$

has been used for all combinations of spins. The first arrow represents the electron helicity, and the second arrow the hadron helicity. By noticing that

$$\sigma^{\uparrow\downarrow} + \sigma^{\downarrow\downarrow} = 2\sigma, \quad (2.34)$$

with

$$\sigma \equiv \frac{d^2\sigma}{d\Omega dE'}, \quad (2.35)$$

these asymmetries can be written in terms of the spin dependent and independent cross sections (2.16), (2.17), and (2.18) as

$$A_{\parallel}(\nu, Q^2) = \frac{1 - \epsilon}{W_1(1 + \epsilon R)} [M(E + E' \cos \theta)G_1 - Q^2 G_2], \quad (2.36)$$

$$A_{\perp}(\nu, Q^2) = \frac{1 - \epsilon}{W_1(1 + \epsilon R)} E' \sin \theta [MG_1 + 2EG_2], \quad (2.37)$$

with the factors ϵ and R defined as

$$\epsilon \equiv \left[1 + 2 \left(1 + \frac{\nu^2}{Q^2} \right) \tan^2 \left(\frac{\theta}{2} \right) \right]^{-1}, \quad (2.38)$$

$$R \equiv \frac{\sigma_L}{\sigma_T} = \frac{W_2}{W_1} \left(1 + \frac{\nu^2}{Q^2} \right) - 1, \quad (2.39)$$

where σ_L and σ_T are the longitudinal and transverse cross sections defined in Eqs. (2.28) and (2.30). The factor ϵ represents the polarization of the virtual photon, which is generally less than the incident electron's polarization because it is emitted in a direction different from the incident electron's momentum.

In addition to these asymmetries, two more asymmetries are normally defined in terms of the virtual photon photoabsorption cross sections (2.26-2.29). They are called the photon-nucleon asymmetries, and are defined as

$$A_1 \equiv \frac{\sigma_{1/2}^T - \sigma_{3/2}^T}{\sigma_{1/2}^T + \sigma_{3/2}^T}, \quad (2.40)$$

and

$$A_2 \equiv \frac{\sigma_{1/2}^{TL}}{\sigma^T}. \quad (2.41)$$

Using Eqs. (2.26-2.29), these asymmetries can be rewritten as

$$A_1 = \frac{M\nu G_1 - Q^2 G_2}{W_1} \quad (2.42)$$

and

$$A_2 = \sqrt{Q^2} \frac{MG_1 + \nu G_2}{W_1}. \quad (2.43)$$

Finally, conversions between the photon-nucleon asymmetries A_1 and A_2 , and the experimental, or electron-nucleon asymmetries $A_{||}$ and A_{\perp} , may be calculated as

$$A_{||}(x, Q^2) = D[A_1(x, Q^2) + \eta A_2(x, Q^2)], \quad (2.44)$$

$$A_{\perp}(x, Q^2) = d[A_2(x, Q^2) - \xi A_1(x, Q^2)], \quad (2.45)$$

$$A_1(x, Q^2) = \frac{A_{||}(x, Q^2)}{D(1 + \eta\xi)} - \frac{\eta A_{\perp}(x, Q^2)}{d(1 + \eta\xi)}, \quad (2.46)$$

$$A_2(x, Q^2) = \frac{\xi A_{||}(x, Q^2)}{D(1 + \eta\xi)} + \frac{A_{\perp}(x, Q^2)}{d(1 + \eta\xi)}, \quad (2.47)$$

where

$$D \equiv \frac{1 - E'\epsilon/E}{1 + \epsilon R}, \quad (2.48)$$

$$\eta \equiv \frac{\epsilon\sqrt{Q^2}}{E - \epsilon E'}, \quad (2.49)$$

$$d \equiv D\sqrt{\frac{2\epsilon}{1 + \epsilon}}, \quad (2.50)$$

$$\xi \equiv \frac{\eta(1 + \epsilon)}{2\epsilon}, \quad (2.51)$$

and ϵ and R were defined in Eqs. (2.38) and (2.39).

2.1.3 Cross Sections using F_1 , F_2 , g_1 , and g_2

The four structure functions W_1 , W_2 , G_1 , and G_2 are functions of ν and Q^2 . A different set of functions depending on x and Q^2 can be defined as follows:

$$F_1(x, Q^2) = MW_1(\nu, Q^2), \quad (2.52)$$

$$F_2(x, Q^2) = \nu W_2(\nu, Q^2), \quad (2.53)$$

$$g_1(x, Q^2) = M^2\nu G_1(\nu, Q^2), \quad (2.54)$$

$$g_2(x, Q^2) = M\nu^2 G_2(\nu, Q^2), \quad (2.55)$$

where $x \equiv Q^2/(2M\nu)$ is the Bjorken scaling variable, and represents the fraction of the nucleon's momentum carried by a given quark. It is convenient to use these forms, since they are the ones which scale (see section 2.1.4). It is an historical artifact that the formulation of the electron scattering formalism was not done using the F_i and g_i structure functions.

The hadronic tensor, (2.11) may be rewritten in terms of the four structure functions defined in Eqs. (2.52)-(2.55) by simple substitution as

$$W_{\mu\nu}^S = \frac{F_1}{M} \left(-g_{\mu\nu} + \frac{q_\mu q_\nu}{q^2} \right) + \frac{F_2}{M(P \cdot q)} \left(P_\mu - \frac{P \cdot q}{q^2} q_\mu \right) \left(P_\nu - \frac{P \cdot q}{q^2} q_\nu \right), \quad (2.56)$$

and

$$W_{\mu\nu}^A = \frac{g_1}{P \cdot q} \epsilon_{\mu\nu\lambda\sigma} q^\lambda S^\sigma + \frac{g_2}{(P \cdot q)^2} \epsilon_{\mu\nu\lambda\sigma} q^\lambda (P \cdot q S^\sigma - S \cdot q P^\sigma). \quad (2.57)$$

With these, the spin independent and dependent cross sections (2.16), (2.17), and (2.18) become

$$\frac{d^2\sigma}{dx dQ^2} = \frac{4\pi\alpha^2}{Q^4x} \left[\left(1 - \frac{Q^2}{2ME_x} - \frac{Q^2}{4E^2} \right) F_2(x, Q^2) + \frac{Q^4}{4M^2E^2x} F_1(x, Q^2) \right], \quad (2.58)$$

$$\frac{d^2\Delta\sigma_{\parallel}}{dx dQ^2} = \frac{4\pi\alpha^2}{ME_xQ^2} \left[\left(2 - \frac{Q^2}{2ME_x} - \frac{Q^2}{2E^2} \right) g_1(x, Q^2) - \frac{2Mx}{E} g_2(x, Q^2) \right], \quad (2.59)$$

and

$$\frac{d^2\Delta\sigma_{\perp}}{dx dQ^2} = \frac{2\pi\alpha^2 \cot(\theta/2)}{E^3xM} \left[g_1(x, Q^2) - 4EMxg_2(x, Q^2) \right]. \quad (2.60)$$

Note that the differentials in the cross section are now in terms of dx and dQ^2 instead of dE' and $d\Omega$. The conversion between the different forms of the cross sections is given by

$$\frac{d^2\sigma}{d\Omega dE'} = \left(\frac{\pi\nu}{E^2x} \right) \frac{d^2\sigma}{dx dQ^2}. \quad (2.61)$$

Finally, all the preceding formulae for the asymmetries can be converted to forms in terms of the scaling structure functions, (2.52-2.55) as

$$A_{\parallel}(x, Q^2) = \frac{1 - \epsilon}{\nu F_1(1 + \epsilon R)} [(E + E' \cos \theta)g_1 - 2Mxg_2], \quad (2.62)$$

$$A_{\perp}(x, Q^2) = \frac{1 - \epsilon}{\nu F_1(1 + \epsilon R)} E' \sin \theta \left[g_1 + \frac{2E}{\nu} g_2 \right], \quad (2.63)$$

$$A_1(x, Q^2) = \frac{g_1 - 2Mxg_2/\nu}{F_1}, \quad (2.64)$$

$$A_2(x, Q^2) = \frac{\sqrt{Q^2}(g_1 + g_2)}{\nu F_1}. \quad (2.65)$$

2.1.4 Scaling Behavior of the Structure Functions

In the quark-parton model, deep inelastic scattering is interpreted as an elastic scattering of the virtual photon off a single constituent quark in the nucleon. In this case the quarks are assumed to be simple point-like, spin-1/2 Dirac particles, so the quark-electron interaction is fully calculable. A nucleon is made of three

‘constituent’ quarks. A proton consists of two ‘up’ and one ‘down’, while a neutron contains one ‘up’ and two ‘down’ constituent quarks. The term ‘constituent’ specifies these as quarks which carry the quantum numbers of the nucleon, in contrast to the ‘sea’ quarks which condense out of the vacuum in quark-antiquark pairs for short periods of time. They should also be contrasted with ‘valence’ or ‘bare’ quarks which are the QCD fields described in Table 1.1.

The probability of a quark carrying a fraction x of the nucleon momentum is labeled as $q(x)$. Choosing the quark spin quantization axis the same as the nucleon spin quantization axis, the two spin states of the quarks and anti-quarks are labeled $q^\uparrow(x)$, $\bar{q}_i^\uparrow(x)$, and $q^\downarrow(x)$, $\bar{q}_i^\downarrow(x)$ for spins parallel and antiparallel respectively to the spin of the parent nucleon.

Using the quark-parton model, the structure functions take simple forms in terms of the quark probabilities [27]:

$$F_1(x) = \frac{1}{2} \sum_i e_i^2 [q_i^\uparrow(x) + q_i^\downarrow(x) + \bar{q}_i^\uparrow(x) + \bar{q}_i^\downarrow(x)], \quad (2.66)$$

$$F_2(x) = x \sum_i e_i^2 [q_i^\uparrow(x) + q_i^\downarrow(x) + \bar{q}_i^\uparrow(x) + \bar{q}_i^\downarrow(x)], \quad (2.67)$$

$$g_1(x) = \frac{1}{2} \sum_i e_i^2 [q_i^\uparrow(x) - q_i^\downarrow(x) + \bar{q}_i^\uparrow(x) - \bar{q}_i^\downarrow(x)], \quad (2.68)$$

$$g_2(x) = 0, \quad (2.69)$$

where e_i is the electric charge of a quark of flavor i , and the sum is over all relevant flavors. Normally the relevant flavors are chosen to be up, down, and strange. The charm quark can play a role above its production threshold, but is usually ignored at the Q^2 of these experiments. Note that both ‘constituent’, and ‘sea’ quarks are utilized. Also, Eqs. (2.66)-(2.69) implicitly assume that there are no quark-quark interactions, which is plausible only in the Bjorken limit of infinite momentum.

As shown by Eqs. (2.66)-(2.69), in the QPM model, the structure functions are functions of x alone, and do not depend on Q^2 . This is termed ‘scaling’. The naive QPM picture leading to scaling behavior is, however only valid for $\nu, Q^2 \rightarrow \infty$,

termed the ‘scaling limit’, since the quark-quark interactions dominate otherwise. In the scaling limit the structure functions, (2.52)-(2.55) become,

$$\lim_{\nu, Q^2 \rightarrow \infty} F_1(x, Q^2) \rightarrow F_1(x), \quad (2.70)$$

$$\lim_{\nu, Q^2 \rightarrow \infty} F_2(x, Q^2) \rightarrow F_2(x), \quad (2.71)$$

$$\lim_{\nu, Q^2 \rightarrow \infty} g_1(x, Q^2) \rightarrow g_1(x), \quad (2.72)$$

$$\lim_{\nu, Q^2 \rightarrow \infty} g_2(x, Q^2) \rightarrow g_2(x), \quad (2.73)$$

explaining why they are used instead of W_1 , W_2 , G_1 , and G_2 .

2.1.5 Interpretations of the Structure Functions

In the QPM, the first moment of the spin structure function, $g_1(x)$ may be calculated [27] using Eqs. (2.66)-(2.69) for both the proton

$$\Gamma_1^p \equiv \int_0^1 g_1^p(x) dx = \frac{1}{2} \left(\frac{4}{9} \Delta u + \frac{1}{9} \Delta d + \frac{1}{9} \Delta s \right) \quad (2.74)$$

and the neutron

$$\Gamma_1^n \equiv \int_0^1 g_1^n(x) dx = \frac{1}{2} \left(\frac{1}{9} \Delta u + \frac{4}{9} \Delta d + \frac{1}{9} \Delta s \right), \quad (2.75)$$

where the notation

$$\Delta q = \int_0^1 dx [q^\uparrow(x) - q^\downarrow(x) + \bar{q}^\uparrow(x) - \bar{q}^\downarrow(x)] \quad (2.76)$$

has been used to represent the fraction of the nucleon spin carried by a specific quark flavor and isospin symmetry suggests the Δu in the neutron is the same as the Δd in the proton, and Δd in the neutron is the same as the Δu in the proton. These moments have the obvious interpretation as the overall nucleon spin, which allows Δq to be interpreted as the spin contribution due to an individual flavor.

A somewhat more realistic version of the quark-parton model includes spin contributions to the nucleons from both the spins of the gluons, and the relative

orbital angular momentum of the quarks, $\langle L_z \rangle$. The integrals (2.74) and (2.75) may then be written as:

$$\Gamma_1^p = \frac{1}{2} \Delta \Sigma^p + \langle L_z \rangle + \Delta G \quad (2.77)$$

and

$$\Gamma_1^n = \frac{1}{2} \Delta \Sigma^n + \langle L_z \rangle + \Delta G \quad (2.78)$$

where

$$\Delta \Sigma^p \equiv \frac{4}{9} \Delta u + \frac{1}{9} \Delta d + \frac{1}{9} \Delta s, \quad (2.79)$$

$$\Delta \Sigma^n \equiv \frac{1}{9} \Delta u + \frac{4}{9} \Delta d + \frac{1}{9} \Delta s, \quad (2.80)$$

and ΔG represents the spin contribution of the gluons in a way analogous to the quarks

$$\Delta G \equiv \int_0^1 dx \left[g^\uparrow(x) - g^\downarrow(x) + \bar{g}^\uparrow(x) - \bar{g}^\downarrow(x) \right]. \quad (2.81)$$

Note that unless the gluons, which are simply mediating the strong color force between the quarks, are polarized to any degree, most of the spin of the nucleon is due to the quarks, since in the naive QPM the orbital angular momentum between the quarks only contributes between 25% and 40%.

2.2 Q^2 Evolution

The structure functions, which are in general functions of Q^2 , exhibit scaling behavior at large momentum transfer values, and become independent of Q^2 . Experiments however, are performed at finite, and often quite low values of Q^2 . Also, different experiments are typically performed at different values of Q^2 for the same x values, making it necessary to be able to ‘evolve’ the structure functions between different values of Q^2 in order to make meaningful comparisons. This is especially important if the extracted structure functions contain other structure functions

determined from different experiments, such as F_2 and R , which are necessary to calculate the neutron structure functions (see Eqs. (2.103) and (2.123)).

The normal method for doing this is to assume that the Q^2 dependence of the spin structure functions is similar to that of the unpolarized structure functions so the ratio $g_1(x)/F_1(x)$, should be nearly independent of Q^2 . Experimentally this has been well verified by several groups over very broad kinematic ranges [28, 29].

However, there is no obvious theoretical reason why the spin structure functions should have the same Q^2 dependence as the spin independent structure functions. In fact, there are good reasons that the Q^2 -dependences differ. A more appropriate form for the Q^2 evolution, which incorporates the theoretical requirements, proceeds through the GLAP equations [18], which state

$$\frac{d}{dt} \begin{pmatrix} g \\ q_S \end{pmatrix} = \frac{\alpha_s(t)}{2\pi} \begin{pmatrix} P_{gg} & P_{gq} \\ P_{qg} & P_{qq}^S \end{pmatrix} \otimes \begin{pmatrix} g \\ q_S \end{pmatrix} \quad (2.82)$$

$$\frac{d}{dt} q_{NS} = \frac{\alpha_s(t)}{2\pi} P_{qq}^{NS} \otimes q_{NS}, \quad (2.83)$$

where

$$t \equiv \ln \left(\frac{Q^2}{\Lambda^2} \right), \quad (2.84)$$

the symbol \otimes represents the convolution

$$P(x) \otimes q(x) \equiv \int_x^1 \frac{dx'}{x'} P(x') q \left(\frac{x}{x'} \right) \quad (2.85)$$

and the singlet (S) and non-singlet (NS) quark distributions are

$$q_S(x, t) = \sum_{i=1}^{n_f} \left[q_i(x_i, Q^2) + \bar{q}_i(x_i, Q^2) \right], \quad (2.86)$$

and

$$q_{NS}(x, t) = \sum_{i=1}^{n_f} \left(\frac{e_i^2}{\langle e^2 \rangle} - 1 \right) \left[q_i(x_i, Q^2) + \bar{q}_i(x_i, Q^2) \right], \quad (2.87)$$

with n_f the active number of quark flavors, and α_s the strong coupling constant. The perturbative QCD cut-off Λ is typically about 250 MeV, and the ‘splitting’

functions P_{ij} are given for all orders n in perturbative QCD by

$$\frac{\alpha_s(t)}{2\pi} P(x, t) = \sum_{k=1}^n P^{(k)} \left(\frac{\alpha_s(t)}{2\pi} \right)^k + \mathcal{O}(\alpha_s^{n+1}). \quad (2.88)$$

These sets of equations define the appropriate Q^2 evolution for the quark densities which in turn determine the structure functions through Eqs. (2.66-2.69).

The GLAP equations are mentioned here since they are important for a next-to-leading order QCD analysis of the structure functions undertaken by the E154 collaboration [30]. However, in order to extract the spin structure functions from the asymmetry data, there is no need, at the level of accuracy of the present data, to do anything more than use the fact that $g_1(x)/F_1(x)$ is independent of Q^2 .

2.3 Sum Rules

As mentioned in the Introduction, a number of sum rules exist which relate the integrals over all x of the structure functions to other observables. The most important of these from a theoretical viewpoint is the Bjorken sum rule [8], relating the integral of the difference between the proton and neutron g_1 spin structure functions to the ratio between axial-vector and vector couplings for neutron beta decay. Also relevant to the spin structure functions are the Ellis-Jaffe sum rule [9], which predicts the integral of $g_1(x)$ for both the proton and the neutron individually, and the Burkhardt-Cottingham sum rule [19] for $g_2(x)$.

2.3.1 The Bjorken Sum Rule

The Bjorken sum rule [8] was derived in 1966 using current algebra, and states

$$\Gamma_1^p - \Gamma_1^n \equiv \int_0^1 dx [g_1^p(x) - g_1^n(x)] = \frac{1}{6} \left(\frac{g_A}{g_V} \right), \quad (2.89)$$

where g_A/g_V is the ratio between the nucleon axial vector coupling and the nucleon vector coupling determined from neutron beta decay [31] and is equal to 1.2601 ± 0.0025 .

The Bjorken sum rule was derived in the Bjorken limit of ν , $Q^2 \rightarrow \infty$ while $x = Q^2/(2M\nu)$ remains finite. The extremely high ν and Q^2 region is inaccessible to experiments, so corrections must be made for the finite ν and Q^2 values available to experiments if the sum rule is to be tested. The best corrections to date for finite Q^2 effects have been calculated by Larin and Vermaseren [32] with an estimate of the fourth order correction by Kataev and Starshenko [33], who find:

$$\int_0^1 dx [g_1^p(x) - g_1^n(x)] = \frac{1}{6} \left(\frac{g_A}{g_V} \right) \sum_i C_i^{ns} \left(\frac{\alpha_s(Q^2)}{\pi} \right)^i, \quad (2.90)$$

where the C_i^{ns} are given below in Eqs.(2.91), $\alpha_s(Q^2)$ is the Q^2 dependent strong coupling constant, and the ns superscript refers to the fact that these are non-singlet corrections. The coefficients, assuming three active quark flavors, are

$$\begin{aligned} C_0^{ns} &= 1, \\ C_1^{ns} &= -1, \\ C_2^{ns} &= -3.5833, \\ C_3^{ns} &= -20.2153, \\ C_4^{ns} &= -\mathcal{O}(130). \end{aligned} \quad (2.91)$$

With these corrections, the Bjorken sum rule prediction is

$$\int_0^1 dx [g_1^p(x) - g_1^n(x)] = 0.188 \quad (2.92)$$

at $Q^2 = 5 \text{ GeV}^2$.

2.3.2 The Ellis-Jaffe Sum Rule

In 1974 Ellis and Jaffe derived a set of sum rules for the proton and neutron individually [9]. The proton sum rule states

$$\int_0^1 g_1^p(x) dx = \frac{1}{12} \left(\frac{g_A}{g_V} \right) \left(1 + \frac{5}{3} \frac{(3F/D) - 1}{(F/D) + 1} \right), \quad (2.93)$$

and the neutron sum rule states

$$\int_0^1 g_1^n(x) dx = \frac{1}{12} \left(\frac{g_A}{g_V} \right) \left(-1 + \frac{5}{3} \frac{(3F/D) - 1}{(F/D) + 1} \right). \quad (2.94)$$

The F/D ratio for axial charges is well determined [34], yielding a value of 0.575 ± 0.016 .

This sum rule depends on SU(3) symmetry between the light quarks, which is known not to be an exact symmetry. Ellis and Jaffe themselves point out that the sum rule should not be exact for this reason. The assumption has also been made that the sea quarks and gluons are unpolarized, which is not necessarily the case.

As with the Bjorken sum rule, there are QCD corrections which must be applied to the Ellis-Jaffe sum rule to account for finite Q^2 effects, before it can be compared with experimental measurements. The best corrections to date were derived in reference [35] and are

$$\int_0^1 g_1^n(x) dx = C^{ns} \left(\frac{\alpha_s}{\pi} \right) \left[-\frac{1}{12} \frac{g_A}{g_V} + \frac{a_8}{36} \right] + C^s \left(\frac{\alpha_s}{\pi} \right) \frac{1}{9} \hat{a}_0, \quad (2.95)$$

where C^{ns} is the same sum of non-singlet corrections used on the Bjorken sum rule in Eq. (2.90), C^s are the corresponding singlet terms given as,

$$\begin{aligned} C_0^s &= 1.0000, \\ C_1^s &= -0.33333, \\ C_2^s &= -0.54959, \\ C_3^s &= -4.44725, \end{aligned} \quad (2.96)$$

and the form of the sum rule has been changed somewhat to distinguish between singlet and non-singlet contributions. The definitions of a_8 and \hat{a}_0 are given in reference [35].

One of the main goals of the experiment described in this dissertation was an experimental measurement of this sum rule. With all relevant QCD corrections, the experimental data available before this experiment was performed agreed only marginally with this sum rule. At Q^2 of 5 GeV², the prediction for the neutron is -0.018 ± 0.009 , while the available data gave -0.028 ± 0.006 [34].

2.3.3 The Burkhardt-Cottingham Sum Rule

Finally, there exists a sum rule for $g_2(x)$ due to Burkhardt and Cottingham [19] which states

$$\int_0^1 g_2(x) dx = 0. \quad (2.97)$$

This is closely related to a parameterization of g_2 due to Wandzura and Wilczek [36], usually referred to as g_2^{WW} , who find

$$g_2^{WW}(x) = -g_1(x) + \int_x^1 \frac{dy}{y} g_1(y). \quad (2.98)$$

Their parameterization only accounts for twist-2 matrix elements. However, higher twist effects are thought to be significant for g_2 [37], so a better parameterization is

$$g_2(x) = g_2^{WW}(x) + g_2^{HT}(x), \quad (2.99)$$

where $g_2^{HT}(x, Q^2)$ contains the higher twist contributions (twist three and higher). In fact there is an additional twist-2 contribution to the g_2^{WW} formulation, due to the transverse polarization density in the nucleon [38]. However, this can be ignored since it is suppressed by the ratio of the quark to nucleon mass, m/M .

In addition to the sum rule, there is a theoretical limit on $g_2^n(x)$ [39] based on ‘positivity’, stating that the transverse photon asymmetry, A_2^n must be less

than \sqrt{R} . In the past, this has been used as a limit on the g_2 contribution to the experimentally measured asymmetry. It was hoped however, that the systematic uncertainties for this experiment could be reduced by using measured values rather than theoretic limits.

2.4 Measuring the Structure Functions

A polarized DIS experiment usually measures the electron-nucleon asymmetries $A_{\parallel}(x, Q^2)$ and $A_{\perp}(x, Q^2)$. This is accomplished by counting the number of electrons of each helicity scattered into the spectrometers (detectors), and generating asymmetries through the relation

$$A_{raw}(x, Q^2) = \frac{n^{\uparrow} - n^{\downarrow}}{n^{\uparrow} + n^{\downarrow}}, \quad (2.100)$$

where $n^{\uparrow} = N^{\uparrow}/Q^{\uparrow}$ is the number of detected electrons, N^{\uparrow} per incident charge Q^{\uparrow} for the electron helicity right. The same definition holds for n^{\downarrow} , except it is for incident electron helicity left. Two raw asymmetries are generated depending on the direction of the target polarization relative to the electron polarization. For target polarizations parallel (antiparallel) to the electron polarization direction, $A_{raw_{\parallel}}$ is measured, and for the target polarization direction perpendicular to the electron polarization direction $A_{raw_{\perp}}$ is measured.

These raw asymmetries are converted to the familiar electron-nucleon asymmetries using

$$A_{\parallel}(x, Q^2) = \frac{A_{raw_{\parallel}}(x, Q^2)}{f P_b P_t}, \quad (2.101)$$

$$A_{\perp}(x, Q^2) = \frac{A_{raw_{\perp}}(x, Q^2)}{f P_b P_t}, \quad (2.102)$$

where f is the dilution factor describing the fraction of polarized to unpolarized target particles (see section 4.2), P_b is the beam polarization, and P_t is the target

polarization. The electron-nucleon asymmetries, (2.101) and (2.102) are converted to photon-nucleon asymmetries $A_1(x, Q^2)$ and $A_2(x, Q^2)$ using (2.46) and (2.47).

The quantities of interest, $g_1^n(x, Q^2)$ and $g_2^n(x, Q^2)$ can be extracted from the photon-nucleon asymmetries using [45]

$$g_1^n(x, Q^2) = \frac{A_1^n(x, Q^2)F_2(x, Q^2)}{2x[1 + R(x, Q^2)]} \quad (2.103)$$

and

$$g_2^n(x, Q^2) = \frac{\nu^2}{\sqrt{Q^2}}F_1(x, Q^2)\frac{(\nu A_2 - \sqrt{Q^2}A_1)}{(\nu^2 + Q^2)}. \quad (2.104)$$

In addition to the measured asymmetries, values for R , defined in Eq. (2.39), and the unpolarized structure function F_1 , are required to determine the spin structure functions g_1 and g_2 . Both of these have been measured quite accurately and fit to phenomenological functions which can be used over the E154 x and Q^2 range [40, 42, 43]. The parameterized version of $R(x, Q^2)$ is called R1990 [40], and is given by

$$R^{1990}(x, Q^2) = \frac{b_1}{\ln(Q^2/\Lambda^2)}\Theta(x, Q^2) + \frac{b_2}{Q^2} + \frac{b_3}{Q^4 + 0.09}, \quad (2.105)$$

where $\Lambda \equiv 0.2$ GeV,

$$\Theta(x, Q^2) \equiv 1 + 12 \left(\frac{Q^2}{Q^2 + 1} \right) \left(\frac{0.125^2}{0.125^2 + x^2} \right), \quad (2.106)$$

and the parameters are found to be

$$b_1 = 0.635 \quad (2.107)$$

$$b_2 = 0.5747 \quad (2.108)$$

$$b_3 = -0.3534. \quad (2.109)$$

The latest parameterization of F_2 can be found in [43], and has the form

$$F_2(x, Q^2) = A(x) \left(\frac{\ln(Q^2/\Lambda^2)}{\ln(Q_0^2/\Lambda^2)} \right)^{B(x)} \left(1 + \frac{C(x)}{Q^2} \right), \quad (2.110)$$

with $Q_0^2 \equiv 20$ GeV, $\Lambda \equiv 0.250$ GeV, and

$$\begin{aligned}
 A(x) &\equiv x^{a_1} \delta^{a_2} [a_3 + a_4 \delta + a_5 \delta^2 + a_6 \delta^3 + a_7 \delta^4], \\
 B(x) &\equiv b_1 + b_2 x + \frac{b_3}{(x + b_4)}, \\
 C(x) &\equiv c_1 x + c_2 x^2 + c_3 x^3 + c_4 x^4,
 \end{aligned}
 \tag{2.111}$$

and $\delta \equiv 1 - x$. The fifteen parameters are listed in Table 2.1.

Table 2.1. Parameters for the 15 parameter fit to $F_2(x)$.

Parameter	Value
a_1	-0.02778
a_2	2.926
a_3	1.0362
a_4	-1.840
a_5	8.123
a_6	-13.074
a_7	6.215
b_1	0.285
b_2	-2.694
b_3	0.0188
b_4	0.0274
c_1	-1.413
c_2	9.366
c_3	-37.79
c_4	47.10

2.5 Neutron Targets

Measurements of the neutron structure functions are complicated by the fact that no pure neutron targets exist. Neutrons are unstable, and undergo beta-decay with a mean life of 14.8 minutes [12]. While it is possible to trap free neutrons, it is not possible to do this with a high enough number density to be considered as a target for scattering experiments. Since there are no elements consisting only of neutrons, every measurement must utilize a nuclear target of some sort, typically

either deuterium or ${}^3\text{He}$, and use a parameterization of the nuclear wave function to subtract the ‘extra’ proton spin contributions from the resulting cross sections. In the case of deuterium, this is done by assuming the deuteron structure functions can be built out of the constituent nucleon structure functions as

$$g_1^d = \frac{(g_1^p + g_1^n)}{2} \left(1 - \frac{3}{2}\omega_D\right), \quad (2.112)$$

where $\omega_D = 0.05 \pm 0.01$ accounts for the D -state component in the deuteron [29].

The experiment described in this thesis used ${}^3\text{He}$ as the target material. The ground state of the spin-1/2 ${}^3\text{He}$ nucleus is primarily an S state, with the spins of the two protons anti-aligned due to the Pauli Exclusion Principle. Thus the unpaired neutron contributes the majority of the spin of the ${}^3\text{He}$ nucleus. If the nucleus is examined in greater detail, two additional contributions to the ground state are found; an S' state which accounts for 1.54% of the ${}^3\text{He}$ wave function, and a D state contributing 8.37% [48]. Because of these states, the conceptual picture described above is not strictly accurate. A more complete model for the ${}^3\text{He}$ spin composition was derived by Friar taking these additional states into account [49].

Define $P_n^{+(-)}$ as the number of neutrons with spins aligned (anti-aligned) with the ${}^3\text{He}$ nuclear spin, and $P_p^{+(-)}$ the same for the protons, then define Δ such that

$$P_n^+ = 1 - \Delta \quad (2.113)$$

$$P_n^- = \Delta, \quad (2.114)$$

so

$$\Delta = \frac{P(S') + 2P(D)}{3}, \quad (2.115)$$

where $P(S')$ is the probability of the S' state, and $P(D)$ is the probability of the D state. Likewise, define Δ' such that

$$P_p^+ = \frac{1}{2} - \Delta' \quad (2.116)$$

$$P_p^- = \frac{1}{2} + \Delta', \quad (2.117)$$

so

$$\Delta' = \frac{P(D) - P(S')}{6}. \quad (2.118)$$

Using these, the average polarizations of the individual nucleons in the ${}^3\bar{\text{H}}\text{e}$ nucleus, p_n and p_p may be written as

$$p_n \equiv P_n^+ - P_n^- = 1 - 2\Delta, \quad (2.119)$$

$$p_p \equiv P_p^+ - P_p^- = -2\Delta'. \quad (2.120)$$

Averaging the results for Δ and Δ' of many different models, Friar *et al.* [49] found

$$p_n = 0.86 \pm 0.02 \quad (2.121)$$

$$p_p = -0.027 \pm 0.004. \quad (2.122)$$

The errors reflect the model uncertainties in determining Δ and Δ' . These polarizations may then be used to decompose the nuclear structure functions into the constituent nucleon structure functions [50]

$$g_1^{3\text{He}}(x) = 2p_p g_1^p(x) + p_n g_1^n(x), \quad (2.123)$$

and the asymmetries decompose as

$$A_{3\text{He}} = 2 \frac{F_2^p}{2F_2^p + F_2^n} p_p A_p + \frac{F_2^n}{2F_2^p + F_2^n} p_n A_n. \quad (2.124)$$

2.6 Status of Experiments

As described in Chapter 1, the first polarized DIS experiment, E80 was carried out at SLAC in 1976 [5], and measured g_1^p over a fairly small kinematic range. It was followed by SLAC experiment E130 in 1983 [6], in which g_1^p , was measured over a broader kinematic range $0.18 < x < 0.7$. In the late 1980's a series of experiments was begun at CERN using naturally polarized muons to probe the spin structure

functions. The first of these was conducted by the European Muon Collaboration (EMC), with measurements of g_1^p over a much wider range of x than the previous experiments [7]. This was followed by a series of CERN experiments on different targets which started in the early 1990s by the Spin Muon Collaboration (SMC) [45]. Interspersed were two more SLAC experiments, E142 [46], and E143 [47]. The experiments are summarized in Table 2.2, showing which structure functions were measured, and over what kinematic ranges.

Table 2.2. The DIS spin structure function experiments, with kinematic ranges, and structure functions measured. The superscript d refers to the deuteron, and the dates are for publication times.

Experiment	Date	Kinematic Range		Reference
SLAC E80	1976		$g_1^p(x)$	[5]
SLAC E130	1983	$0.18 < x < 0.7$	$g_1^p(x)$	[6]
EMC	1988	$0.01 < x < 0.7$	$g_1^p(x)$	[7]
SMC	1993	$0.006 < x < 0.6$	$g_1^d(x)$	[45]
	1994	$0.003 < x < 0.6$	$g_1^p(x)$	
	1994	$0.006 < x < 0.6$	$g_2^p(x)$	
	1995	$0.003 < x < 0.7$	$g_1^d(x)$	
SLAC E142	1993	$0.03 < x < 0.6$	$g_1^n(x)$	[46]
SLAC E143	1995	$0.029 < x < 0.8$	$g_1^p(x)$	[47]
	1995	$0.029 < x < 0.8$	$g_1^d(x)$	
	1996	$0.029 < x < 0.8$	$g_2^p(x)$	
	1996	$0.029 < x < 0.8$	$g_2^d(x)$	

A compilation of all available data for $g_1^n(x)$ before E154 is shown in Fig. 2.2. As can be seen, there were many data points in the mid- x range, but they lacked accuracy. It was hoped that E154 could both improve the accuracy, and extend the precision measurements to lower x values.

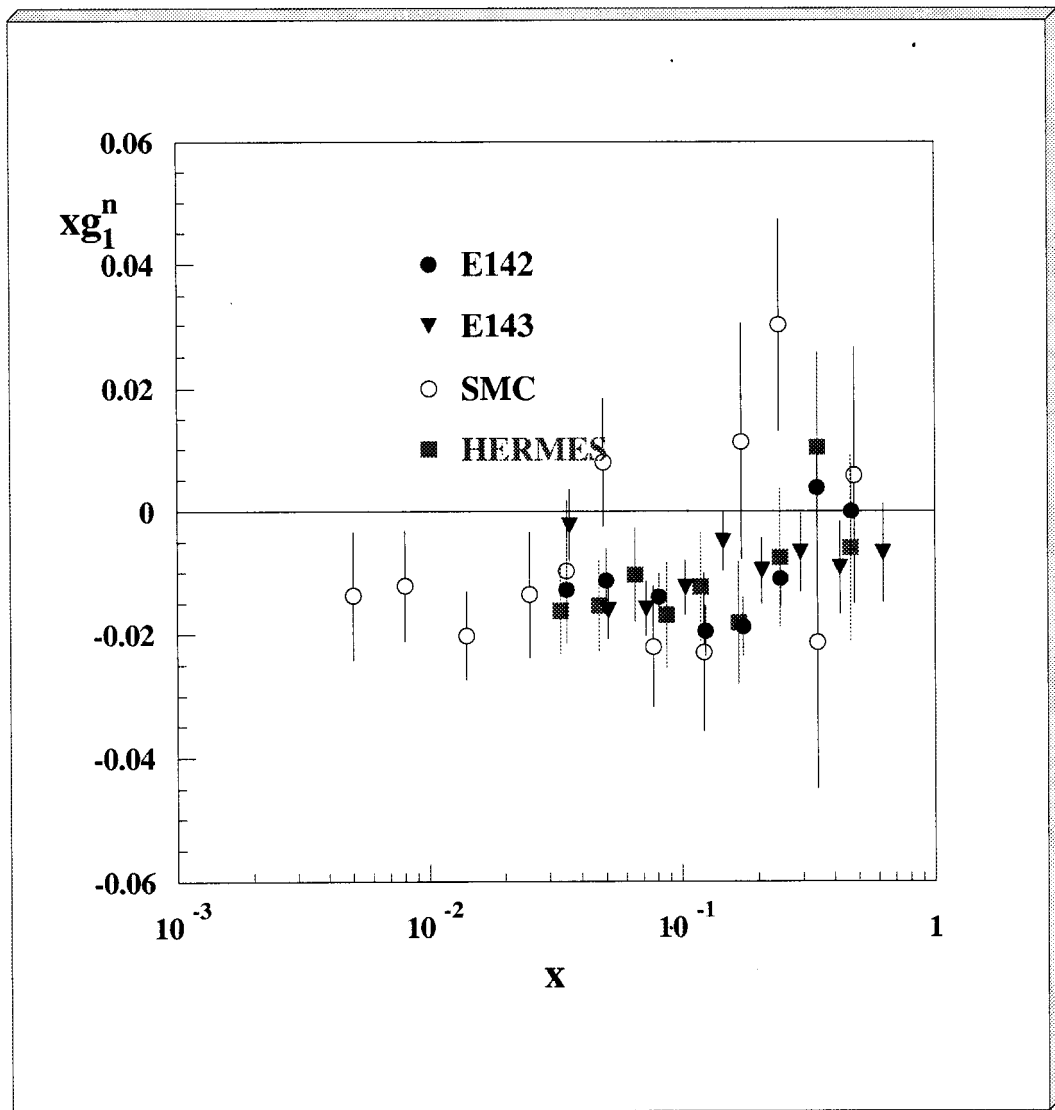


Figure 2.2. World results on $xg_1^n(x)$ before E154

CHAPTER 3

THE SLAC 50 GEV BEAM

3.1 Introduction

The Stanford Linear Accelerator can accelerate electrons to energies of around 50 GeV. These electrons are subsequently transported through a beam line transport system to one of several possible experimental areas. Experiment E154 was performed in End Station A (ESA), which is reached from the accelerator output via the beam switchyard and the A-line beam transport system. In this chapter, the complete system will be described in some detail from the electron source through the A-line, which was significantly upgraded for E154. A sketch of some of the major parts of the laboratory is provided in Fig. 3.1.

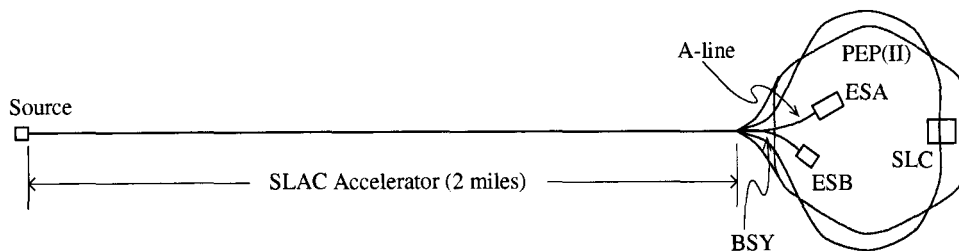


Figure 3.1. The Stanford Linear Accelerator Center (not to scale). Electrons are generated in the source on the left side of the figure, accelerated in the 2 mile linac (straight portion), then steered through the Beam Switch Yard (BSY) into one of the experimental areas. The hexagonal 'ring' is being upgraded to become the SLAC B-factory, and the Stanford Linear Collider experiment hall is labeled as SLC. E154 used the larger of the two end stations, ESA.

3.1.1 Accelerator Operation

Operators at the Main Control Center (MCC) controlled the accelerator using a computer interface which allowed them to operate and monitor the many components from a single location. All the magnets, klystrons, cooling water pumps, beam position monitors, etc. were under this computer control. The experimenters had no direct access to the accelerator operation. If the beam was not meeting specifications, the operators were asked to improve it, and generally they could adjust various components to improve the beam quality. The great majority of components were adjusted automatically by the computer control program using both fast and slow feedback loops to keep the beam well conditioned and centered on the target at the correct energy on a pulse by pulse basis. This computer control was also the first stage in the safety system as any malfunctioning components would be detected by the various monitors, forcing the control program to shut the beam source off. There were additional hardware safety features such as radiation monitors, burn-through monitors, and interlocked gates into the experiment hall, which will not be discussed here.

3.2 Polarized Source

The polarized electron source, located at the beginning of the accelerator in sector zero, produced the polarized electrons used in the experiment. It consisted of a strained gallium-arsenide crystal which was illuminated by circularly polarized laser light. The photoelectrons produced by the laser light were also polarized, and could subsequently be accelerated for use in the experiment.

Pure gallium-arsenide crystals have been used in the past as photo-cathodes to produce polarized electrons. However, the band structure of GaAs is such that there is a degeneracy between the valence bands, limiting the polarization of photo-

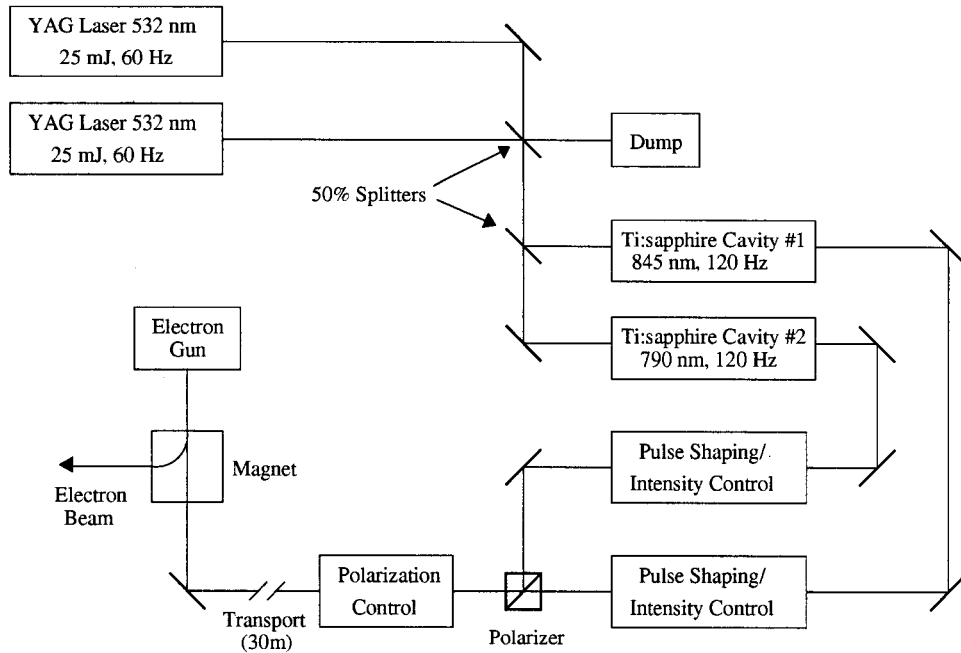


Figure 3.2. The SLAC polarized electron source laser system

electrons from a pure GaAs crystal to a maximum of 50%. It is possible to remove this degeneracy through the addition of a substrate of $\text{GaAs}_{1-x}\text{P}_x$. The small additional amount of phosphorous changes the crystal lattice constant which *strains* the pure GaAs crystal enough to lift the degeneracy [51], thereby allowing polarizations approaching 100%.

The source was originally designed to be used with the Stanford Linear Collider program, for which the operating characteristics were optimized. Whereas a short, 1 ns beam pulse or ‘spill’ was needed by the collider program, the E154 experiment required a longer beam spill of 250 ns. This necessitated the use of a totally different laser system, consisting of a YAG pumped Ti:Sapphire laser which was optically chopped to the correct spill length of 250 ns [52]. A schematic of the laser system used for E154 is shown in Fig. 3.2.

The polarization of the photoelectrons emitted from the strained GaAs photocathode was defined for each pulse using voltage controlled $\lambda/4$ plates, also known as Pokels cells, which determined the laser photon polarizations which could reach

the photocathode. The Pokels cells transformed the laser radiation polarization from linear to circular. The helicity of the circular polarization could be rapidly switched by changing the voltage to the birefringent crystal of the Pokels cell.

In order to minimize systematic uncertainties, the polarization was switched in a pseudo-random fashion. The algorithm consisted of a 33-bit shift-register and an exclusive ‘OR’ of bits 19 and 32 which was subsequently input into bit 0. A schematic of the sequence generator is shown in Fig. 3.3. This sequence generates an equal number of ones and zeros in a ‘random’ and yet predictable way. Since the sequence can be predicted once a 33 bit sequence (the seed) is known, the expected polarization of any pulse can be compared with the generated values as a consistency check.

Some of the properties of the generated sequence include the following:

- The length of the sequence is $2^{33} - 1$, meaning it will not repeat itself for 2-1/4 years of nonstop running at 120 Hz.
- All possible 33-bit sequences, except 33 consecutive zeros, are sampled exactly once during a complete cycle.
- The probabilities of ones and zeros are exactly equal.
- Any 33-bit sequence determines the seed, allowing a projection of the sequence forward or backward in time.

The generator was contained in a CAMAC module known as a Polarization MONitor (PMON) controller. It controlled the high voltage pulser for the Pokels cell, which in turn defined the laser light polarization direction and subsequently the electron beam helicity. Other PMON modules were connected to the generator allowing access to the polarization bit at other locations in the laboratory. The PMON polarization bit was one of the four methods of determining the beam

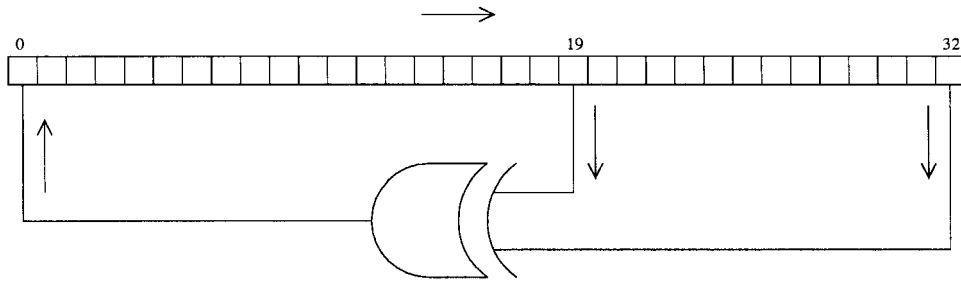


Figure 3.3. The pseudo random bit generator schematic. Arrows show the direction of information flow. The upper set of squares represents a 33-bit shift register, and the lower symbol is an exclusive ‘OR’ logic gate.

polarization sign available to E154. The other three methods were the so-called MACH lines, the high voltage VETO lines, and of course the Møller system as a final check on the validity of all these sources. These systems are described in [53].

3.3 The SLAC Accelerator

Electrons are accelerated by electric and magnetic fields. However, only electric fields can increase the kinetic energy since static magnetic fields act to produce a force in a direction perpendicular to the momentum. Once an electron reaches several MeV of kinetic energy, its velocity becomes very close to the speed of light. This allows the use of the very strong electric fields of microwaves, traveling in phase with the electrons through a disk-loaded wave-guide, to accelerate the electrons to higher energies. A longitudinal electric field (only possible in a wave guide) is produced, which is timed so the electrons are at the peak of the electric field wave. This technique, has been used in electron linear accelerators for nearly 50 years. The SLAC accelerator uses 2856 MHz microwaves produced by 250 high power (60 kW average, 50 MW peak) klystrons spaced every 40 feet along the 10,000 foot (about 2 miles) accelerator. The accelerator is straight to avoid energy loss due to synchrotron radiation (see Eq. (3.1)), and hence called a linear accelerator, or

linac. It is the premier example of its type in the world, and is described in much more detail by Neal [54].

Many parts of the accelerator have been improved over the years, although the actual disk-loaded wave guide is the same one built in 1962-1966. One of the most significant upgrades, which was relevant to the experiment in this thesis, was the implementation of the Stanford Linac Energy Doubler, or SLED, which increases the microwave power delivered to the beam electrons by using microwave cavities to store the power and release it suddenly to the accelerating sections [55]. Using this system allows the same accelerator, originally designed to generate about 25 GeV electrons, to double this energy to over 50 GeV. However, there is a drawback to using the SLED system in that the pulse length during which the electron beam has a constant energy profile is reduced to just a few nanoseconds. This is not a problem for the Stanford Collider Program, which requires very short (1/3 ns) pulses. However this experiment required as long a pulse as possible to spread the very high data rate out in time and reduce 'dead-time' effects in the detectors and electronics.

Fortunately, an operating procedure was found whereby the SLED system could be used, and the beam pulse length simultaneously increased to nearly 250 ns [56]. The technique involved adjusting the timing for each klystron to fill in a larger time window with the many high power peaks, and adding a second phase inversion to some of the SLED cavities which reduced the energy gain in the middle of the pulse while increasing it at the end of the pulse. Six of the thirty accelerator sections were implemented with this additional inversion. A full description of the technique and final beam characteristics are described in reference [56].

3.4 The A-line

The ‘A-line’ is the beam transport system, shown in Figs. 3.1 and 3.4, which conveyed the accelerated electron bunches from the output end of the linac into End Station A (ESA). Historically, it was the first beam line in operation at SLAC, with the first beam appearing in ESA in November of 1966 [57]. It was originally designed to handle the maximum linac energy at that time of about 25 GeV, and was used with very little modification for nearly 30 years. This experiment, however, required the present-day full linac energy using the SLED system of 50 GeV in order to investigate the spin structure functions at small x values. Accordingly, an upgrade of the A-line was proposed and implemented as an integral part of E154.

As part of the upgrade, the entire A-line was refurbished, and rebuilt where necessary. All beam monitoring and control systems, some of which had been in place for thirty years, were upgraded to modern standards. The most significant change, however, was an increase in the number of dipole bend magnets from eight to twelve. The additional four were salvaged from the now defunct B-line, and added to the original eight. All twelve dipole magnets were completely refurbished before final placement in May through July of 1995.

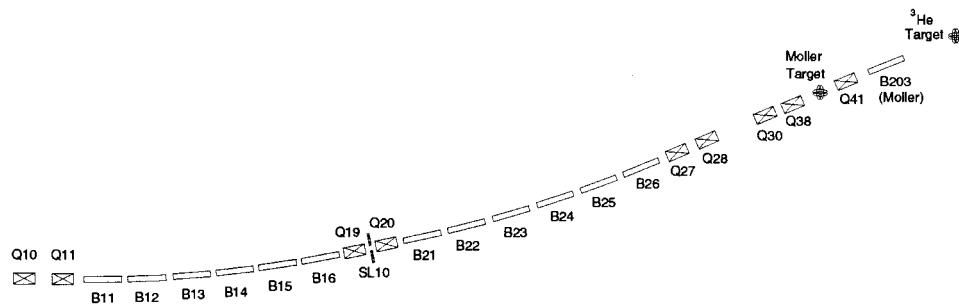


Figure 3.4. Schematic (not to scale) of the A-line magnetic elements. Several small magnets between the accelerator and Q10 are not shown, including the pulsed magnets which add a $1/2^\circ$ bend. Only the momentum-defining slits, SL10, are shown. The quadrupoles Q30 and Q38 were not used during most of E154.

3.4.1 Synchrotron Radiation Energy Loss

At the elevated beam energy of 50 GeV, synchrotron emission became a significant factor, and had to be well understood in order to account for energy losses and electron spin precession effects. An electron of energy E , traveling along a circular trajectory of radius R , emits synchrotron radiation according to

$$P_{inst} = \frac{2}{3} \frac{r_e c}{(m_e c^2)^3} \frac{E^4}{R^2}, \quad (3.1)$$

where P_{inst} is the instantaneous power radiated by the electron, m_e is the electron mass, $r_e \equiv e^2/4\pi\epsilon_0 m_e c^2$ is the classical electron radius, and c is the speed of light [58]. The energy loss may be obtained by integrating the instantaneous power along the electron trajectory corresponding to the time differential dt :

$$\Delta E = \oint P_{inst} dt, \quad (3.2)$$

where the path is along a circular arc, so $s = R d\theta = c dt$. This leaves

$$\Delta E(\theta) = \int_0^\theta P_{inst} \left(\frac{R}{c}\right) d\theta. \quad (3.3)$$

Evaluating the integral yields the energy loss due to synchrotron radiation for an electron deflected through an angle θ along a circular path of radius R ,

$$\Delta E(\theta) = \frac{2}{3} \frac{r_e \theta}{(m_e c^2)^3} \frac{E^4}{R}. \quad (3.4)$$

Combining all the constants this becomes

$$\Delta E(\theta) = 1.407927 \times 10^{-5} \frac{\theta E^4}{R}, \quad (3.5)$$

where θ is measured in radians, E in GeV, and R in meters.

The dependence on the fourth power of the energy is very significant, since it causes a factor of sixteen increase in the radiated power and energy loss for a doubling of the beam energy. Thus, while the synchrotron radiation was fairly

negligible at 25 GeV in the A-line, it represents a loss of nearly 500 MeV for 50 GeV electrons. This was one of the reasons additional dipole magnets were added to the A-line during the upgrade. By making each bend shallower the bend radius was increased from 57.285 m to 85.927 m [59], so as to reduce the synchrotron energy loss.

Synchrotron emission changes the beam energy at each of the twelve bend magnets. Each quadrupole also contributes, but to a much lesser degree, since the bend radius is very large if the beam is centered in the quadrupole. Because of this, one can either adjust the bend angle for each dipole so that each is slightly different, or adjust the field strength of each bend magnet and maintain the 2.00 degree bend for each. The latter option was chosen in order to retain the ability to use the A-line for lower energies where synchrotron emission is negligible. However, there was only one large power supply driving all twelve bend magnets connected in series. The solution to this problem was the use of separate ‘trim’ coils to modify the magnetic fields appropriately. It was decided that the synchrotron loss was gradual enough for pairs of magnet trim coils to be connected in series, resulting in an additional six small trim power supplies.

3.4.2 Spin Precession and Beam Energy

Another facet of the problem of increased synchrotron emission in the 50 GeV A-line, described in the preceding Section, was due to the precession of the electron spins in the beam. Because the spin precession depends on the energy of the beam electrons, which is modified by the emission of synchrotron radiation, the two effects become convolved together. The spin precession angle was important because the longitudinal beam polarization peaked in the End Station for precessions of an integral number of π radians.

In general, an electron whose path is bent by a magnetic field undergoes a precession of its spin described by

$$\theta_{prec} = \gamma \left[\frac{g-2}{2} \right] \theta_{bend}, \quad (3.6)$$

where $\gamma = 1/\sqrt{1-v^2/c^2}$ is the relativistic gamma of the electron, $g = 2.002319314$ [22] is the electron g -factor, and θ_{bend} is the angle through which the electrons are deflected by the magnet. For electrons the constants may be combined using

$$E = \gamma mc^2 \quad (3.7)$$

and the electron mass of $0.51099907 \text{ MeV}/c^2$ to generate

$$\theta_{prec} = 2.269391 E \theta_{bend}, \quad (3.8)$$

where E is measured in GeV. Ignoring synchrotron energy losses for the moment, the precession angle can be calculated for the A-line to determine the so-called *magic* energies at which the beam is longitudinally polarized in the end station after traversing the A-line bend of 24.5° . Specifically, an energy increase of 3.2374 GeV corresponds to an extra π radians of precession. Thus there are 15π radians of precession for a beam energy of 48.56 GeV (ignoring synchrotron losses).

However, as described in Section 3.4, the synchrotron losses are not negligible in calculating the spin precession at 48 GeV in the A-line. Equation (3.8) can be combined [62] with (3.1) to become

$$\theta_{prec} = 2.26938 \int_0^{\theta_{max}} d\theta_{bend} \left[E - 1.6385 \times 10^{-7} E^4 \theta_{bend} \right]. \quad (3.9)$$

This evaluates to

$$\theta_{prec} = 2.269391 \left[E\theta_{max} - 1.6385 \times 10^{-7} E^4 \frac{\theta_{max}^2}{2} \right], \quad (3.10)$$

which, using the A-line bend angle of $24.5^\circ = 0.427606$ radians, generates

$$\theta_{prec} = 0.9704E - 3.5031 \times 10^{-8} E^4 \quad (\text{rad}). \quad (3.11)$$

This result can be extended to next order by taking account of the θ -dependence of E^4 , yielding an additional term

$$+ 6.5 \times 10^{-15} E^7, \quad (3.12)$$

which is negligible for the energies of interest. With the addition of synchrotron losses to the formula (3.11), a set of magic beam energies for the new A-line can be calculated, and are shown in Table 3.1.

Table 3.1. Magic beam energies for which the electron polarization is longitudinal in ESA, and the corresponding beam energy when synchrotron energy losses are taken into account.

θ_{prec}	E_{linac} (GeV)	E_{ESA} (GeV)
14π	45.478	45.178
15π	48.759	48.362
16π	52.056	51.542

3.4.3 Quadrupole Magnets

The beam in the A-line had to be focused using quadrupole magnets to keep it from diverging outside the beam pipe. The magnetic field \vec{B} in a quadrupole is zero in the center and becomes stronger at positions radially away from the axis. This allows a quadrupole to act like a lens, doing nothing to charged particles traveling along the central axis, but deflecting them more and more as they travel through the quadrupole magnet with greater and greater offsets from the central axis. Quadrupoles are designed with pole tip shapes such that they approximate a field which is proportional to the radius r as much as possible,

$$|\vec{B}| = Ar, \quad (3.13)$$

where A is some constant and r is the radius measured from the central axis of the quadrupole. Because of the direction of the \vec{B} -field lines, a quadrupole focuses in one plane but defocuses in the other.

3.5 Beam Line Optics Calculations

The passage of a charged particle through a magnetic field is described by the Lorentz force, which relates the force \vec{F} on the charged particle to its charge q , the electric and magnetic fields, \vec{E} and \vec{B} , and the velocity \vec{v} of the particle,

$$\vec{F} = q \left(\vec{E} + \frac{1}{c} \vec{v} \times \vec{B} \right). \quad (3.14)$$

A series of calculations may be made using this equation, describing how a beam of charged particles will react to a series of magnets forming a beam line. There are two standard computer programs which perform these tasks: TRANSPORT and TURTLE (Transport Unlimited Rays Through Lumped Elements).

In general, a charged particle in a beam line can be described by a six parameter vector $X = |x, x', y, y', l, \delta\rangle$ where x and y are the horizontal and vertical offsets from the central beam line axis, x' and y' are the angles between the central axis and the particle's momentum in the horizontal and vertical planes, l is the difference in path length between the particle's path and the central trajectory, and δ is the fractional deviation of the momentum from the central beam line momentum p_0 : $\delta \equiv (p - p_0)/p_0$. An initial state $|X(0)\rangle$ can be propagated through a beam line model, and the states $|X(i)\rangle$ determined at any desired point in the beam line. Both TRANSPORT and TURTLE calculate how particles propagate through beam line elements by determining a *transfer* matrix R for each element such that

$$|X(i)\rangle = R(i) |X(i-1)\rangle, \quad (3.15)$$

where $|X(i-1)\rangle$ is the state of the beam before the element, and $|X(i)\rangle$ is the state after the element.

One can easily extend Eq. (3.15) to second order in X using

$$X_i(n) = \sum_j R_{ij}(n) X_j(n-1) + \sum_{j,k} T_{ijk}(n) X_j(n-1) X_k(n-1). \quad (3.16)$$

TRANSPORT can calculate both the R and T matrices. However, the normal use is to ignore the second order effects of the T matrix. This formalism has the advantage of being very easy to extend to several elements, since

$$|X(i)\rangle = R_{total}|X(0)\rangle \quad (3.17)$$

$$= R_i R_{i-1} R_{i-2} \dots |X(0)\rangle, \quad (3.18)$$

where R_i represents the transfer matrix for the i^{th} beam element.

The transfer matrix formalism is valid for each individual particle in the beam. Normally however, the beam as a whole, consisting of many individual particles, is the object of interest. The TRANSPORT formalism, which is described in detail in [60], provides a method for propagating a beam ‘shape’ through an optics model.

An n-dimensional ellipsoid is defined

$$X^T(0)\sigma^{-1}(0)X(0) = 1, \quad (3.19)$$

where $X^T(0)$ is the transpose of the coordinate vector $X(0)$ and $\sigma(0)$ is a real, positive definite, symmetric matrix. The volume of the n-dimensional ellipsoid defined by $\sigma(0)$ is

$$V = \frac{\pi^{n/2}}{\Gamma(n/2 + 1)} \sqrt{\det(\sigma)}, \quad (3.20)$$

and the area of a projection in a given plane is given by

$$A = \pi \sqrt{\det(\sigma_i)}, \quad (3.21)$$

where σ_i is the submatrix corresponding to the given plane. This is the *phase space* occupied by the beam. Note that there are in general six coordinates in phase space, namely the six variables which describe the beam. Using

$$R^{-1}R = 1, \quad (3.22)$$

Eq. (3.19) may be rewritten as

$$X^T(0) (R^T (R^T)^{-1}) \sigma^{-1}(0) (R^{-1}R) X(0) = 1, \quad (3.23)$$

which transforms to

$$[RX(0)]^T [R\sigma(0)R^T]^{-1} [RX(0)] = 1. \quad (3.24)$$

Using Eq. (3.15) and defining

$$\sigma(1) \equiv R\sigma(0)R^T, \quad (3.25)$$

one finds

$$X^T(1)\sigma^{-1}(1)X(1) = 1, \quad (3.26)$$

which is easily identified in analogy with Eq. (3.19) as the n-dimensional ellipsoid at the next beam element. As a result, only the transfer matrix R is needed to determine the phase space occupied by the beam from one element to the next. It can be shown that the square roots of the diagonal terms of the σ matrix are a measure of the beam size for each coordinate. The off-diagonal terms specify the orientation of the phase-space ellipse in six-dimensional space.

TURTLE uses the same matrix formalism as TRANSPORT to propagate a ray (a particle) through a magnetic element, but does not attempt to multiply all the R (and T) matrices together [61]. Rather it propagates one ray at a time through one element at a time. This allows investigations into several effects inaccessible to TRANSPORT. In particular, chromatic effects are accounted for since off-energy rays are explicitly propagated through at their own energy. Collimators may be modeled, since the x,y coordinates of the ray are available at any point, and the ray can be stopped if it extends beyond a maximum value for any coordinate. TURTLE also allows one to investigate non-Gaussian distributions for any coordinate whereas TRANSPORT, which assumes a Gaussian distribution, simply returns the widths of these distributions as the coordinates.

TURTLE was augmented to include the CERN HBOOK histograms and NTUPLES, which allowed the results to be analyzed with modern programs such as

PAW. The original histogram routines of TURTLE were modified to fill HBOOK histograms and a new beam element was defined which added five entries to the NTUPLE for each of the five relevant coordinates at that point, x , x' , y , y' , and δ . As the program ran, an event was added to the NTUPLE for each ray with the ray's five coordinates at each of the points in the beam line where the NTUPLE element was specified. This allowed the investigation of correlations between coordinates not only at a given point, but also between different points along the beam axis.

The TRANSPORT and TURTLE programs are both set up to read the same input file which lists the beam line elements sequentially and contains commands instructing the programs how to operate. Each beam line element is described by a card in the input deck, using terminology from the early 1970's when these codes were written. Types of elements include drift spaces, dipole magnets, quadrupole magnets, slits, and a number of other specialized devices. These programs also calculate where each element must be positioned in order to be centered in the beam. For example, if one inputs a 50 GeV electron bunch and sends it through a dipole with a given length and field strength, followed by a drift space, and another magnet, the (x, y, z) coordinates which center the beam through the magnets will be determined, although only the path length distance, s , is given for each element. Thus the complete deck for the A-line also contains the specifics of the alignment, and one can determine detailed beam properties from this file.

Some results of beam line studies using TURTLE are shown in Figs. 3.5-3.7. These also demonstrate the use of the added NTUPLEs. Figs. 3.5 and 3.6 show the x - y beam cross section at four locations in End Station A for two different input momentum distributions: $\delta = 0.1\%$ and $\delta = 0.5\%$. Fig. 3.7 shows the correlation between the input (from the accelerator) momentum distribution and the x, y distributions at the target position for an input δ of 1%. The strong dependence shown only appears with $\delta \approx 1\%$ or larger. E154 generally ran with

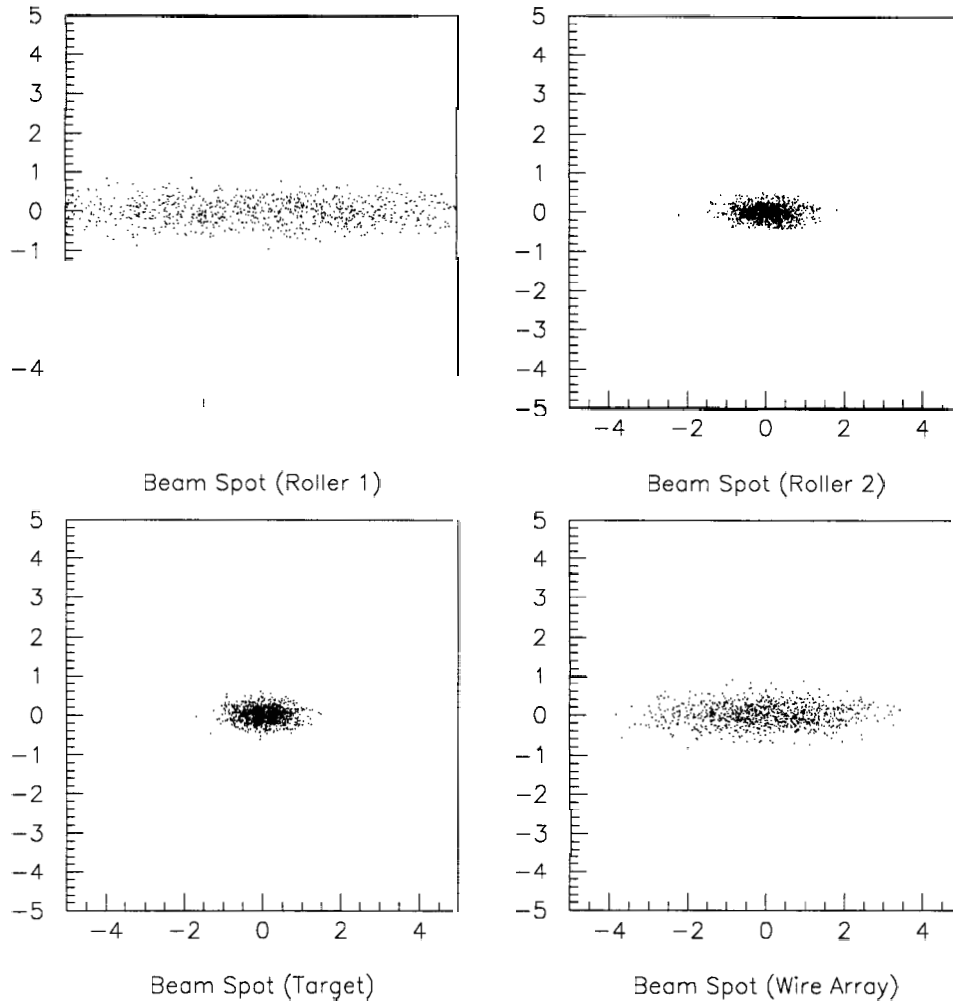


Figure 3.5. Beam x - y cross-sections (spots) at the roller screens, the target and the wire array generated by TURTLE using $\delta = 0.1\%$. Dimensions are in mm.

the SL10 slits limiting $\delta < 1.07\%$, but in fact the accelerator provided a much narrower momentum distribution with a width between 0.1% and 0.3% .

3.6 A-Line Optics During E154

The E154 experiment began data acquisition a couple of weeks after electrons were sent through the upgraded A-line for the first time. As a result, several different *tunes* were used throughout the experiment in an attempt to optimize the beam conditions at the target for the requirements of the experiment. These

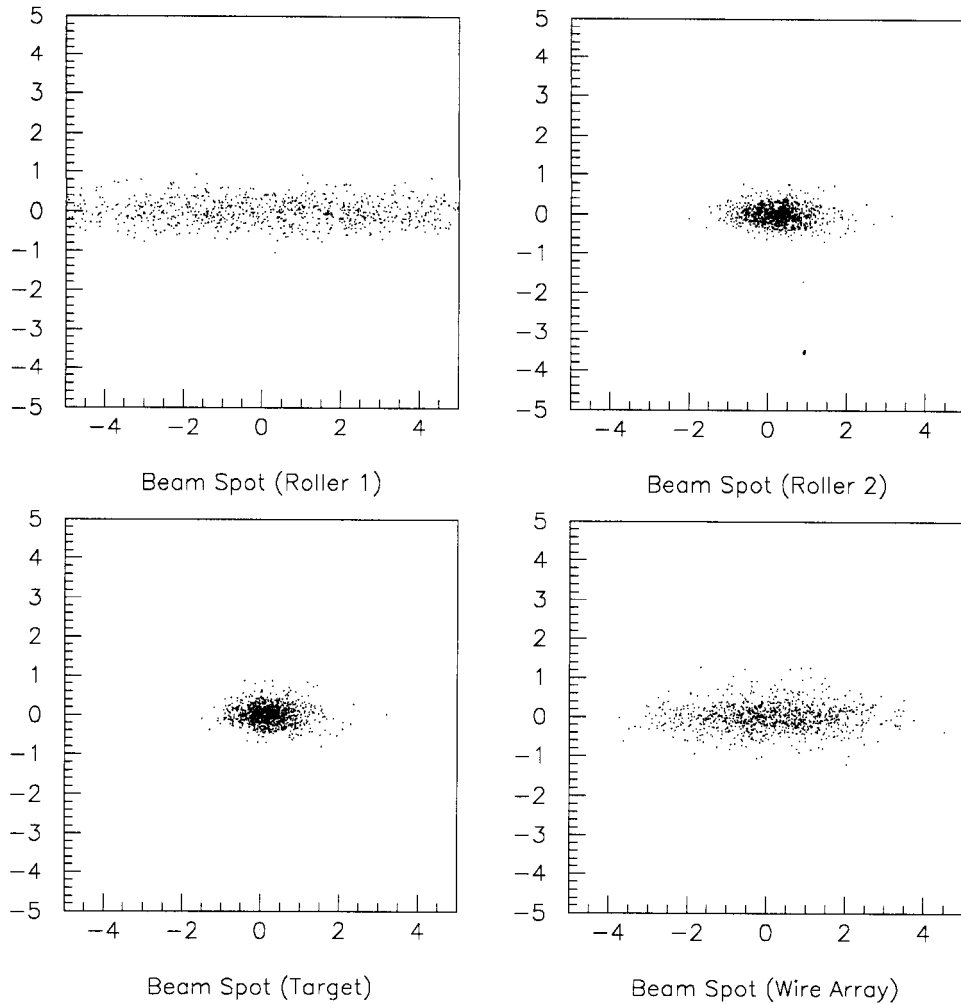


Figure 3.6. Beam x - y cross-sections (spots) at the roller screens, the target and the wire array generated by TURTLE using $\delta = 0.5\%$. Dimensions are in mm.

included the need to minimize the spot size to limit beam halo interactions with the target cell walls, balanced against enlarging the beam spot size on the target cell to reduce local beam heating and radiation damage, which were thought to be contributing factors causing the target cells to explode.

In addition to understanding the beam dynamics well enough to specify the beam spot size on the target cell, it was important to be able to accurately determine the beam parameters at the target from their measured values at the wire array 9.23 m downstream. A thorough understanding of the optics of each different tune

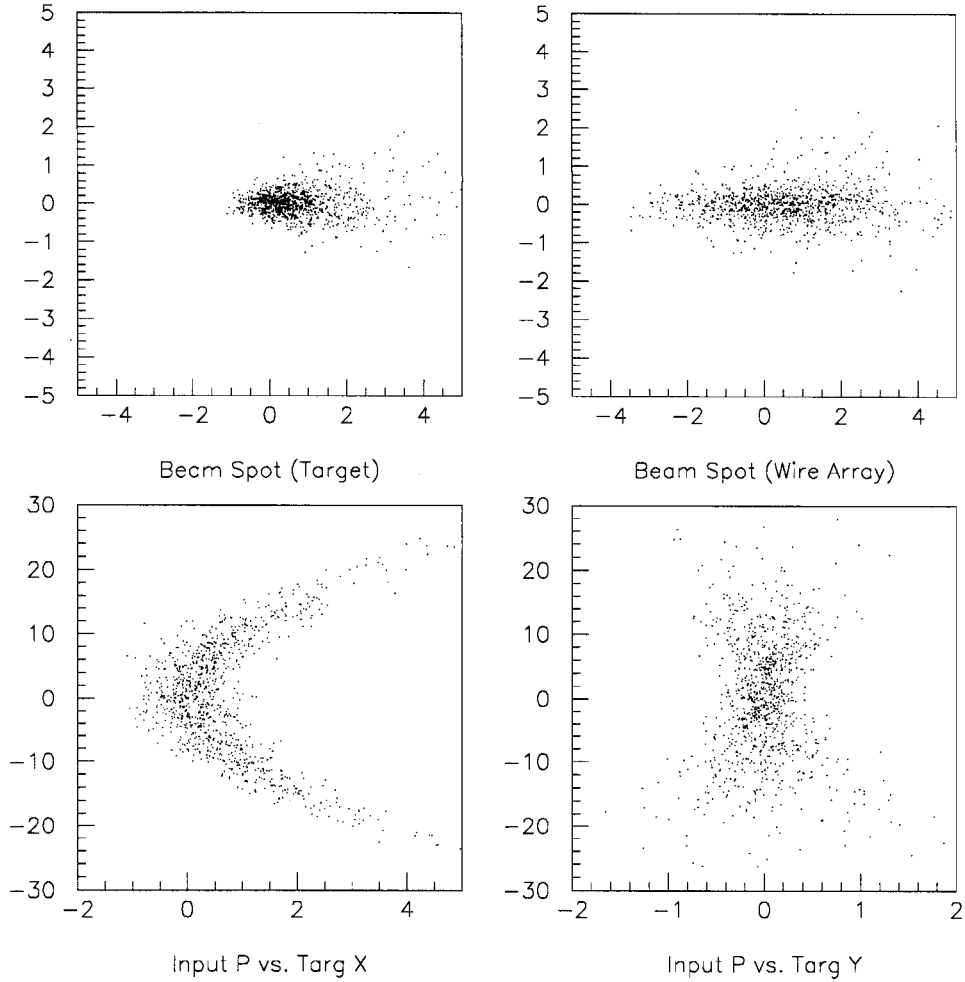


Figure 3.7. Beam x - y cross sections (spots) and correlations between input momenta and target coordinates generated by TURTLE using $\delta = 1.0\%$ Dimensions are in mm for the X and Y coordinates, and 0.1% for the momentum coordinate.

was required for this. The wire array measured both the position of the centroid of the beam, and the horizontal and vertical dimensions of the beam. It is described in greater detail in Section 3.7.1.4.

The original run plan was to place the beam *waist*, or narrowest point, at the target position so beam halo would be as far from the target cell walls as possible. This was done until run 2649, after which an attempt was made to spread the beam out a bit more at the target to reduce beam heating and radiation damage on the target cell glass windows. After run 3146 the beam cross section at the target

was increased even further. Besides these overt changes which were requested by the experimenters, several slightly different tunes, brought about by attempts to improve the beam characteristics, were used during the running period, and are described in Table 3.2.

Table 3.2. A-line quadrupole magnet fields as a function of run number. All units are kG·m/m. The breaks in the run numbers correspond to unanalyzed special runs.

Run #	Q19	Q20	Q27	Q28	Q38	Q41
1329-1387	95.4	20.6	-131.9	134.3	-41.2	83.0
1465-1486	94.9	20.5				82.6
1525-1756	96.8	20.9			-48.0	
1825-2042	96.5	20.1	-134.2			
2070-2156	96.1	20.5	-140.7	141.0		43.5
2157-2166						26.6
2169-2196						25.2
2202-2278						35.1
2288-2562			-132.3	134.3	-45.2	85.1
2649-2900			-135.7		0.0	52.5
2936-3085			-138.8	141.2		35.4
3087-3099			-139.8	139.2		48.4
3146-3347	100.0	20.7	-135.7	134.3		52.5
3354-3369	96.0					
3460-3616					-1.2	

To show that the TRANSPORT calculations of the beam optics were correct, two scans were performed by varying the magnetic field of the last quadrupole in the A-line, Q41. The first scan was made very early in the experiment and consisted of runs 1144 through 1156. These runs were not analyzed in detail. The second scan, consisting of runs 3385 through 3390, was done much later and the results are shown in Fig. 3.8. The A-line optics information was also very useful during Møller runs which used a different tune due to the placement of the Møller target nearly 50 m upstream of the main ^3He target. As shown in Fig. 3.4, the quadrupole magnet Q41 was positioned between the Møller target and the Møller magnet and was thus turned off during Møller runs.

Q41 Scan 11/22/95

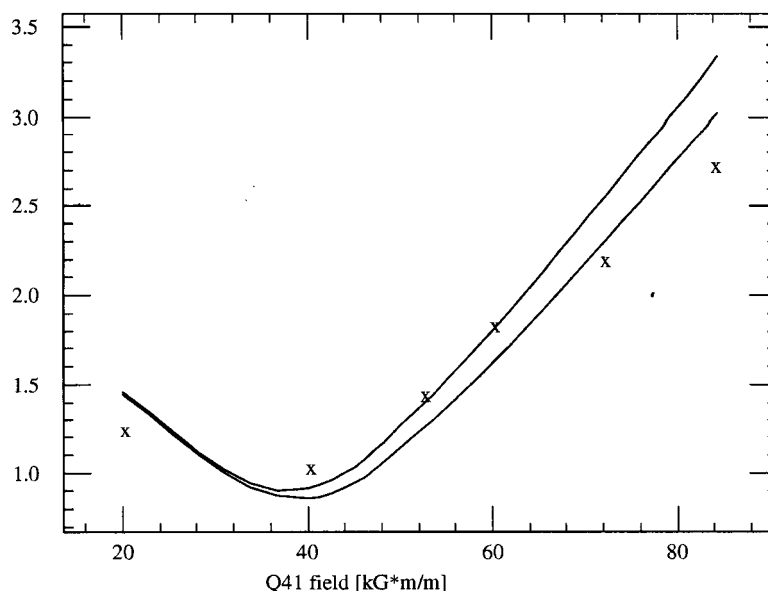


Figure 3.8. Results from the Q41 quadrupole field scan of runs 3385-3390. The two curves are the TRANSPORT results, with the lower curve having an input emittance in x half as large as the upper curve. The X's are the beam 'widths,' or spatial extent (in \hat{x}) measured with the wire array.

3.7 Beam Monitoring and Systematics

Because the asymmetry measured in this experiment is of the order of 10^{-4} , it was imperative to make sure that all other possible effects were significantly smaller. In particular, any variations in the beam correlated with helicity could have posed a significant problem. Throughout the experiment many beam characteristics were monitored, and corrected as needed. However, it was not until the full analysis had been completed that it was possible to show that these beam systematic effects had negligible influences on the asymmetry measurement.

Several systematic beam effects relevant to the experiment were investigated. These included the charge asymmetry, energy asymmetry, and position asymmetries of the beam. The results of these investigations are presented in Chapter 5.

3.7.1 Beam Monitors

In order to measure these various beam asymmetries, several specialized ‘monitors’ were required. These monitors were used to keep track of the beam characteristics on a pulse to pulse basis. The characteristics of interest included the position and size of the beam spot at the target, the energy and energy spread of the beam, the polarization, and the amount of ‘halo’. Beam halo refers to beam particles which were outside the main beam spot, and were typically off-energy, often appearing as a ‘halo’ around the main beam when viewed on a fluorescent screen.

During initial tuning of the A-line transport system, two roller screens of ZnS were frequently placed in the path of the beam and viewed via closed-circuit television. This allowed the accelerator operators to adjust the corrector magnets and quadrupoles to produce a reasonably ‘clean’ beam at the target, *i.e.*, a beam centered on the target cell with minimal halo. The roller screens, however, interfered with the beam, creating a large flux of particles scattered outside the main beam, and consequently were removed during data taking.

During normal running, three ‘spill monitors’ were used which were very sensitive to off-energy particles, mis-steered beam, and halo. These were the ‘bad’ spill monitor, the lead-glass monitor, and the ‘good’ spill monitor. The term ‘spill’ is used to refer to one 250 ns beam pulse. Two additional devices were used to monitor the beam position: the wire array, and the travelling wave monitor. The wire array also measured the beam spot size.

3.7.1.1 Bad Spill Monitor

The bad spill monitor was a small scintillator panel placed slightly downstream of quadrupole Q41 in the ESA alcove. It was mounted (actually simply placed) on the floor below the beam pipe. Its main purpose was to monitor *bad* spills. This

location was well suited for this purpose since ideally no beam particles should be scattered from anything upstream of this monitor. However, in the case of halo, off energy electrons, or simply mis-steered beam, electrons would scatter off the beam pipe and apertures in the A-line, and be detected in this scintillator. The bad spill monitor was attached to a photomultiplier tube to convert the scintillation light to an electrical signal which in turn was digitized using a LeCroy 2249 ADC in the Beam CAMAC crate in the ESA Counting House and written to tape along with the spectrometer data for each spill. For real time monitoring the signal was also sent to an oscilloscope which was monitored by closed-circuit TV. The TV signal was available to the accelerator operators who were instructed to try to minimize the bad spill signal.

3.7.1.2 Good Spill Monitor

The good spill monitor, named more in contrast to *bad* than due to any specific ability to detect *good* spills, was a scintillator panel 'mounted' slightly downstream of the target by simply placing it on the floor. The actual position was not critical as long as it remained constant throughout the experiment, as this monitor served primarily as a luminosity monitor. The luminosity, defined as the product of the incident beam current with the target thickness, was an important aspect since it was strongly dependent on the beam being steered through the center of the target cell. If any portion of the beam – halo for example – traversed the glass walls of the target cell, the luminosity would increase dramatically because the walls were oriented parallel to the beam and were 20 cm thick (in the beam direction) instead of the usual 0.020 mm of the target cell endcap windows. Thus spills with halo, or mis-steered beam, produced larger signals in the good spill monitor.

Due to the fact that the luminosity was actually quite large, the phototube voltage was kept quite low, typically 700 to 800 V to avoid saturation. During the

experiment a number of instances arose where the signal appeared to be showing an odd spill time structure. On lowering the phototube voltage, this structure disappeared. Thus the interpretation of this signal required some care. The good spill signal, like the bad spill signal, was digitized by a LeCroy 2249 ADC in the Beam CAMAC crate in the ESA Counting House. It also was sent to the same oscilloscope as the ‘bad spill’ monitor signal and monitored via closed-circuit TV by both the experimenters and the accelerator operators. As with the ‘bad spill’ signal, the goal was to keep the ‘good spill’ signal both small and constant throughout the full 250 ns spill duration.

An attempt was made to *digitize* the waveforms of both the bad and good spill monitor signals in order to monitor the beam spill time structure. Copies of the signals were fanned out and sent through a series of successively longer delays to a multichannel ADC with a narrow (30 ns) gate, in an attempt to measure the charge in 30 ns increments. Unfortunately, this system was never truly debugged or calibrated. Also, the spill length was increased from the anticipated 200 ns to nearly 250 ns, so these time-sliced spill signals did not cover the full spill duration. Because of these shortcomings, this system was not actually used in the analysis, but the information does exist on the data tapes.

3.7.1.3 Lead-Glass Monitor

The third ‘spill monitor’ was a single lead-glass block placed near the Møller magnet, and shielded by several inches of lead. The purpose of this detector was to monitor high energy electrons which were being scattered upstream of the target for whatever reason. By contrast, the good and bad spill monitors detected charged particles with energies as low as a few MeV, from a beam of nearly 50 GeV. The spectrometers had an acceptance starting at about 8 GeV, so these low energy particles were mostly irrelevant in terms of the physics data. However, high energy

electrons, which were possibly close in energy to the 48.3 GeV beam energy, were within the spectrometer momentum acceptances. Because these electrons were likely to be off-center (due to steering and quadrupole magnets upstream), they were more likely to scatter off the glass target cell walls and into the spectrometers, changing the measured cross sections. This motivated the use of the lead-glass monitor as a measure of high energy background.

Like the good and bad spill monitors, the lead-glass monitor was attached to a phototube whose signal was sent upstairs to the beam CAMAC crate in the ESA counting house and digitized using a LeCroy 2249 ADC channel. However, unlike the good and bad spill signals, this signal was merely written to tape and not monitored on the oscilloscope. The lead-glass monitor was added later in the experiment, and was thus only available after run 1368.

3.7.1.4 Wire Array Monitor

The wire array consisted of two identical planes of 30 parallel 5 mil diameter CuBe wires spaced 1.17 mm apart center to center and placed perpendicular to the beam. The two planes were separated by 10.7 cm along the beam direction and rotated by 90° relative to each other with horizontal wires closer to the target and vertical wires further downstream. The entire system was mounted 9.23 m downstream of the target in the central beam line. Each wire registered a signal proportional to the number of beam electrons incident on it. Thus, by measuring the signals from a series of wires, the spatial (x, y) parameters of the beam emittance, i.e. the beam cross section, could be determined for each spill.

The wire array operated as a secondary emission monitor (SEM). The parallel wires were placed between a set of collector plates which were maintained at a high positive voltage of +300 V. When the beam impinged on the wires, it knocked out electrons, which because of the potential on the collector plates were pulled

away from the wires. This in turn created a positive voltage pulse on the wire, due to the sudden removal of electrons, which could in turn be measured and used to determine the number of incident beam electrons striking a given wire.

With careful preparation, the wire signal response to the beam could be made linearly dependent on the beam current. This was accomplished by adjusting both the wire thickness and the collector potential to accommodate the range of beam currents anticipated. For example, the previous ESA experiment, E143, used a foil array consisting of thin foils positioned parallel (edge on) to the beam to provide a greater thickness in g/cm^2 than the wires used by E154. This was because the E143 beam currents were roughly ten times smaller, and simply achieving a ‘thick’ enough target to produce a usable signal required foils instead of wires.

The signals from each wire were amplified, and the charge digitized using a LeCroy 2249 ADC in the beam CAMAC crate in the ESA counting house. These ADC data were written to the raw data tape along with the other beam monitoring data.

3.7.1.5 Analysis of Wire Array Data

The wire array data were stored in two arrays of pedestal subtracted integers for the horizontal and vertical measurements respectively. These raw data were simply the charge detected on the individual wires, and hence were proportional to the fraction of beam current incident on each wire. They were analyzed by fitting a Gaussian with a constant background

$$f(x) = A + B \exp\left[-\frac{(x - x_0)^2}{2\sigma^2}\right], \quad (3.27)$$

as shown in Fig. 3.9. The four parameters A , B , x_0 , and σ were determined by fitting to the data using MINUIT, a software package from CERN for fitting functions. The x_0 parameter corresponded to the ‘centroid’ of the beam in units of wire number, and σ to the ‘width’. The other two parameters, A and B , measured

the constant background, and normalized the fit respectively. For each spill, a fit was performed for each of the two wire arrays (x and y). The centroid and width of the beam in the vertical and horizontal directions were used in the subsequent asymmetry analysis to distinguish usable beam spills from bad spills.

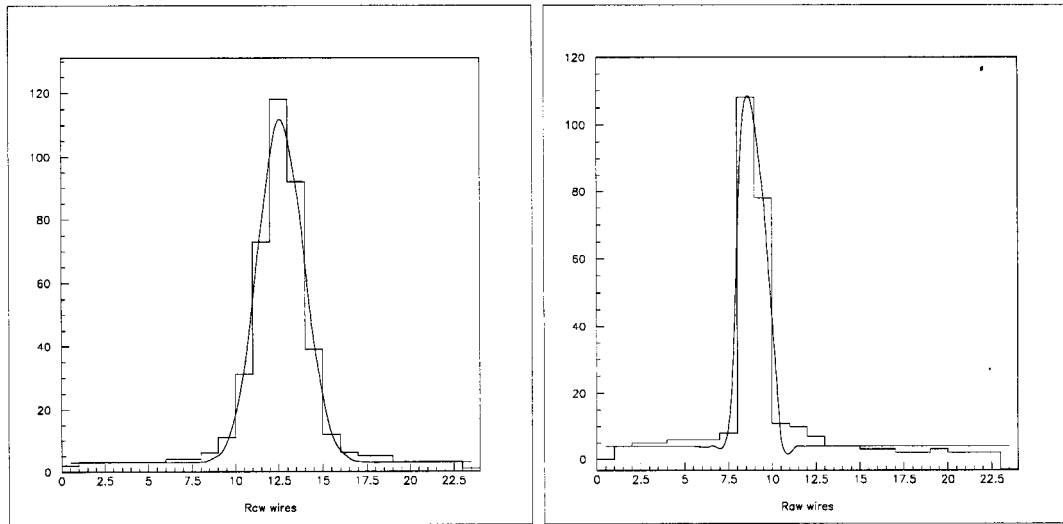


Figure 3.9. Typical data from the x (left figure) and y (right figure) wire arrays for a small spot with the MINUIT fit superimposed.

MINUIT was used for these fits, since the addition of a constant background term to the Gaussian ruled out the use of an analytic least squares fit to the data. A critical concern was also the small beam spot size in the vertical direction, typically only about 0.5 mm, which meant that only one, or at most two, wires in the wire array typically had any data above background, making a four parameter fit somewhat difficult. MINUIT, however, generated very reasonable looking fits to all the wire array data as demonstrated by the narrow fit in the right hand side of Fig. 3.9.

3.7.1.6 Toroids

In addition to the beam emittance characteristics, an important measurement was provided by two high precision toroids which determined the beam current for each spill with an accuracy of $\sim 0.1\%$. Because of the pulsed nature of the beam, a current is induced in a coil around the toroid due to the change in current in the beam. As the first beam pulse electrons pass through the toroid, a current begins to flow, which continues until the last electrons in the pulse leave, which causes the toroid current to stop. By carefully calibrating and measuring the induced charge on the toroid, the charge of the beam pulse passing through may be measured quite accurately.

3.8 Møller Polarimeter

The Møller polarimeter was used to measure the beam polarization in End Station A (ESA). Since the asymmetry of Eq. (2.102) contains the beam polarization as an explicit factor, it was important to measure the polarization as accurately as possible. Although the beam polarization might be known at the source, or even at the end of the linac, nothing was known *a priori* about the polarization in ESA due to the convolution of the electron spin precession and the synchrotron energy loss, described in section 3.4.2. As shown in Table 3.1, the electron spins precess 15π radians going through the 24.5° A-line bend at 48.759 GeV with the synchrotron energy loss factored in.

However, determining the synchrotron energy loss is not quite as simple as the idealized description in section 3.4.1. For example, the beam might be off-center in some of the magnets due to misalignment or bad steering correctors, thus changing the relevant bend radius for the energy loss formula. Additionally, quadrupole magnets, which were ignored in the earlier discussion, could alter the energy loss if the beam was off-center and experiencing an appreciable magnetic field.

Because of this, it was important to actually measure some of the parameters, and to empirically determine the beam energy yielding the peak electron polarization in the end station. This was accomplished by conducting an energy scan while measuring the polarization with the Møller system in ESA. In addition to the determination of the optimum beam energy, the Møller system was employed on a regular basis to monitor both the beam polarization value and sign. Fortunately, the measured value remained constant, within statistical fluctuations for the duration of the experiment.

3.8.1 Theory of Møller Scattering

Møller scattering refers to the scattering of electrons off electrons. In E154, polarized beam electrons were scattered off polarized atomic electrons in a target foil. The cross section for this process is given by [63]

$$\frac{d\sigma}{d\Omega} = \left[\frac{\alpha(1 + \cos\theta_{CM})(3 + \cos^2\theta_{CM})}{2m \sin^2\theta_{CM}} \right]^2 \left(1 + \sum_{i,j} P_B^i A_{i,j} P_T^i \right) \quad (3.28)$$

$$= \left(\frac{d\sigma_0}{d\Omega} \right)_{lab} \left(1 + \sum_{i,j} P_B^i A_{i,j} P_T^i \right), \quad (3.29)$$

where $(d\sigma_0/d\Omega)_{lab}$ is the unpolarized cross section in the lab frame, θ_{CM} is the scattering angle in the center of mass frame, m is the electron mass, P_B^j and P_T^i are the components (x,y,z) of the beam and target polarizations, respectively, and A_{ij} are the asymmetry components for Møller scattering. For measurements of longitudinally polarized electrons on a longitudinally polarized target, only the A_{zz} term is relevant, and is given by [63]

$$A_{zz} = \frac{-[7 + \cos^2(\theta_{CM})] \sin^2(\theta_{CM})}{[3 + \cos^2(\theta_{CM})]^2}. \quad (3.30)$$

This term is most sensitive for $\theta_{CM} = 90^\circ$ where the unpolarized cross section is 0.179 barn/sr and $A_{zz} = -7/9$.

The Møller asymmetry is defined the same way as the DIS asymmetry of Eq. (2.31), which, when combined with the full Møller cross section of Eq. (3.29), and under the assumption that only $A_{zz} \neq 0$, is

$$A_{Moller} \equiv \frac{\left(\frac{d\sigma_0}{d\Omega}\right)_{lab} [(1 + P_B^z A_{zz} P_T^z) - (1 - P_B^z A_{zz} P_T^z)]}{\left(\frac{d\sigma_0}{d\Omega}\right)_{lab} [(1 + P_B^z A_{zz} P_T^z) + (1 - P_B^z A_{zz} P_T^z)]} \quad (3.31)$$

$$= P_B^z A_{zz} P_T^z \quad (3.32)$$

$$= \frac{-7}{9} P_B^z P_T^z. \quad (3.33)$$

Using $P_B^z = 0.8$ and $P_T^z = 0.08$, a typical value of the asymmetry for this experiment is roughly -0.05.

3.8.2 Physical Layout

The Møller polarimeter consisted of a movable target ladder with six metal foils, a collimator ‘mask’ which defined the Møller spectrometer acceptance, a dipole magnet to momentum analyze the scattered electrons, and a silicon pad detector package. The targets were placed as far upstream as possible, because the 90° center-of-mass scattering angle was Lorentz contracted to a very tiny lab angle. As shown in Fig. 3.10, the mask was placed upstream from the dipole magnet, B203, so the scattered electrons would experience the magnetic field, but the unscattered beam electrons could travel through a septum made of high permeability μ -metal, shielding them from this field. Shielding the beam electrons was an important requirement for two reasons. First, it kept the beam electrons out of the Møller detector, and second, from a safety viewpoint, it ensured that the beam electrons continued traveling through the beam pipe to the water-cooled beam dump. The beam at full current contained about 100 kW of power, making it essential that the beam not be deflected away from the beam dump.

The optics of the Møller system is shown in Figs. 3.10 and 3.11. The last quadrupole in the A-line, Q41 (not shown in Figs. 3.10 or 3.11), was turned off since

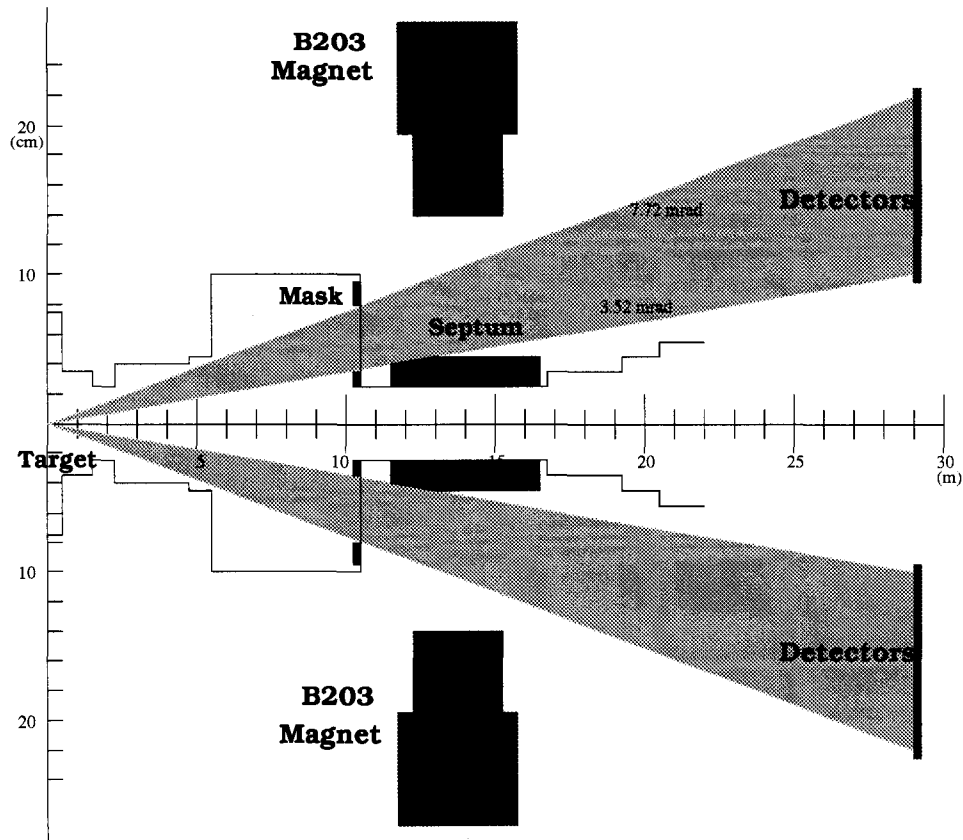


Figure 3.10. The Møller system viewed from the side. The vertical dimension is shown scaled by a factor of 200 larger than the horizontal dimension for clarity. The gray bands show the scattering angle acceptances for Møller electrons in the laboratory reference frame.

it was positioned between the Møller target and the B203 dipole (see Fig. 3.4). This resulted in a very simple spectrometer system consisting of the single dipole, B203. The mask selected electrons scattered in the vertical direction between 75° and 118° in the center-of-mass frame. Unscattered beam electrons continued through a hole in the middle of the mask and through the center hole of the μ -metal septum shielding them from the B203 field. The scattered Møller electrons travelled above and below the septum, allowing them to be deflected by B203 towards the Møller detectors on the north side of the beam line. The Møller electrons traveled the additional drift distance to the detectors through helium-filled boxes to minimize multiple scattering. A detailed magnetic field map of the Møller magnet (B203)

was produced with the septum in place [64], so the Møller spectrometer system could be modeled accurately.

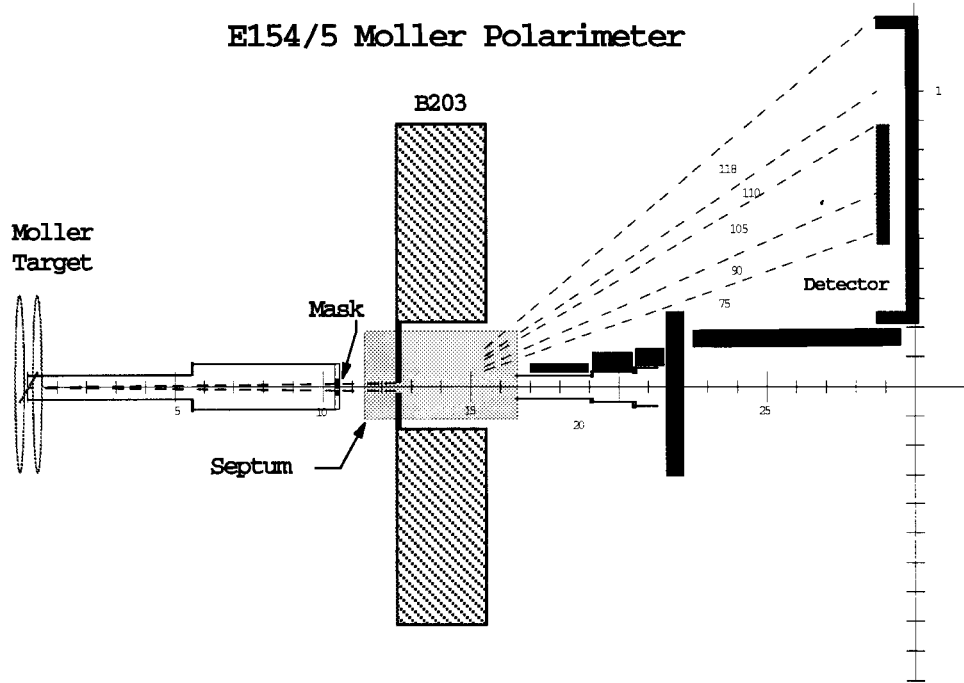


Figure 3.11. The Møller system viewed from above. The vertical dimension is expanded by a factor of ten compared to the horizontal dimension. The scattering angle values shown are for the center-of-mass reference frame.

3.8.3 Møller Target

The Møller target system was originally constructed for the first polarized DIS experiment, SLAC E80, in 1976 [5]. It was refurbished for SLAC experiment E143 in 1994 with new foils, pickup coils, and a stepping motor for positioning the foils in the beam.

The target foils were $3 \text{ cm} \times 35 \text{ cm}$ and consisted of various thicknesses of Vacoflux [65], an alloy of 49% Co, 49% Fe, and 2% V by weight. The six different foils used are summarized in Table 3.3. Each foil was stretched over a frame mounted at 20.7° with respect to the beam axis. The foils were magnetized to near saturation by Helmholtz coils providing nearly 100 Gauss at the target center. Pickup coils,

made from 500 turns of 30 gauge wire, for measuring the foil magnetizations were placed near the foils.

Table 3.3. Møller target foil parameters

Position	Foil	Polarization
1	L4 (154 μm)	0.08283
2	H12 (30 μm)	0.08192
3	K4 (40 μm)	0.08204
4	G17 (20 μm)	0.08116
5	G14 (20 μm)	0.08109
6	K14 (40 μm)	0.08223

The foils were placed at an angle to the beam because the ferromagnetic metal of the target foils channeled the magnetic field lines from the Helmholtz coils into the plane of the target. Ideally, the target electrons would have been polarized along the beam axis, but this would have required the target foil to be edge on to the beam, which was not acceptable. The angle of 20.7° between the beam axis and target foil surface was chosen as a compromise to minimize the target thickness relative to the beam, and still retain a significant polarization parallel to the beam.

The foil polarization was determined using [63]

$$P_T = \left(\frac{M}{n_e \mu_B} \right) \left(\frac{g' - 1}{g'} \right) \left(\frac{g_e}{g_e - 1} \right), \quad (3.34)$$

where M is the bulk magnetization in the foil, n_e is the electron number density, $\mu_B = 9.273 \times 10^{-21} \text{ G}\cdot\text{cm}^3$ is the Bohr magneton, g' is the magnetomechanical ratio, and $g_e = 2.002319$ is the free electron g factor. The g' factor is needed to make a correction for orbital contributions to the magnetization.

Two methods are available to determine g' . The g' values for Fe and Co can be determined individually and interpolated using a weighted average to find g'_{eff} for an alloy of the two. The 2% vanadium is neglected in this instance since it is

paramagnetic rather than ferromagnetic. The weighted average used is

$$g'_{eff} = \frac{M_1 + M_2}{(M_1/g'_1) + (M_2/g'_2)}, \quad (3.35)$$

where M_i are the saturation magnetizations of each species, and g'_i are the corresponding magnetomechanical ratios. At 20° C, $M_{Fe} = 218.0$ and $M_{Co} = 161$ [66]. Taking g'_{Fe} and g'_{Co} from [67], g'_{eff} is found to be [68]

$$g'_{eff} = 1.889 \pm 0.005. \quad (3.36)$$

This was the method used by previous experiments in End Station A.

The second method for determining g'_{eff} of Vacoflux is to use a direct measurement by Scott and Sturner [69] of $g'_{eff} = 1.916 \pm 0.002$ for a foil with equal amounts by weight of iron and cobalt. For the purposes of E154 the 2% of vanadium is again assumed to be negligible, and Scott and Sturner's value for g'_{eff} may be used without modification.

Because the values of g'_{eff} determined by these two methods do not agree, and because it is assumed that the vanadium does not affect the g'_{eff} value, the larger overall systematic uncertainty to g'_{eff} of 0.005 was accepted. The final value used in the Møller analysis was $g'_{eff} = 1.916 \pm 0.005$ [63].

3.8.4 Møller Detector

The Møller detector consisted of a series of five silicon panels arranged as shown in Fig. 3.12. Each panel consisted of two 4 cm wide by 6 cm tall pads mounted vertically one above the other, making an overall pad 4 cm wide by about 12 cm tall. Each of these pads was 300 μm thick. The four lower detectors each had 12 channels with a vertical segmentation of 8.69 mm. The upper detector had 48 channels with a vertical segmentation of 2.18 mm. There was a 7 mm gap between the two pads which fell between channels 24 and 25 on the top detector and channels 5 and 6 on

the bottom set. The upper detector was movable to cover the full kinematic range of the Møller spectrometer. The detectors were tilted $+12.5^\circ$ (top) and -10.2° (bottom) to align them with the Møller scattering stripes.

The 96 silicon channels were connected to 96 charge-sensitive preamplifiers. The outputs from the preamplifiers were transmitted into the End Station A counting house on long coaxial cables and input into charge-sensitive analog to digital converters (ADCs) in the beam CAMAC crate. Linearity calibrations of the ADCs were made before and after the experiment. Nonlinearities were less than 0.5% overall, and typically less than 0.1% for most channels.

3.8.5 Møller Data and Analysis

Measurements from the 96 ADC channels corresponding to counting rates (pulse heights) in the silicon strip detectors were the Møller data for each spill. The Møller asymmetry, defined in Eq. (3.31), consisted of the difference between the count rates for opposite beam helicities divided by the corresponding sum of count rates. Typical data for the sum and difference are shown in Figs. 3.13 and 3.14.

The raw pulse height data and the counting errors were averaged for each channel. Separate averages were maintained for each beam helicity. Rough beam cuts were required, limiting the beam current to an acceptable minimum. The beam cut rejected roughly 2.5% of the spills from the data set. These averages and errors for each channel and each beam helicity were written to a data summary file for each run.

As shown in Fig. 3.13, there was a background under the Møller peak. This was estimated by fitting the unpolarized peak with a quadratic background term. This same technique was used previously in both E142 and E143.

Detector Hut

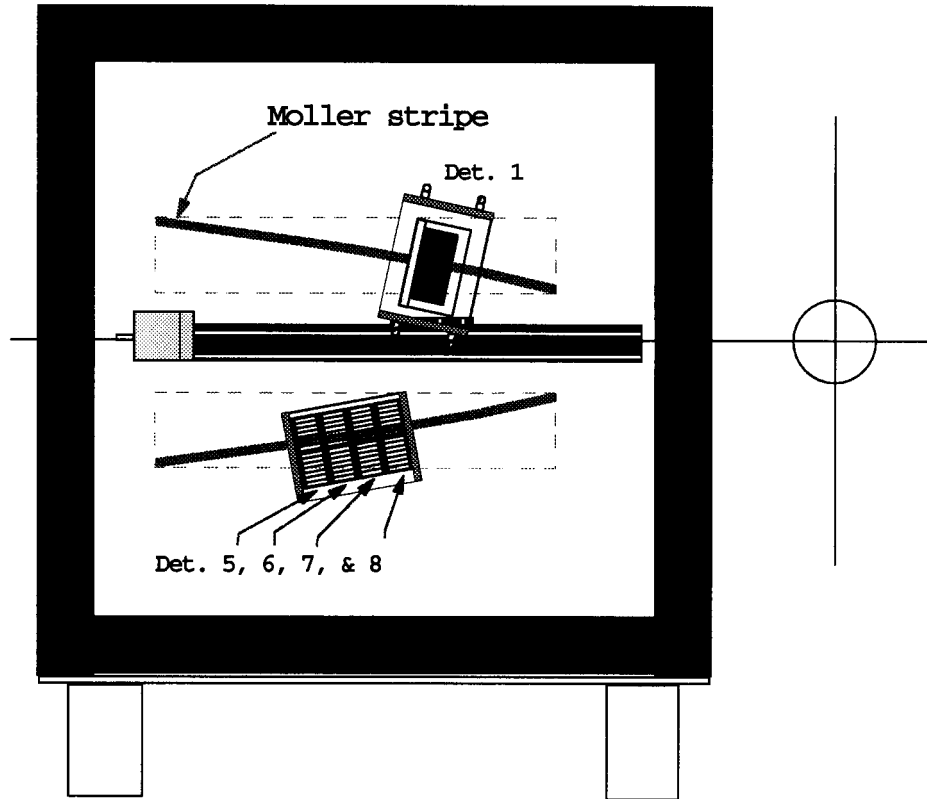


Figure 3.12. The Møller Detector Package. The main beam line is shown as the circle on the right. The gray band labeled 'Møller stripe' in the figure is the region where elastically scattered Møller electrons are expected after being deflected to the left by the Møller magnet. There is a symmetrically placed stripe below the beam axis for scattering 'down' rather than 'up'. The upper and lower detectors are clearly visible, including the actuator for moving the upper silicon pad detector array horizontally.

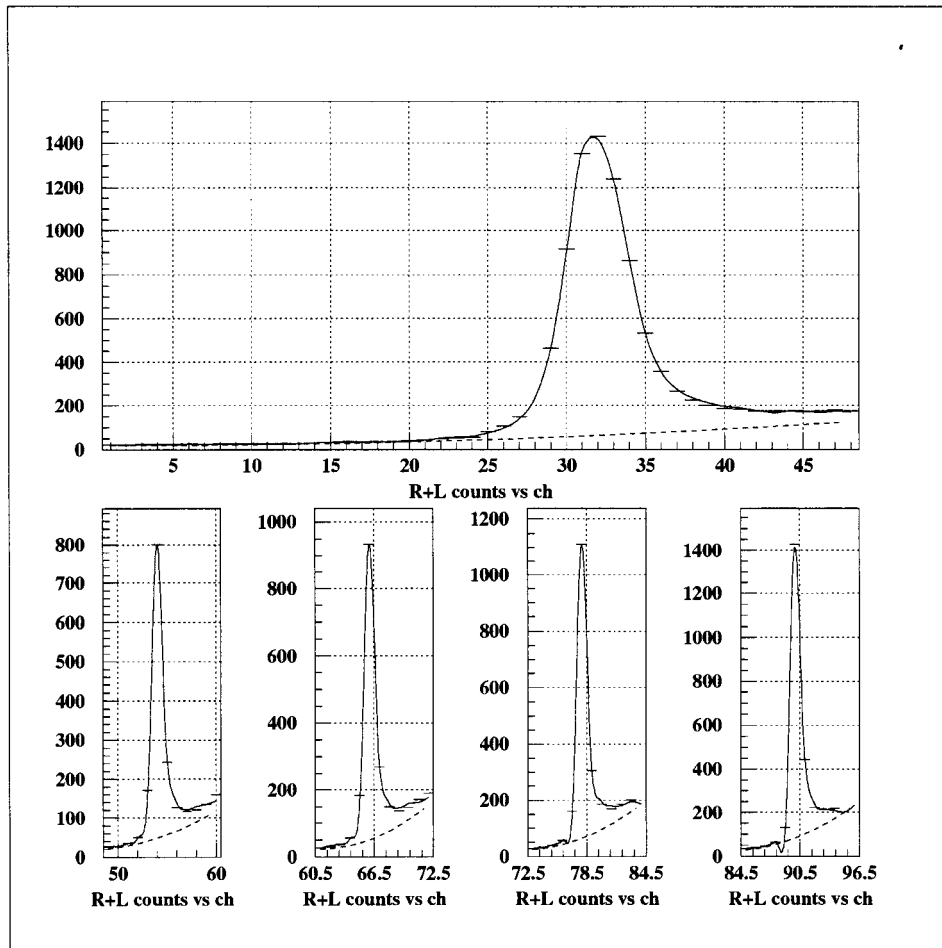


Figure 3.13. Møller data showing the sum of right and left helicities for run number 3349. The top figure corresponds to the upper Møller detector, and the four lower figures show data from the four lower detectors. In each instance, larger scattering angles are to the left.

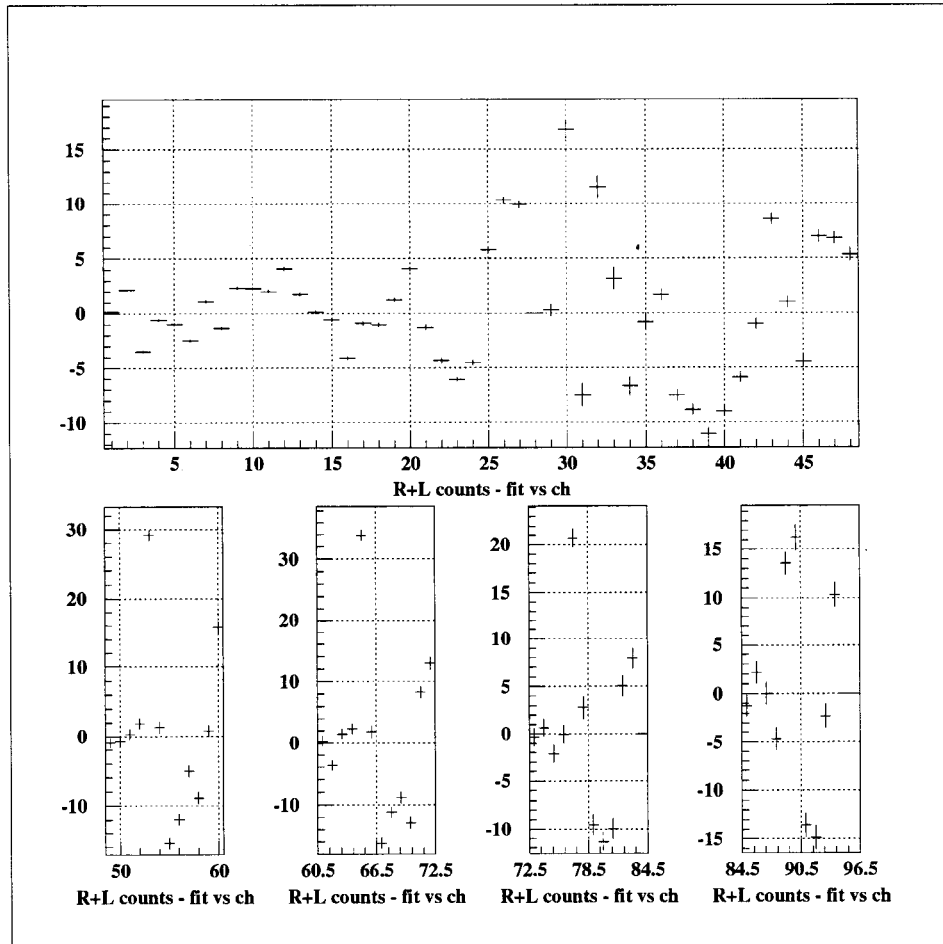


Figure 3.14. Møller data showing the difference between right and left beam helicity count rates for run number 3349.

The measured Møller asymmetry was determined using

$$A_{Moller} = \frac{\sum_i (R_i - L_i)}{(R_i + L_i) - B_i}, \quad (3.37)$$

where R_i and L_i were the count rates for incident beam helicities right and left respectively, and B_i was the background term for the i^{th} channel determined by the quadratic fits. This asymmetry was compared with Eq. (3.33) allowing the beam polarization to be determined.

3.8.5.1 Averaging Runs

As in the main experiment, many runs were typically averaged together to minimize the statistical and systematic uncertainties. The formula for combining many measurements of an asymmetry with statistical uncertainties only is

$$\bar{A} = \frac{\sum (A_i/\sigma_i^2)}{\sum (1/\sigma_i^2)} \pm \sqrt{\frac{1}{\sum (1/\sigma_i^2)}}, \quad (3.38)$$

where A_i is the measured asymmetry for each individual run, and σ_i is the corresponding uncertainty.

3.8.6 Sign of the Beam Polarization

The Møller asymmetry of Eq. (3.33) is negative, so the cross section is larger if the beam and target electron spins are anti-parallel. The Møller target polarization sign was determined by explicitly measuring the Helmholtz field with a Hall probe. It was found to point downstream when the power supply voltage was positive. The magnetization is in the same direction as the driving H-field; however, the electron magnetic moments are in the opposite direction to the electron spin. Thus, the Møller target electron spins pointed upstream when the Helmholtz power supply voltage was positive. With this information the polarization direction of the beam electrons could be determined unambiguously, and compared to the polarization bits from the polarized source. It was found that pulses labeled as ‘R’ at the source,

corresponding to a value of ‘1’ in the polarization bits, were left-handed helicity electrons in ESA. This was consistent with 15π spin precessions. Similarly, electrons labeled as ‘L’ at the source, corresponding to a value of ‘2’ in the polarization bits, were right-handed helicity electrons in ESA [63].

3.8.7 Energy Scan

As mentioned earlier, a beam energy scan was performed to determine the beam energy at which the polarization peaked in the End Station due to the electron spin precessions. This program was carried out on October 11, 1995 in runs 1414 through 1455. Using the formulae for the spin precession and synchrotron energy losses derived in section 3.4.2, a formula relating the beam polarization in the End Station to the beam energy may be derived which states

$$P_{ESA} = P_0 \cos \left\{ \pi \left[E + \Delta + \frac{0.198(E/48.362)^4}{3.2374} \right] \right\}, \quad (3.39)$$

where P_0 corresponds to the polarization at the source, E the beam energy, and Δ accounts for uncertainties in the energy measurements. The results of the energy scan with a fit of the form of Eq. (3.39) are shown in Fig. 3.15. The best fit to the data resulted in the constants $P_0 = 79.1 \pm 0.3$, and $\Delta = 0.074 \pm 0.003$. After this scan the beam energy was set to 48.30 GeV for the rest of the experiment.

3.8.8 Source Laser Wavelength Scan

The polarization of the electrons produced at the polarized source, which was described in section 3.2, had a slight dependence on the wavelength of the circularly polarized laser light. Two separate scans were carried out [63] to find an optimal laser wavelength. The scans showed an improvement at longer wavelengths, so the source laser wavelength was increased from 845 nm to 850 nm.

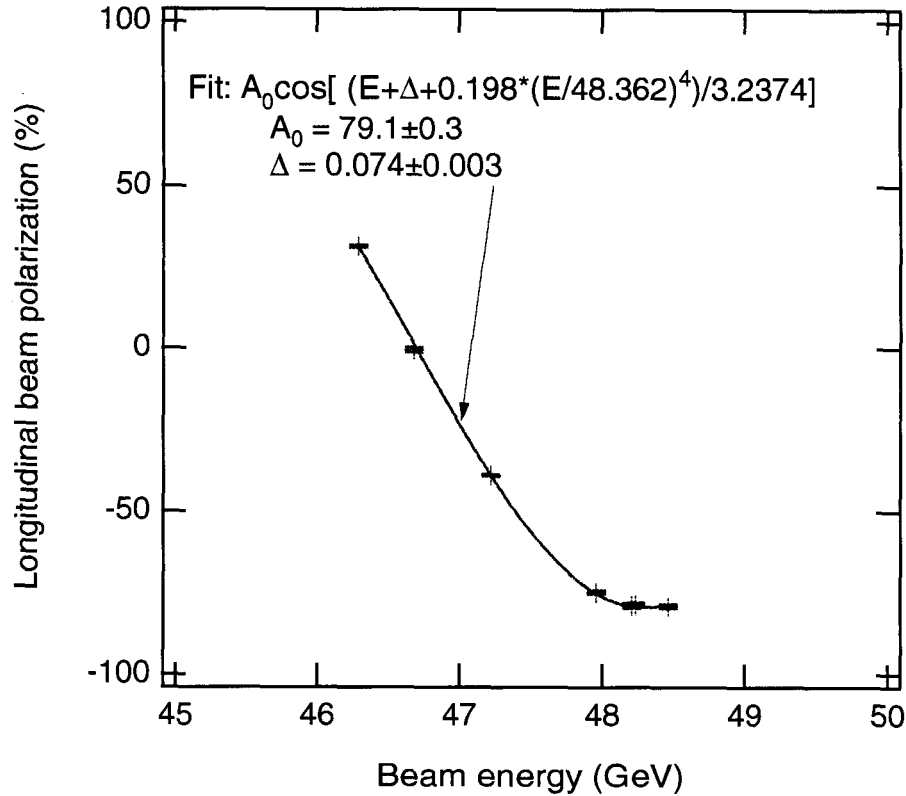


Figure 3.15. Beam polarization vs. beam energy in ESA. The parameters of the fit are described in the text.

3.8.9 Møller Results and Uncertainties

As in the main experiment, the beam polarization was varied in a pseudo-random manner during Møller runs. In fact, from the point of view of accelerator operation, only the final two quadrupoles in the A-line were operated at different field strengths compared with the main experiment. The frequent and random switching of the polarization, due to the pseudo-random algorithm described in section 3.2, minimized any systematic effects due to either a specific polarization combination, or 60 Hz related effects. Additionally, the Møller target foil polarizations were altered, typically between runs to alleviate any other systematic asymmetries.

The individual uncertainties contributing to the overall uncertainty of the beam polarization measurement are listed in Table 3.4. The determination of each uncertainty is described in [63].

Table 3.4. Uncertainties contributing to the Møller measurement of the beam polarization.

Item	Systematic Error
Foil Magnetization	1.7%
Kinematic Acceptance	0.3%
Background Correction	2.0%
Fit Range	0.3%

As mentioned earlier, the beam polarization was very constant for the later part of the E154 running period. This is demonstrated in Fig. 3.16. The different straight lines are averages of Møller measurements made with similar beam characteristics. The relevant run ranges and the corresponding average polarizations are listed in Table 3.5 with statistical uncertainties only. The changes between ranges of run numbers in Table 3.5 are as follows: runs 1329-1411 were before the beam energy optimization and source laser wavelength adjustment; runs 1456-1684 came after the optimizations; runs 1691-2311 followed more source optimizations; runs 2316-3371 were for average beam currents of 4.9×10^{10} electrons per pulse; and runs 3377-3788 were for beam currents of 3.0×10^{10} electrons per pulse.

Table 3.5. Run ranges during which the beam and source characteristics were reasonably stable. The average polarization from the Møller measurements taken in each range are shown with statistical uncertainties only.

Run Range	Average Polarization
1329-1411	0.759 ± 0.004
1456-1684	0.775 ± 0.005
1691-2311	0.814 ± 0.002
2316-3371	0.824 ± 0.001
3377-3788	0.826 ± 0.002

After appropriately combining the uncertainties, an average beam polarization was determined for the later runs (1691-3788) which encompassed nearly all of the useful E154 asymmetry data. The final value was 0.82 ± 0.02 .

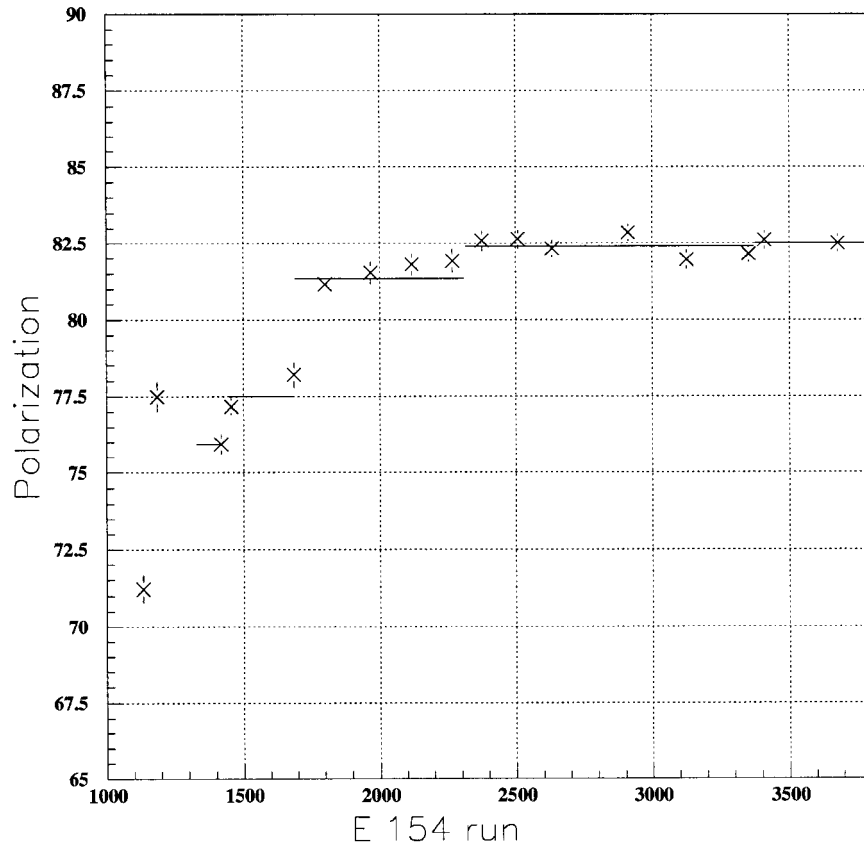


Figure 3.16. Beam polarization in percent vs. run number. The straight horizontal lines show averages for run ranges over which the beam characteristics were similar.

CHAPTER 4

THE E154 EXPERIMENT

The E154 experiment was designed to measure the neutron g_1 and g_2 structure functions using the upgraded SLAC A-line electron beam energy of 50 GeV described in chapter 3. Polarized ^3He provided the neutron target, and two independent spectrometers, set at laboratory scattering angles of 2.75° and 5.5° , measured deep-inelastically scattered electrons. Most of these systems were modifications of the previously used E142 and E143 systems, adjusted for the higher beam energy.

4.1 The E154 Polarized Target

The E154 polarized target system consisted of two glass cells containing ^3He , rubidium, and a small amount of nitrogen. These two cells were connected by a small glass tube allowing the ^3He , which became polarized in the upper ‘pumping’ cell, to diffuse to the lower ‘target’ cell. The pumping cell was positioned within an oven which heated the cell to over 150°C to vaporize the rubidium. Gaseous rubidium atoms were polarized using circularly polarized laser light from an array of high power lasers. The polarized rubidium atoms in turn polarized the ^3He nuclei in the pumping cell through spin exchange interactions. A small holding field of a few Gauss, provided by a large Helmholtz coil, kept the spins of the polarized atoms aligned. A schematic of the full system is shown in Fig. 4.1.

Rubidium was concentrated in the upper cell by cooling the lower target cell to the point where the rubidium vapor pressure was negligible. This was accomplished

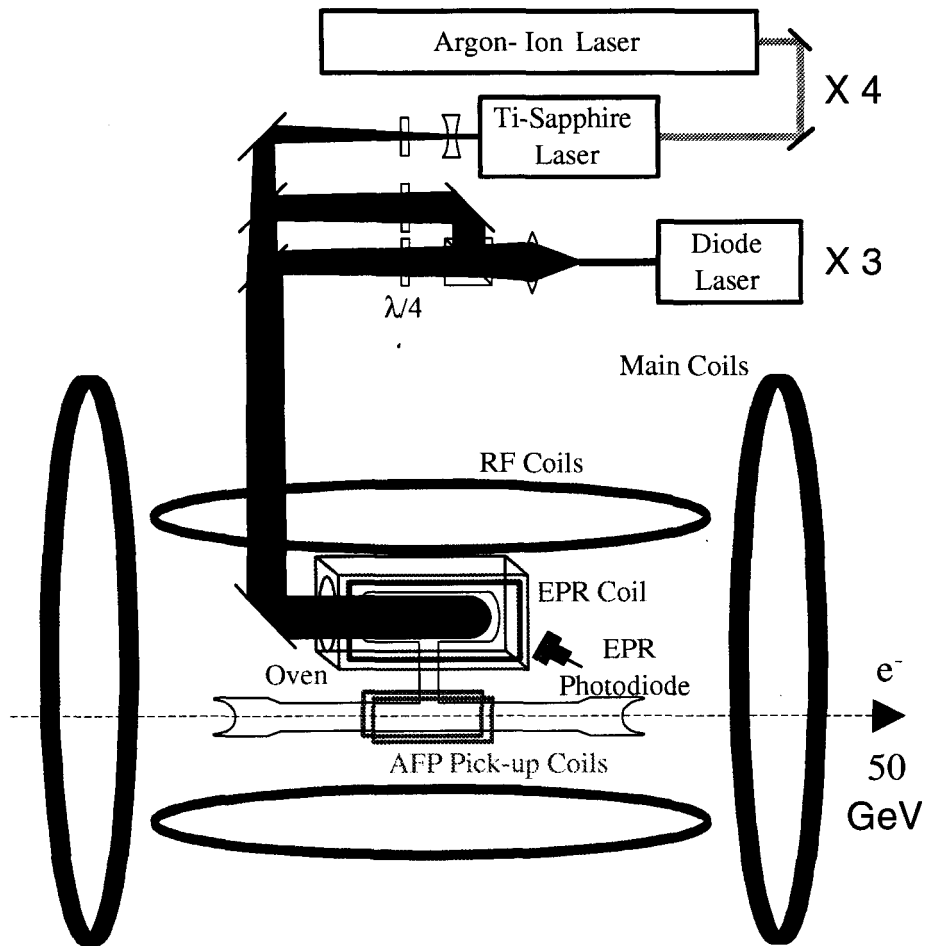


Figure 4.1. The E154 polarized ^3He target system.

by directing small ^4He cooling jets onto the end windows of the lower cell, which maintained it close to room temperature.

In order to achieve a reasonable target thickness with a gas, a high pressure glass cell like the one drawn in Fig. 4.2 was used. The cells were blown at Princeton University from 1720 Corning glass tubes. The thin inverted end windows permitted high pressures of about 10 atmospheres. The flares at the ends of the target cell allowed the thin end windows to be ‘welded’ into place, and the connection between the windows and the tube to be made as rounded as possible. Avoiding sharp corners reduced local stresses in the glass under pressure, which in turn allowed higher pressures to be used. Because these cells were blown by hand, every cell had

slightly different dimensions as shown in Table 4.1. Table 4.2 lists the range of run numbers during which each target cell was in use.

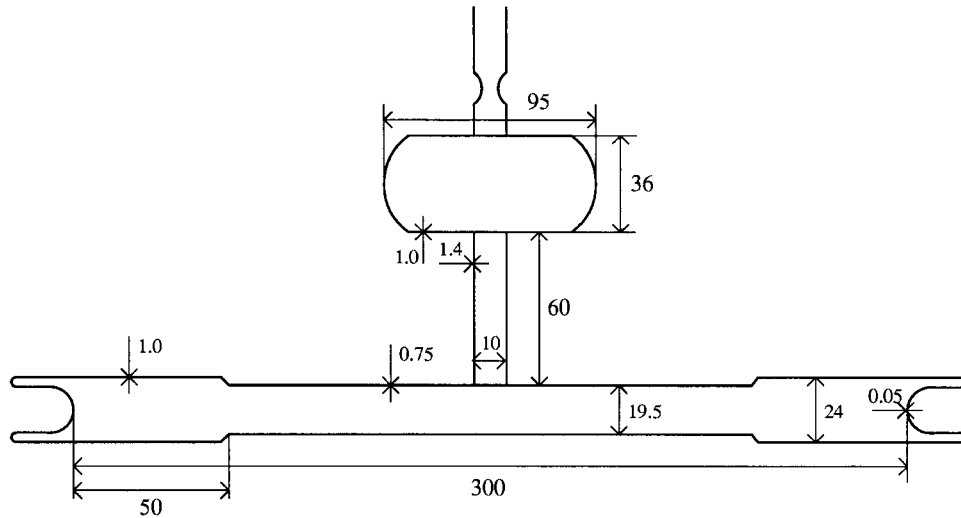


Figure 4.2. A polarized ^3He target cell (Picard). All dimensions are in mm. Other cells were very similar in size and shape. Relevant dimensions for all cells used are listed in Table 4.1.

4.1.1 Polarizing ^3He

The ^3He in the target cell was polarized through spin-spin interactions with rubidium atoms, which in turn were polarized by circularly polarized laser light. This light was generated by a set of three diode lasers and by an array of four Ti:sapphire lasers each pumped by an Argon ion laser. The Ti:sapphire lasers had a very narrow bandwidth centered on the rubidium D1 transition line, but were expensive and somewhat unreliable. By contrast, the diode lasers had a much broader bandwidth, resulting in only a fraction of the total power being useful, but were easily obtained and much cheaper. Since one of the limiting factors in achieving high polarization was the available laser power, a combination of both types of lasers was used.

Rubidium atoms were polarized through the use of optical pumping and the application of a magnetic field [70]. Initially the rubidium was unpolarized with

Table 4.1. Target cell dimensions in mm. ‘OD’ refers to the outer diameter, ‘Wall’ is the wall thickness of the main target cell tube, the ‘Start’ column under ‘Flare’ measures the distance from the center of the cell to the start of the flare, and the two lengths under ‘Pumping Cell’, ‘L.1’ and ‘L.2’, refer to the length of the straight part of the pumping cell wall, and the total length, respectively.

Cell Name	Target Cell				Flare		Transfer Tube		Pumping Cell		
	OD	σ_{OD}	Wall	Length	Start	OD	OD	Length	OD	L. 1	L. 2
Dave	20.75	0.02	0.730	291	110	26.7	12.4	61.5	36.3	84.0	95.1
Riker	21.72	?	0.697	300	105	25.7	11.8	?	37.2	70.6	82.3
Bob	20.80	0.03	0.728	299	115	26.6	12.3	61.2	36.1	79.0	94.6
SMC	20.66	0.05	0.733	302	110	26.3	12.2	63.5	37.8	77.7	90.7
Generals	21.62	0.13	0.700	297	110	25.9	12.9	59.2	36.0	66.8	80.0
Hermes	20.53	0.03	0.737	295	110	26.7	11.9	62.9	37.7	74.8	89.4
Prelims	21.24	0.04	0.713	300	110	26.0	12.9	59.4	36.1	68.3	80.5
Chance	21.33	0.05	0.710	299	118	25.4	13.5	67.0	35.8	79.0	93.0
Picard	22.40	0.09	0.676	299	105	25.3	11.5	61.6	37.7	65.5	79.8
Water I	20.55	0.03	0.737	302	102	24.8	14.0	59.7	36.8	74.9	88.9
Water II	22.62	0.07	0.669	297	112	25.4	13.2	72.6	36.8	73.7	94.5

an equal number of valence electrons in the $5S_{1/2}$ ($M_J = -1/2$) and the $5S_{1/2}$ ($M_J = +1/2$) states. Optical pumping transferred electrons preferentially to the $5S_{1/2}$ ($M_J = +1/2$) state allowing an external magnetic field to align the spins and polarize the bulk rubidium. The relevant energy levels for rubidium are displayed in Fig. 4.3.

The D1 line of rubidium, at 794.7 nm excited the valence electron from the $5S_{1/2}$ ($M_J = -1/2$) ground state to the $5P_{1/2}$ ($M_J = +1/2$) state. This is shown schematically in Fig. 4.3 by a diagonal line between the states. In the excited P state, the electron spin was ‘up’. This state radiatively decayed to both magnetic states with the $5S_{1/2}$ ($M_J = -1/2$) state favored two to one over the $5S_{1/2}$ ($M_J = +1/2$) state. However, some of the electrons ended up in the spin up ($M_J = +1/2$) state. Electrons which decayed back to the spin down state simply need to be optically pumped again, and slowly the $5S_{1/2}$ ($M_J = +1/2$) state became filled.

Table 4.2. Target cell usage during E154. The upper entries are for the polarized ^3He cells, and the lower four entries list the corresponding reference cells.

Cell Name	First Run	Last Run
Dave	1201	1388
Riker	1412	1757
Bob	1777	2043
SMC	2050	2311
Generals	2316	2594
Hermes (Mercury)	2597	2902
Prelims	2903	3100
Chance	3101	3371
Picard	3377	3788
Ref. Cell #1	733	1757
Ref. Cell #2	1777	2047
Ref. Cell #3	2050	2596
Ref. Cell #4	2597	3788

This picture was complicated by the fact that the $5P_{1/2}$ state radiated unpolarized photons as it decayed to the $5S_{1/2}$ state. These decay photons could depolarize the bulk rubidium as they scattered off of other rubidium atoms. This process would have left only a tiny fraction of the rubidium near the laser entry window polarized, without the addition of a small amount (100 torr) of nitrogen as a ‘buffer’ gas. The buffer gas ensured that the $5P_{1/2}$ state was non-radiatively quenched by collisional interactions with the nitrogen gas since the collision cross section is much larger than the decay cross section.

The ^3He atoms in the target cell interacted with the polarized rubidium through a hyperfine spin-exchange, which transferred the polarization from the rubidium to the ^3He . The interacting rubidium atoms became unpolarized in the process, but could be optically pumped again quickly, since the optical pumping cross section is much larger than the hyperfine spin-exchange cross section. For this reason, the inverse spin-exchange interaction where a ^3He atom transfers its spin back to a rubidium atom was inhibited since the rubidium atoms were all already in the polarized state.

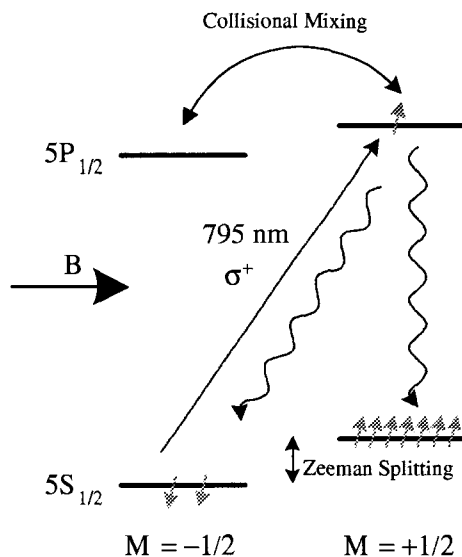


Figure 4.3. Rubidium energy levels.

A number of methods existed by which the polarized ^3He atoms could become depolarized. First, they could interact with unpolarized rubidium as described above. Second, they could experience a spin-exchange interaction with the unpolarized glass of the target cell walls. Third, they could be ionized by the high energy electron beam and lose their polarization. And fourth, the oscillating magnetic field used for measuring the polarization with the Adiabatic Fast Passage method (AFP) described below, could push the spins out of alignment with the holding field, causing a loss of polarization.

Since the spin-exchange cross section was so small, it was imperative that these depolarizing mechanisms were minimized in order to retain an appreciable ^3He polarization. The effect of the unpolarized glass walls was minimized by the choice of 1720 Corning glass since this type of glass is very impermeable to ^3He . This meant that the ^3He atoms did not spend an appreciable duration of time in close contact with the cell walls, and consequently very few spin-exchange interactions could take place. Very little could be done about the ionization caused by the beam, but fortunately this was a relatively small effect. The loss of polarization

due to the AFP measurements was minimized by spacing the measurements fairly far apart in time.

As an example of the time scales being discussed, the ‘spin-up’ of the target cell named ‘Picard’ is shown in Fig. 4.4. It took between 70 and 80 hours to reach its asymptotic polarization value of about 48% ^3He polarization. One can also see that the depolarization effect due to the beam was quite small since the polarization continued to follow nearly the same curve after the beam was turned on at about 35 hours.

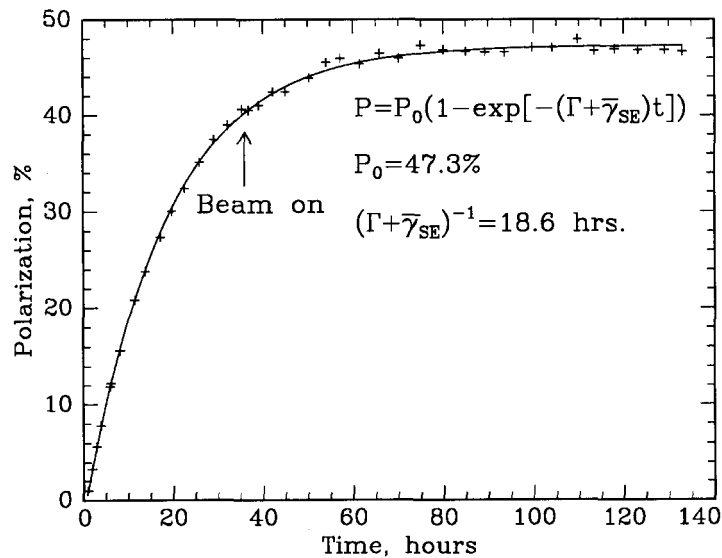


Figure 4.4. ‘Spin-up’ of target cell ‘Picard’.

4.1.2 Measuring the ^3He Polarization

The target polarization was one of the multiplicative factors relating the measured asymmetry to the parallel and transverse asymmetries being measured (see Eqs. (2.101) and (2.102)). For this reason it was measured frequently during the experiment using one of two methods. The primary method used was Adiabatic Fast Passage (AFP) which measured the nuclear magnetic resonance (NMR) signal

of the ^3He nuclei. The second method used was Electron Paramagnetic Resonance (EPR). The EPR method was only used on a few occasions, and was effectively a cross check on the AFP system.

The AFP method worked as follows. The ^3He nuclear spins were aligned along the beam direction (the \hat{z} axis) by a relatively large 5-20 gauss holding field produced by the main Helmholtz coils. An additional oscillating magnetic field in the \hat{x} direction could be thought of as the superposition of two circularly rotating magnetic fields turning in opposite directions. As the ^3He nuclear spins attempted to follow the driving field, they precessed around the primary field direction. One of the two rotating fields rotated in the same direction as this precession. At 92 kHz the spin precession was in resonance, and the spins were driven to the point where they completely flipped over and pointed in the opposite direction. It was important to drive them through the resonance quickly ('Fast Passage') since at the resonance the spins were being violently tossed about and the polarization could easily be completely lost. The precessing spins generated a small additional oscillating magnetic field which was detected in a pair of pickup coils mounted perpendicular to the \hat{y} direction as an NMR signal. This NMR signal was proportional to the ^3He polarization. The process was 'adiabatic' since the 92 kHz driving field was slow enough that the spins could follow it, yet simultaneously 'fast passage' through the resonance so the polarization would not be destroyed during the process.

AFP was used throughout the experiment to measure the target polarization every few hours. The process typically reduced the target polarization by about 1/2%, so it was important not to use it too frequently. Additionally, the beam had to be turned off, and data acquisition halted, which stopped the experiment. Because of this, a compromise of two to four hour intervals between measurements was typical throughout the two-month duration of the experiment.

The Electron Paramagnetic Resonance (EPR) method measured the Zeeman splitting of ^3He resonance lines due to the additional magnetic field caused by the polarized ^3He nuclei. The Zeeman splitting could be measured quite accurately, and the contribution due to the ^3He spins could be determined by reversing the ^3He spin directions relative to the holding field and comparing the two measurements.

Both the AFP and EPR methods measured the polarization with approximately 4% relative uncertainty [71]. Since the agreement between the two methods was quite good, the results were averaged, with an overall error of 4.8%. The overall error does not reduce in the averaging process because the difference between the measurement techniques is assumed to be due to systematic shifts in one or both methods.

4.1.2.1 Problems Achieving High Polarization

Some target cells experienced difficulty achieving high polarization. Several parameters were varied in an attempt to improve the situation, but in several cases without success. After careful testing, several possible problems were identified and mostly rectified.

One of these problems involved masing in the ^3He cell. The AFP pickup coils acted as mirrors to an RF signal, which could 'mase' in the cell at the 92 kHz AFP frequency. This process could depolarize the ^3He atoms since the nuclear spins would be driven by the resonating RF signal to precess around the alignment direction. Since this was at the AFP resonance, the precessing spins could be violently tossed around, causing the polarization to be lost. No immediate cure was found for this problem, but as it only appeared to manifest itself in certain cells, it was not pursued any further.

4.1.3 Polarization History

The ^3He target polarization as a function of run number is plotted in Fig. 4.5. Each of the different target spin-ups is visible. It is possible to see where the target polarizations were reversed, that the average polarization was around 38%, and that the maximum polarization achieved was slightly less than 50% for the last target cell, named 'Picard'.

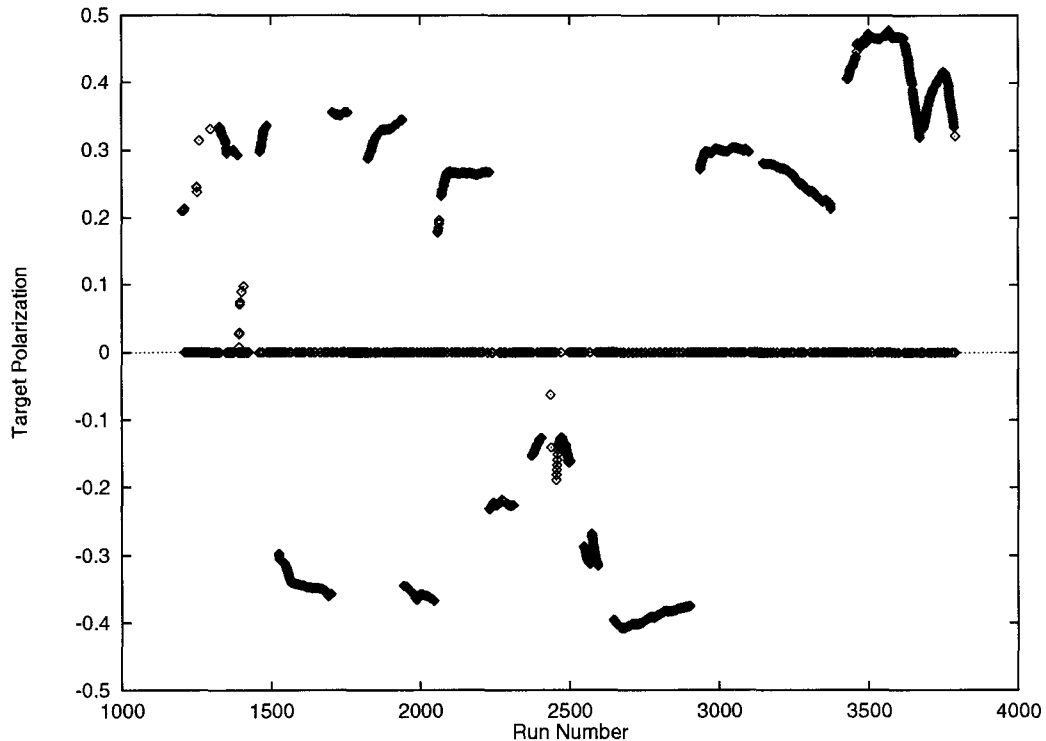


Figure 4.5. Target polarizations as a function of run number. As can be seen, the majority of runs had positive polarizations corresponding to the ^3He magnetic moment pointing downstream in the beam line. Most of the 'spin-ups' are not very obvious, because no data runs were taken on the polarized target cells until the polarization reached a reasonable value.

4.1.4 The Exploding Target Problem

During the 'owl' shift on October 11, at about 2:15 AM, the SEM monitor near the target caused the beam to shut off. When the beam was restored it was noticed that the good spill monitor was not showing an appreciable signal. After some

investigation it was determined that the target had in fact exploded. A lengthy investigation followed in an attempt to determine a cause for the demise of this target cell, and several possible explanations were explored. First, changes in the beam characteristics, such as increased emittance, a large increase in current, or the beam being steered onto the target wall were investigated. Second, since the vacuum monitors went off at the same time as the beam shut down, the possibility that a sudden vacuum leak in the ESA beam line might have caused the target to explode was explored. However, under close scrutiny, none of these possibilities appeared to be the cause of the explosion.

A second cell, named 'Riker', was installed, and running resumed October 12. This cell lasted until October 17, when it too exploded. At this point it was conjectured that the glass end windows of the cells were being radiation-damaged by the beam, and collapsing under the 10 atm pressure. Another conjecture was that the beam was heating the glass end windows beyond their tolerance: with a very tightly focused beam, a small spot on the end window could become quite hot and possibly weaken the glass. The radiation-damage and local heating effects were minimized by spreading the beam spot size out to cover a larger surface area on the target cell end window. The beam current was also lowered from 9×10^{10} to 5×10^{10} electrons per spill. After several more target ruptures, it was lowered even further to the final value of 3×10^{10} electrons per spill. Whether or not these adjustments were the reason, the last target cell used, 'Picard', survived intact longer than any of the previous cells, lasting through to the end of the experiment, and fortunately also producing the highest polarization of all the target cells.

4.2 The Dilution Factor

The neutron spin structure functions were measured by scattering electrons off ^3He nuclei. However, electrons were also scattered by the unpolarized nitrogen gas contained in the target cell, and by the unpolarized glass end windows of the target cell, which effectively diluted the measured DIS electron asymmetry for scattering off polarized ^3He . Fortunately, this effect could be appropriately accounted for, and the true ^3He asymmetry determined from the data.

The measured cross section was the sum of all cross sections of all target materials visible from the spectrometer acceptance. In particular, the number of electrons scattered into the spectrometer acceptance was

$$n_{meas} = n_{^3\text{He}} + n_{N_2} + n_{glass}, \quad (4.1)$$

where n refers to the number of electrons scattered into the spectrometer acceptance from each of the listed target components. The ^3He dilution factor $f_{^3\text{He}}$ was defined as the ratio of the number of detected electrons scattered off ^3He to the total number of detected electrons:

$$f_{^3\text{He}} \equiv \frac{n_{^3\text{He}}}{n_{^3\text{He}} + n_{N_2} + n_{glass}} = \frac{n_{^3\text{He}}}{n_{meas}}. \quad (4.2)$$

Since cross sections are functions of x and Q^2 , the dilution factor is also a function of these variables. This necessitated calculating a dilution factor for each individual x bin, for each of the two spectrometers, and for each of the nine target cells used.

4.2.1 Dilution Factor Model

Since unpolarized DIS cross sections have been very well measured in the past, the number of electrons scattered into the spectrometer acceptance in a given x

range can be calculated quite accurately, allowing the dilution factor to be calculated for a model of the target geometry. The relevant counting rates are derived as follows: Define L_i as the thickness of a given target material, and n_i as the number density of scattering centers in this material. The total number of scattering centers in the target material contributing to counts in a spectrometer is then $SL_i n_i$, where S is the cross sectional area of the incident beam. If σ_i is defined to be the scattering cross section for the target material, and $a(x, Q^2)$ as the spectrometer acceptance, then the number of beam electrons scattered into a by the target material is

$$N_i(x, Q^2) = \left(\frac{I}{S}\right) (SL_i n_i) \int_{[x \text{ bin}]} d\Omega(x, Q^2) \sigma_i(x, Q^2) a(x, Q^2), \quad (4.3)$$

where I is the number of incident beam particles and Ω is the solid angle acceptance.

For the kinematics of this experiment the cross section varied slowly within every individual x bin except the lowest, where it changed mildly, allowing a factorization of the cross section $\sigma_i(x, Q^2)$ outside the integral:

$$\int_{[x \text{ bin}]} d\Omega(x, Q^2) \sigma_i(x, Q^2) a(x, Q^2) \approx \sigma_i(\bar{x}, \bar{Q}^2) a(\bar{x}, \bar{Q}^2). \quad (4.4)$$

Here \bar{x} and \bar{Q}^2 denote the average x and Q^2 over the spectrometer solid angle for a given x range.

The cross section for deep inelastic electron scattering off any isotope can be parametrized quite generally using the proton and neutron form factors $F_2^p(x, Q^2)$ and $F_2^n(x, Q^2)$, and the EMC effect parametrizations, which account for nucleon binding effects. The cross section takes the form

$$\sigma_i(x, Q^2) = K(x, Q^2) [Z_i F_2^p(x, Q^2) + (A_i - Z_i) F_2^n(x, Q^2)] E(A_i, x), \quad (4.5)$$

where $K(x, Q^2)$ contains kinematical factors, and $E(A_i, x)$ is the EMC effect parametrization [72].

Equation (4.5) can be used to determine the deep inelastic electron scattering cross sections for each individual target material. With this information, and knowledge of the target thicknesses for each isotope, the dilution factor can be calculated as

$$f(\bar{x}, \bar{Q}^2) = \frac{R_{He}(\bar{x}, \bar{Q}^2)}{R_{He}(\bar{x}, \bar{Q}^2) + R_{N_2}(\bar{x}, \bar{Q}^2) + R_{glass}(\bar{x}, \bar{Q}^2)}, \quad (4.6)$$

where

$$R_i(x, Q^2) \equiv L_i n_i K(x, Q^2) [Z_i F_2^p(x, Q^2) + (A_i - Z_i) F_2^n(x, Q^2)] E(A_i, x). \quad (4.7)$$

4.2.2 Radiative Corrections

Equation (4.6) is true only for the leading order scattering diagram. All other orders are accounted for by radiative corrections. This type of radiative correction is termed internal, since it is related to the internals of the actual nuclear scattering. The other type of radiative correction is termed external, and accounts for radiative effects, primarily bremsstrahlung off other nuclei, which can occur both on the way to the scattering center, and on the way out from the scattering center. Both effects must be convolved as

$$rc_i \equiv rc_i^{int} \otimes rc_i^{ext} \quad (4.8)$$

for the i^{th} target material. There are standard methods for calculating these unpolarized radiative corrections which are described in reference [73].

With the radiative corrections, the dilution factor of Eq. (4.6) must be modified to

$$f = \frac{R_{He}(\bar{x}, \bar{Q}^2) rc_{He}}{R_{He}(\bar{x}, \bar{Q}^2) rc_{He} + R_{N_2}(\bar{x}, \bar{Q}^2) rc_{N_2} + R_{glass}(\bar{x}, \bar{Q}^2) rc_{glass}}. \quad (4.9)$$

Finally, the glass must be divided into two separate contributions, from the upstream window and the downstream window, since the radiative corrections for each are quite different.

4.2.3 Experimental Measurement of the Dilution Factor

In addition to the calculation described above, a direct measurement of the dilution factor was performed for each target cell. The definition, Eq. (4.2) suggests the method: A measurement of the total number of detected electrons both with and without ^3He was made. The number of electrons scattered off ^3He could then be determined, allowing a direct measurement of the dilution factor f . In practice, the polarized target cells were sealed, making it impractical to try emptying and refilling them. Instead, reference cells were used for this procedure.

Reference cells were very similar but not identical to polarized cells. They could be emptied and refilled with any of several gasses including ^3He . The scattered electron counting rates were determined for the reference cell empty and filled with a known quantity of ^3He . In a few instances a half-full rate was also measured for consistency. By taking the difference between the full and empty rates, the ^3He counting rate was determined. It was better to measure the ^3He rate, and then subtract this from the total rate to find the actual target cell glass and nitrogen contribution, than to find the reference cell glass contribution, and then attempt to scale this to the target cell window thicknesses. This was because the quantity of ^3He in the target cell was known more precisely than the window thicknesses, and the sum of glass and nitrogen rates could be determined from the ^3He rate, which was more important than knowing the glass rate alone. The amount of ^3He in the polarized cells was known fairly accurately, so the full rate from the polarized cell minus the ^3He rate determined from the reference cell allowed a determination of the remaining polarized cell rates originating in the glass windows and nitrogen buffer gas.

A measurement was performed for each x -bin in both spectrometers by filling the reference cell with some number of ^3He scattering centers. This total counting

rate was measured, then the reference cell was emptied and the empty counting rate determined. By subtracting the empty rate from the full rate, the ^3He rate was found for a specific number density of ^3He scattering centers. This rate was then scaled to match the ^3He number density in the polarized cell and used in the numerator of Eq. (4.2) for the dilution factor. The measured dilution factor results for each target cell and each spectrometer are presented in Tables 4.3 and 4.4.

4.2.4 Dilution Factor Error Analysis

Many factors contributed to the error bars in Figs. 4.2.4–4.2.4. First, there are statistical uncertainties associated with the limited number of electrons detected in each x bin. Second, there are also uncertainties due to the measurement of the ^3He pressures in the reference cell during the empty and full runs. These measurements were performed using a precision Heise pressure gauge, accurate to about 1/2 psia on a scale ranging to 200 psia. A third uncertainty stemmed from the measurement of the quantity of ^3He in the actual target cell. This measurement was performed in a number of different ways [74] as part of the cell construction process. It was not possible to check this measurement after the experiment for any of the target cells except ‘Picard’, since all the rest exploded. This made it impossible to check for slow leaks which would change the dilution factor over time. Since ‘Picard’ did not appear to have leaked, it was assumed that none of the other cells leaked either.

4.3 E154 Spectrometers

The DIS electrons scattered off the polarized ^3He target were detected using two independent magnetic spectrometers. Two spectrometers were used because the combination improved the data acquisition rate and the kinematic coverage. The spectrometers were operated independently, and effectively performed two si-

Table 4.3. The dilution factor f : results and uncertainties for the 2.75° spectrometer.

	Dave		Riker		Bob	
\bar{x}	f	δf	f	δf	f	δf
0.017	0.58	0.031	0.53	0.032	0.50	0.033
0.025	0.59	0.021	0.54	0.041	0.51	0.023
0.035	0.59	0.022	0.55	0.031	0.52	0.024
0.049	0.59	0.035	0.55	0.024	0.52	0.022
0.078	0.60	0.019	0.55	0.021	0.52	0.034
0.123	0.60	0.039	0.56	0.020	0.52	0.044
0.173	0.60	0.058	0.56	0.021	0.53	0.041
0.241	0.61	0.029	0.57	0.023	0.54	0.069
0.339	0.62	0.029	0.59	0.025	0.55	0.055
0.439	0.63	0.103	0.60	0.083	0.57	0.123
0.516	0.64	0.248	0.61	0.042	0.58	0.104
	SMC		Generals		Hermes	
\bar{x}	f	δf	f	δf	f	δf
0.017	0.52	0.036	0.55	0.036	0.56	0.032
0.025	0.52	0.020	0.56	0.029	0.57	0.035
0.035	0.53	0.015	0.56	0.022	0.57	0.019
0.049	0.53	0.013	0.57	0.017	0.57	0.030
0.078	0.53	0.014	0.57	0.027	0.57	0.019
0.123	0.54	0.023	0.57	0.030	0.58	0.020
0.173	0.54	0.054	0.58	0.032	0.58	0.031
0.241	0.55	0.071	0.59	0.041	0.59	0.018
0.339	0.57	0.082	0.60	0.038	0.60	0.019
0.439	0.58	0.064	0.61	0.042	0.61	0.020
0.516	0.59	0.053	0.62	0.149	0.62	0.062
	Prelims		Chance		Picard	
\bar{x}	f	δf	f	δf	f	δf
0.017	0.61	0.030	0.41	0.029	0.51	0.030
0.025	0.61	0.048	0.47	0.020	0.52	0.019
0.035	0.62	0.026	0.48	0.018	0.53	0.015
0.049	0.62	0.026	0.48	0.018	0.53	0.014
0.078	0.62	0.026	0.48	0.021	0.53	0.015
0.123	0.63	0.031	0.48	0.024	0.54	0.028
0.173	0.63	0.060	0.49	0.023	0.54	0.033
0.241	0.64	0.029	0.50	0.044	0.55	0.019
0.339	0.65	0.023	0.51	0.054	0.57	0.037
0.439	0.67	0.058	0.53	0.033	0.58	0.036
0.516	0.68	0.186	0.54	0.029	0.59	0.042

Table 4.4. The dilution factor f : results and uncertainties for the 5.5° spectrometer.

	Dave		Riker		Bob	
\bar{x}	f	δf	f	δf	f	δf
0.057	0.59	0.119	0.55	0.023	0.51	0.049
0.084	0.59	0.037	0.55	0.019	0.52	0.022
0.123	0.59	0.018	0.55	0.019	0.52	0.029
0.172	0.60	0.020	0.55	0.018	0.52	0.049
0.242	0.60	0.032	0.56	0.019	0.52	0.020
0.342	0.60	0.034	0.56	0.055	0.53	0.020
0.442	0.61	0.034	0.57	0.029	0.54	0.051
0.568	0.62	0.022	0.58	0.032	0.55	0.026
	SMC		Generals		Hermes	
\bar{x}	f	δf	f	δf	f	δf
0.057	0.53	0.075	0.56	0.036	0.57	0.032
0.084	0.53	0.015	0.57	0.018	0.57	0.032
0.123	0.53	0.013	0.57	0.017	0.57	0.023
0.172	0.53	0.013	0.57	0.035	0.57	0.086
0.242	0.54	0.014	0.57	0.018	0.58	0.049
0.342	0.54	0.017	0.58	0.019	0.58	0.021
0.442	0.55	0.041	0.59	0.038	0.59	0.044
0.568	0.56	0.021	0.60	0.046	0.60	0.076
	Prelims		Chance		Picard	
\bar{x}	f	δf	f	δf	f	δf
0.057	0.62	0.185	0.47	0.019	0.52	0.075
0.084	0.62	0.039	0.48	0.023	0.53	0.020
0.123	0.62	0.026	0.48	0.015	0.53	0.013
0.172	0.62	0.097	0.48	0.019	0.53	0.018
0.242	0.63	0.031	0.48	0.024	0.54	0.014
0.342	0.63	0.042	0.49	0.016	0.54	0.070
0.442	0.64	0.097	0.50	0.026	0.55	0.028
0.568	0.65	0.234	0.51	0.050	0.56	0.077

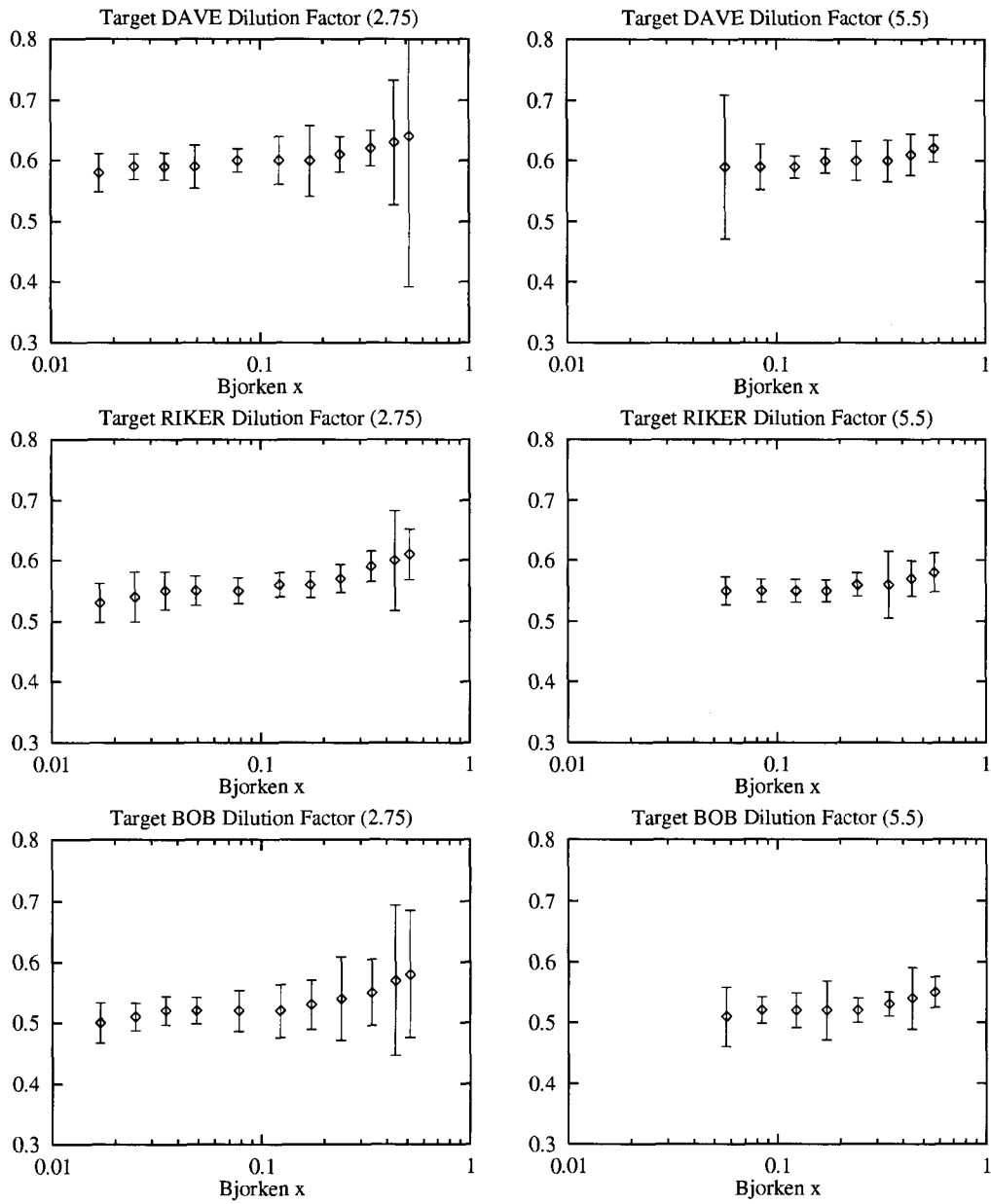


Figure 4.6. Dilution factors for targets 'Dave', 'Riker', and 'Bob'. Dilution factors for the 2.75° spectrometer are shown in the left column and for the 5.5° spectrometer in the right.

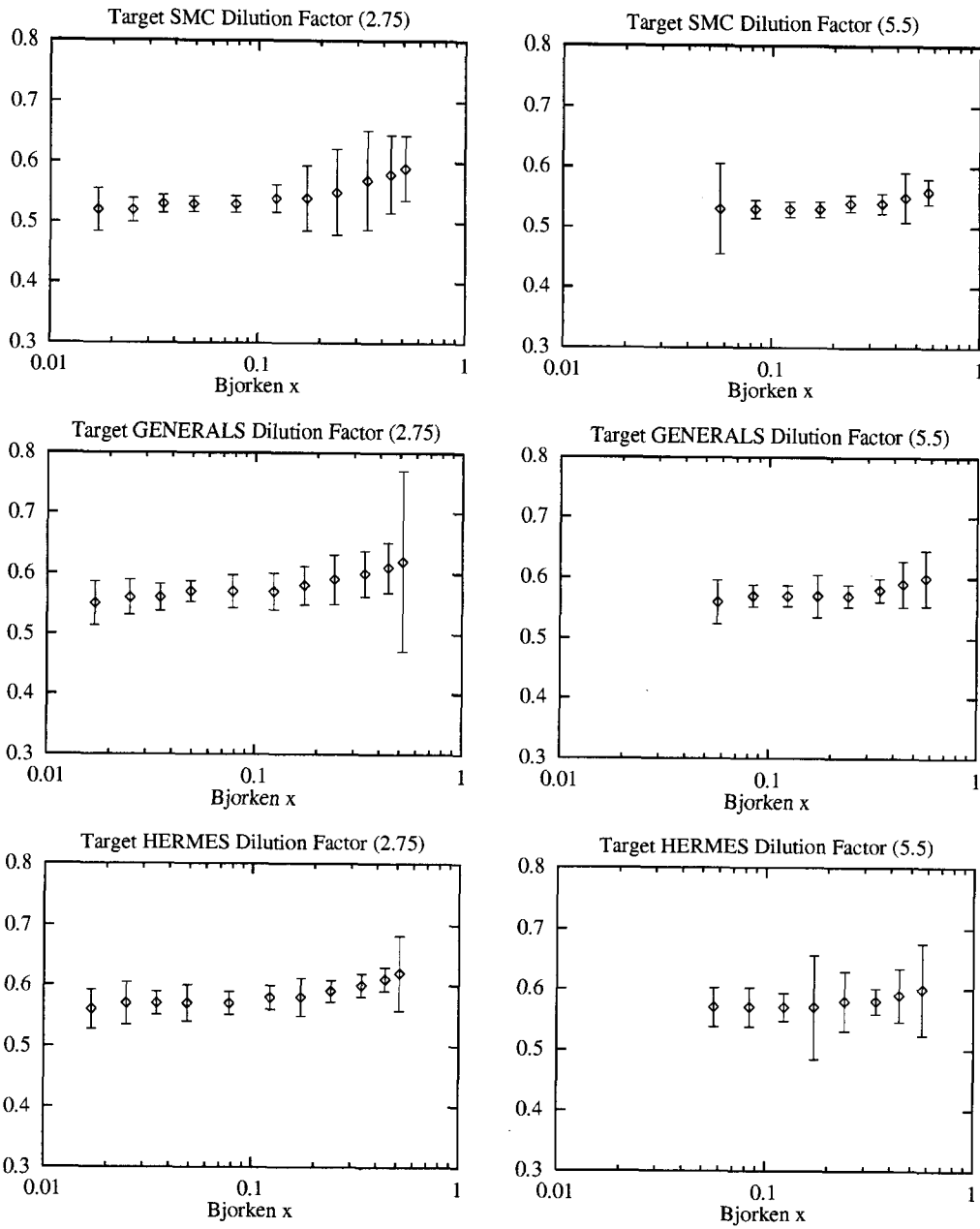


Figure 4.7. Dilution factors for targets 'SMC', 'Generals', and 'Hermes'. Dilution factors for the 2.75° spectrometer are shown in the left column and for the 5.5° spectrometer in the right.

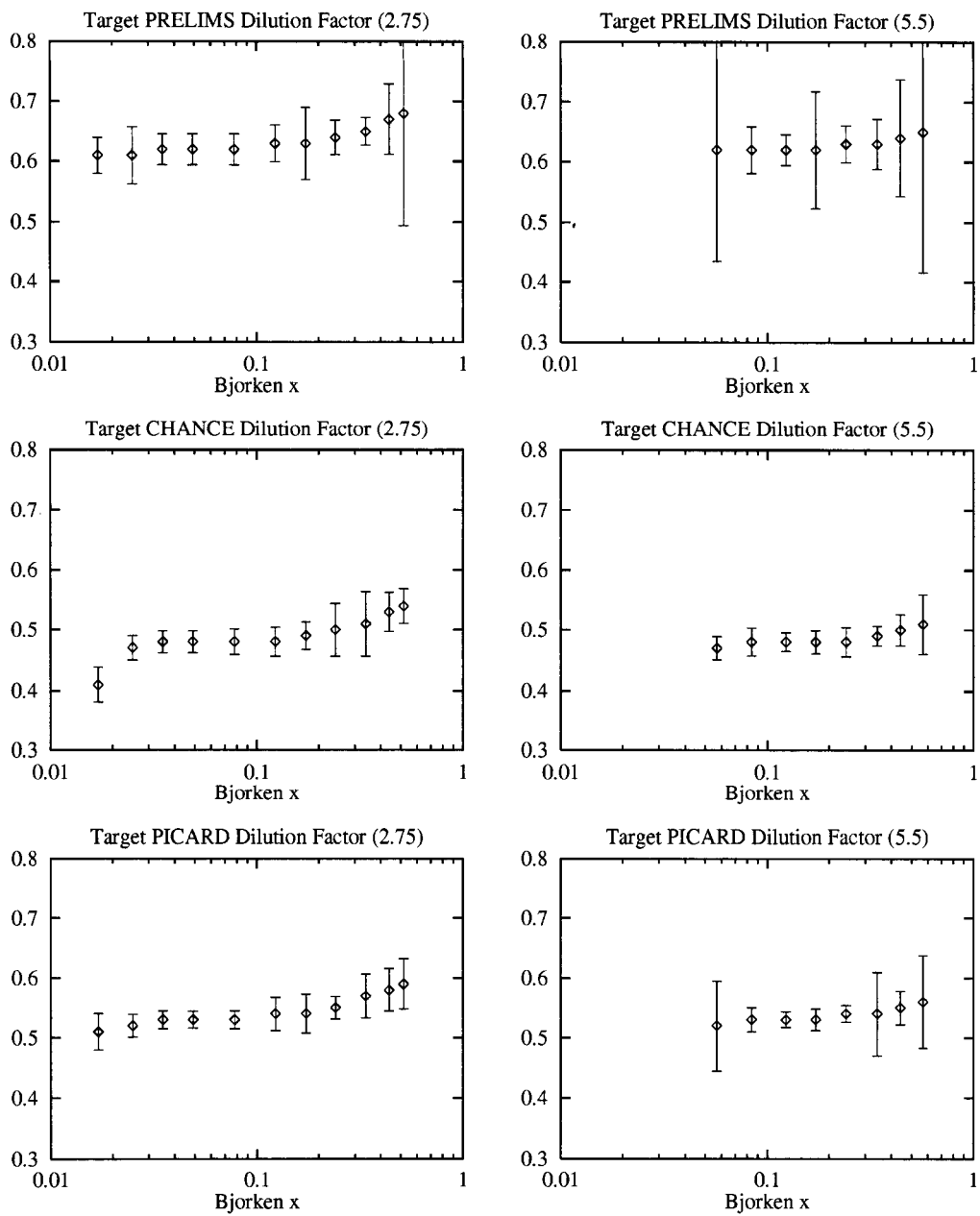


Figure 4.8. Dilution factors for target cells 'Prelims', 'Chance', and 'Picard'. Dilution factors for the 2.75° spectrometer are shown in the left column and for the 5.5° spectrometer in the right.

multaneous measurements of the asymmetries. They were centered around laboratory scattering angles of 2.75° and 5.5° , and instrumented with the same basic components, although the 2.75° detector package contained a greater number of hodoscope planes for better tracking due to the larger background rates at the lower x values covered. A schematic drawing of the two E154 spectrometers showing both the top and elevation views is presented in Fig. 4.9.

The use of two spectrometers at different scattering angles extended the kinematic coverage in x and Q^2 for the experiment as a whole. This was important for calculating the integrals of the measured structure functions over the full x range from 0 to 1, since greater coverage translated to smaller uncertainties in the extrapolations to the endpoints.

The smaller scattering angle of 2.75° was chosen to measure the structure functions at the lowest possible x value. This translated to the smallest achievable scattering angle, which, due to the space constraints imposed by the End Station and the size of the magnets, was 2.75° . The larger scattering angle of 5.5° was chosen to be twice as large as the 2.75° scattering angle, with the goal of investigating the Q^2 dependencies of the structure functions. This scattering angle also interleaved nicely with the 4.5° and 7.0° scattering angles used in the previous ESA experiments, E142 [46] and E143 [47].

With these scattering angles, and an incident beam energy of 48.3 GeV, the accessible x ranges were from 0.014 to 0.6 in the 2.75° spectrometer, and 0.04 to 0.7 in the 5.5° spectrometer as shown in Fig. 4.10. The corresponding momentum ranges, defined by the collimators, were 10 to 46 GeV/c, and 10 to 39 GeV/c. The low momentum cut-off was chosen to minimize the need for radiative corrections. The high momentum range was limited by the maximum beam energy and the deep inelastic cutoff of $W^2 > 4 \text{ GeV}^2$.

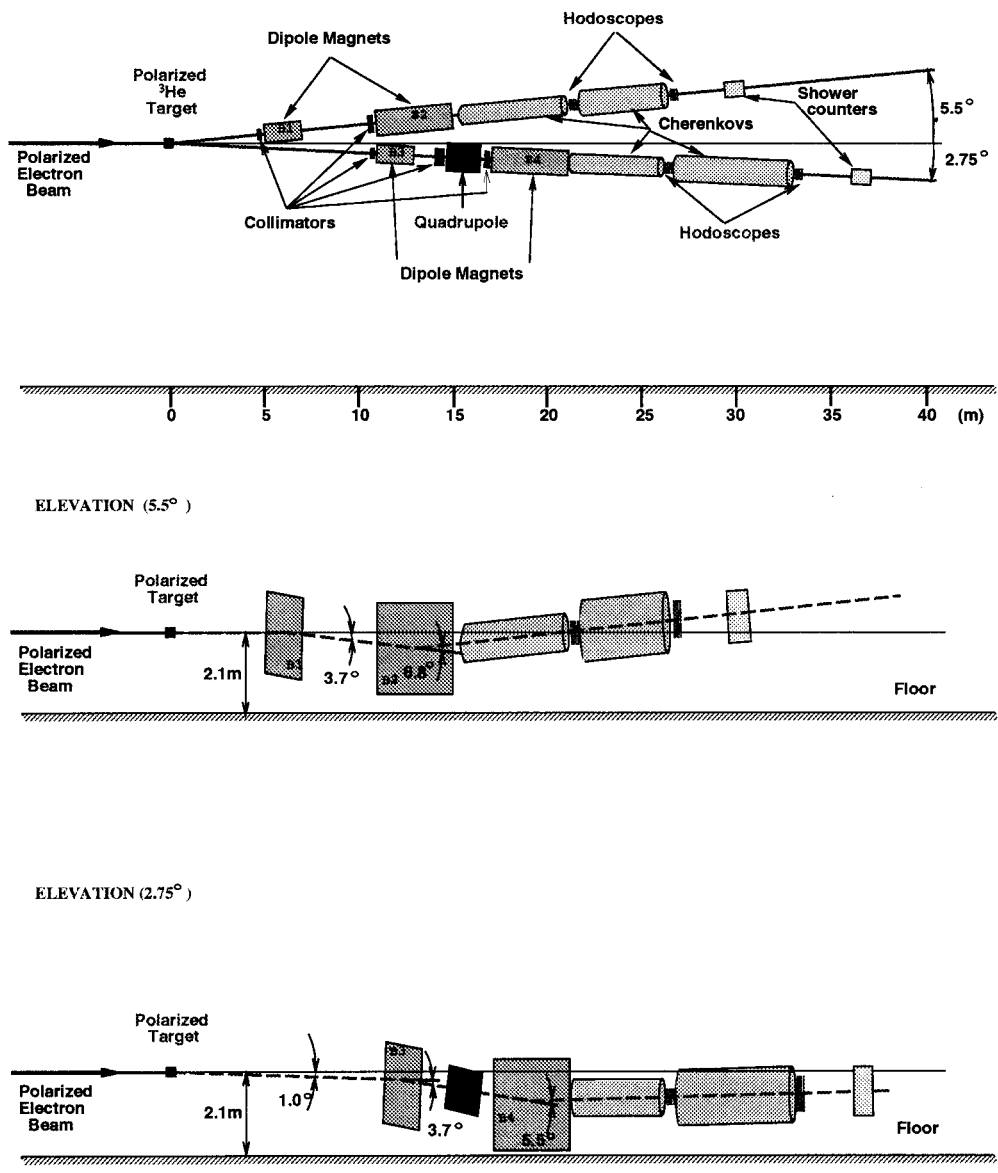


Figure 4.9. The E154 spectrometers.

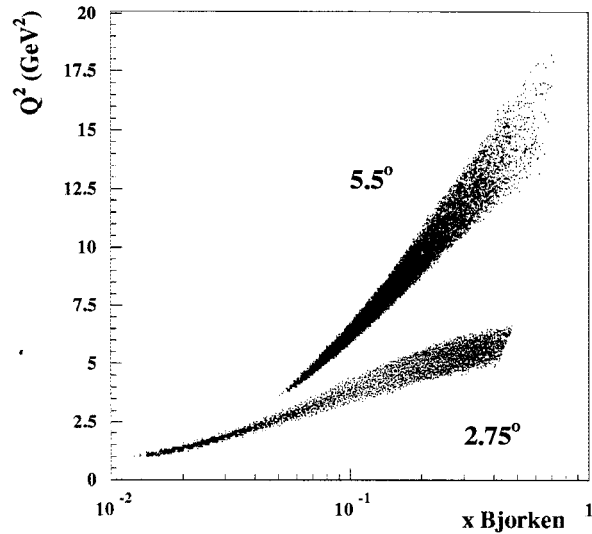


Figure 4.10. The x and Q^2 coverage of the two E154 spectrometers for an incident beam energy of 48.3 GeV.

Both spectrometers were designed with the goal of maximizing the detected event rate while retaining the ability to cleanly identify electron tracks in the presence of a large background of pions and low-energy neutral particles. The designs grew out of the E142 and E143 spectrometer designs, and actually used most of the same components and the same ‘S-Bend’ shape.

The DIS cross section of Eq. (2.16) drops precipitously with increasing scattering angle, so the 5.5° spectrometer was designed with a large solid angle in an attempt to increase the event rate and minimize the statistical uncertainties of the spin structure function measurements. By contrast, the 2.75° spectrometer had movable collimators which allowed the solid angle acceptance to be adjusted. This ability was necessary to be able to limit the particle rate to the maximum acceptable rate in the detectors. The acceptance was adjusted each time the beam current changed, so several different acceptances were used during the experiment.

4.3.1 Magnetic Optics of the Spectrometers

Both spectrometers were arranged in an S-bend configuration as shown in the elevation views in Fig. 4.9. This type of spectrometer configuration was advantageous for two reasons. First, it substantially reduced the neutral particle background, consisting mostly of high energy bremsstrahlung photons, by requiring them to scatter off apertures at least twice in order to reach the detector elements. This was termed the ‘two bounce’ requirement. Second, it allowed a relatively large solid angle acceptance in a confined space.

The spectrometer coordinate systems were right-handed and defined with the central scattering angle of each spectrometer as the \hat{z} direction. The \hat{x} direction was horizontal (north in End Station A), and the \hat{y} direction pointed up (to the ceiling). Angles in the bend-plane (\hat{y} - \hat{z}) were labeled ϕ , and angles in the non-bend plane (\hat{x} - \hat{z}) were labeled θ .

4.3.1.1 The 2.75° Spectrometer Optics

The magnetic optics components for this spectrometer consisted of two dipole magnets positioned so as to deflect electrons in opposite directions, with a quadrupole in between the dipoles. The central momentum trajectory, defined to be 20 GeV/c, was deflected down 3.7° by B3 and back up 5.5° by B4. This is shown in the lower elevation view in Fig. 4.9. The quadrupole magnet was used to spread the particle paths out in the horizontal direction, helping to reduce the instantaneous rates in the detectors. It was also adjusted to make the pion rate as uniform as possible in the vertical (bend) direction, and to assist the movable collimators in defining the optimum solid angle acceptance. In addition, the quadrupole provided a momentum focus for electrons in the vertical direction. This assisted in rejecting pions since only a small range of electron energies were allowed for a given shower block position.

The dipoles, B3 and B4, were operated with fields of about 1.5 Tesla and 1.9 Tesla respectively. The quadrupole, Q1, was set at a field gradient of 5.6 T/m. The magnetic fields produced by these magnets were extensively mapped prior to the experiment, allowing Monte Carlo simulations of the optics to be performed.

The limiting apertures were defined by the openings of the three sets of collimators shown in the top view of Fig. 4.9. Opened to their maximum, the solid angle could be as large as 0.2 msr. During the experiment, the collimators were generally closed enough to limit the acceptance to 0.1 msr, keeping the event rate at a manageable level in the detectors.

4.3.1.2 The 5.5° Spectrometer Optics

The 5.5° spectrometer was very similar to the 2.75° spectrometer, but because the electron scattering cross section and pion production rate are smaller at this angle, no quadrupole was required to spread events out. Also, the collimator openings were fixed in their widest position to maximize the solid angle acceptance.

This spectrometer was positioned on the north side of the beam line in End Station A. Like the 2.75° spectrometer, it also consisted of an S-bend using two dipoles, B1 and B2, operated at about 0.9 Tesla and 2.2 Tesla. B1 was positioned 2.0 m from the target, this being as close as possible while making sure the fringe field did not affect the polarized target operation. Magnet B1 deflected electrons with a central momentum of 20 GeV down 3.5° and B2 deflected them back up again through an angle of 6.8°.

This spectrometer also followed the two bounce criteria for neutral particles from the target to reach the detector packages. The bend angles were set to accept electrons from about 10 GeV/c up to the maximum possible, 39 GeV/c, at this scattering angle from a 48.3 GeV beam, including the requirement that $W^2 > 4$

GeV². As in the 2.75° spectrometer, the angular resolution in the non-bend plane (θ) was about 0.3 mr.

4.4 Detector Systems

The basic detector systems were identical for both spectrometers, although the specifics varied. They consisted of a 6 m gas Čerenkov detector, a hodoscope package, another 6 m gas Čerenkov detector, another hodoscope package, and finally a lead-glass shower counter array. The Čerenkov detectors were primarily used for particle identification between electrons and pions, which were the primary background. The hodoscopes were used for position measurements to define tracks, and the lead-glass blocks served the dual roles of determining the detected electron energy and position. The lead-glass data was used both for particle identification and tracking.

4.4.1 Čerenkov Detectors

The four Čerenkov detectors used in this experiment were labeled 2C1 and 2C2 in the 2.75° spectrometer, and 5C1 and 5C2 in the 5.5° spectrometer as shown in Fig. 4.9. All four detectors were operated in the same fashion, and differed only in their operating pressures, and in their physical dimensions, which were determined by their positions in the spectrometers. Low pressure nitrogen gas was used as the refractive material, and the generated Čerenkov light was reflected off three spherical mirrors inside each detector to a single 5 inch photomultiplier tube. One of the unique aspects of this experiment was that the Čerenkov signal from each phototube was digitized using a Struck Flash ADC, so multiple tracks could be detected with better timing accuracy and shorter dead time than by simply using TDCs.

4.4.1.1 Čerenkov Detector Operation

When a charged particle passes through a material with index of refraction n , the particle will radiate Čerenkov radiation if its velocity is greater than the velocity of light *in the material*. This light is the electromagnetic version of a supersonic shock wave, and is described in detail in the text by Jackson [75]. The threshold above which Čerenkov radiation is emitted is given by the relation

$$\beta n > 1, \quad (4.10)$$

where $\beta \equiv v/c$ is the particles velocity, v is a fraction of the speed of light c , and n is the index of refraction of the material. The angle between the particle's momentum and the direction at which the Čerenkov radiation is emitted, θ_c , is given by

$$\cos(\theta_c) = \frac{1}{\beta n}. \quad (4.11)$$

The index of refraction for a gas can be related to the gas density through the Lorenz-Lorentz law [76]

$$\left(\frac{n(\lambda)^2 - 1}{n(\lambda)^2 + 2} \right) = K(\lambda)\rho \quad (4.12)$$

where λ is the wavelength of light, ρ is the density, and $K(\lambda = 546 \text{ nm}) \approx 0.163 \text{ cm}^3/\text{g}$. For a typical gas this may be simplified somewhat since $n \simeq 1$, thus

$$\frac{(n-1)(n+1)}{n^2+2} \simeq (n-1)\frac{2}{3}. \quad (4.13)$$

Combining Eqs. (4.13) and (4.12) yields

$$(n-1) \simeq \frac{3\rho K(\lambda)}{2}. \quad (4.14)$$

The density can easily be determined using the ideal gas law.

Using these relations, and the gas pressures in the Čerenkov detectors of 1.4 psia and 2.0 psia, the light emission angle is found to be effectively zero degrees, *i.e.*, straight ahead for electrons, and the pion thresholds are at about 19 GeV and 16 GeV.

4.4.1.2 Wavelength Shifters

Since the Čerenkov light was primarily emitted at very short, ultraviolet wavelengths, a thin coating of Para-Terphenyl was used on the phototube as a wavelength shifter. By increasing the wavelength into a region where the phototubes were more sensitive, the Čerenkov signals were significantly enhanced.

4.4.1.3 Čerenkov Electronics

The phototube signals were collected at both the dynode and the anode. The anode signals were sent to flash ADC's, where the signals were digitized in 1ns time slices. The dynode signal was copied using LeCroy 428F fan-outs, and sent to a set of LeCroy 623B threshold discriminators adjusted for different thresholds. The discriminated dynode signals were subsequently input into LeCroy 2277 TDCs which measured the start times for each 'hit'. The TDC information was used as a backup for the digitized waveform from the flash ADCs.

4.4.2 Hodoscopes

The hodoscopes consisted of arrays of Bicron BC404 plastic scintillators arranged to facilitate tracking. The scintillators were mounted in planes roughly perpendicular to the central momentum ray. Each plane consisted of a number of parallel scintillator 'fingers', which measured the particle position in the direction perpendicular to the length of the finger due to the segmented nature of the arrays. The great majority of the planes measured track positions in either the \hat{x} or \hat{y} dimensions directly, but the first 2 planes were a u-v pair placed at a 30° angle with respect to horizontal. The positions of each plane in the spectrometers are shown in Fig. 4.11.

Each scintillator of each hodoscope was connected to its own phototube, whose output signal was transmitted via RG58 coaxial cable to LeCroy 3412 multichannel

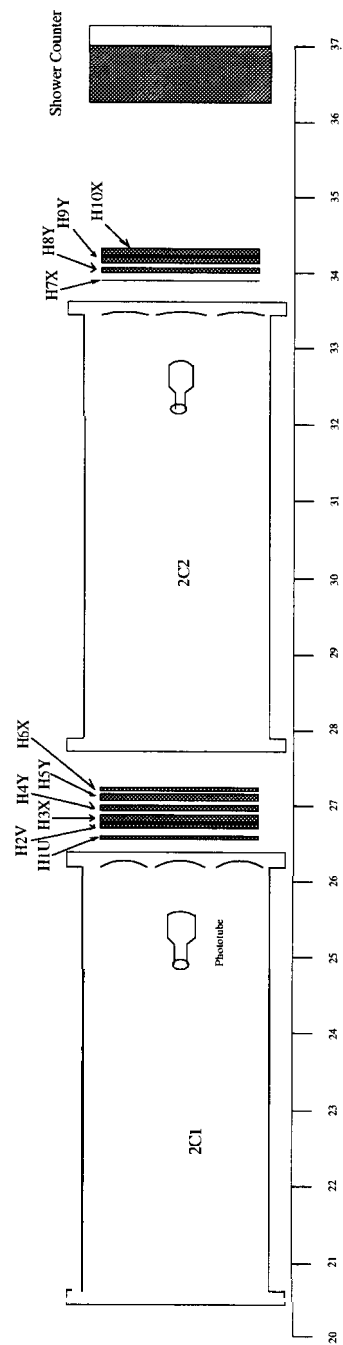


Figure 4.11. A schematic of the detector systems for the 2.75° spectrometer. The scale is in meters, measured from the target position.

discriminators. The discriminated output signal was subsequently sent to a LeCroy 3377 multihit TDC channel where the leading edge times for each hit were recorded and ultimately relayed to the data acquisition system. Cable lengths were adjusted so that the signals from all hodoscopes would fit into a single time window during which the TDCs were active.

A timing offset was determined for each finger to determine the actual time when the particle traversed the finger from the TDC value. This determination proceeded through a series of bootstrap style refinements using the tracking system to calculate the expected time, and adjusting the timing offset accordingly. With the final timing offsets calculated, the hodoscope information was used by the tracking program to determine particle track parameters.

4.4.3 Lead Glass Shower Counter Arrays

The final detector element in each of the two spectrometers was an array of lead glass blocks arranged as shown in Fig. 4.12. Both arrays were identical and consisted of 200 blocks of $6.2 \times 6.2 \times 75$ cm F2 lead glass in a rectangular array 10 blocks wide by 20 blocks tall. This arrangement allowed a position measurement for electrons which was much better than the segmentation. It also generated an electron energy measurement with an uncertainty of $3\% + 0.8/\sqrt{E}$ in GeV. The length of each lead-glass block corresponded to about 24 radiation lengths for high energy electrons, making this a total absorption calorimeter for electrons.

In general, electrons generate showers in lead-glass and pions do not, allowing a fairly clean separation between the two types of particles.

Like the hodoscopes, each lead-glass block was connected to its own phototube. The phototube signal was transmitted through RG58 coaxial cable to a set of *passive splitters* which split each signal into two unequal portions of 17% and 83%. The

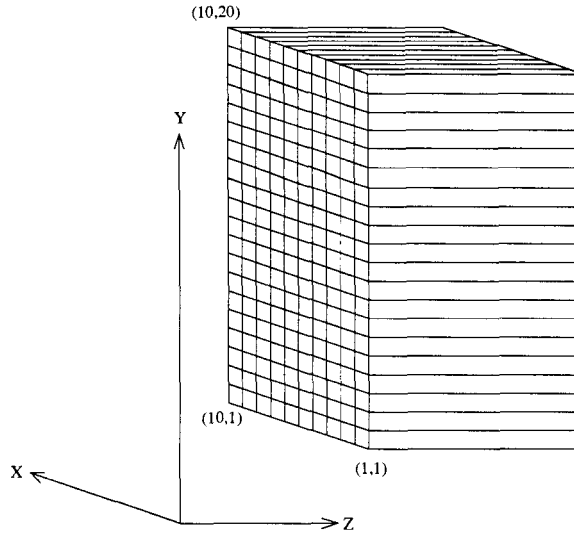


Figure 4.12. Arrangement of the shower counter blocks shown with the spectrometer coordinate system axes. Particles entered the detector from the left, traveling in the \hat{z} direction, and the phototubes (not shown) were on the downstream end of the blocks. The numbering of the blocks in 'block coordinates' is shown by the coordinate pairs for three of the corner blocks.

larger portions of the signals were sent via preamps to discriminators and TDCs, while the smaller portions were sent directly to LeCroy 2280 ADCs.

4.5 Spectrometer Electronics

Most of the data acquisition electronics modules were near the spectrometers inside the 2.75° spectrometer shielding hut. This was a new arrangement for End Station A experiments, which in the past sent all raw signals to the counting house where the electronics modules were readily accessible. This experiment, however, had so many individual data channels that it was impossible to transmit all of them to the counting house through long cables. Instead the electronics and readout system were located near the spectrometers, making cabling much cheaper.

The electronics schematic for E154 is shown in Fig. 4.13. Cable lengths were adjusted so that signals from the detectors arrived at the electronics modules within the same time window, limiting the number of trigger signals required, as described in section 4.5.1.

The various types of modules used were primarily chosen from the available 'pool' of End Station A electronics. As shown in Fig. 4.13, a large number of LeCroy 428F Fan-Outs were utilized for copying signals from the detectors, and sending the analog copies on to the next stage, as was done with the 64 channels from the 2.75° shower counter which were instrumented with multiple discriminator levels, and with the Čerenkov dynode signals, which were also compared to multiple discriminator levels. Most discriminators were LeCroy 3412 modules, although a number of LeCroy 4413 and LeCroy 623B modules were also used. The modules accessible to the data acquisition system were the LeCroy 2280/2282 ADC systems, the LeCroy 2277 and 3377 TDCs, and the Struck Flash ADCs which were contained in a single VME crate.

The eight LeCroy high voltage power supplies were mounted upstairs in the counting house for easier access. The high voltages were carried to the detectors through long, coaxial, high voltage cables. All high voltage chassis were operated by the high voltage control program, which set and monitored each of the voltages for each detector element. This information was available at every checkpoint in the data stream, as described below in Section 4.6.1.

One of the time-intensive jobs performed during the setup phase of the experiment was connecting all of the cables from the many detector channels to the appropriate electronics modules. As there were nearly 2,000 individual data channels for the two spectrometers, it was imperative to provide a system for checking that these cables were all connected to the correct channels on the correct modules, and that each data path was in good working order. A small data acquisition system called the 'MiniDAQ' was written for this purpose, and used to check every system except the VME modules.

A number of detectors provided test signals which could be used to check the integrity of each complete path. The Čerenkov detectors each had an LED in-

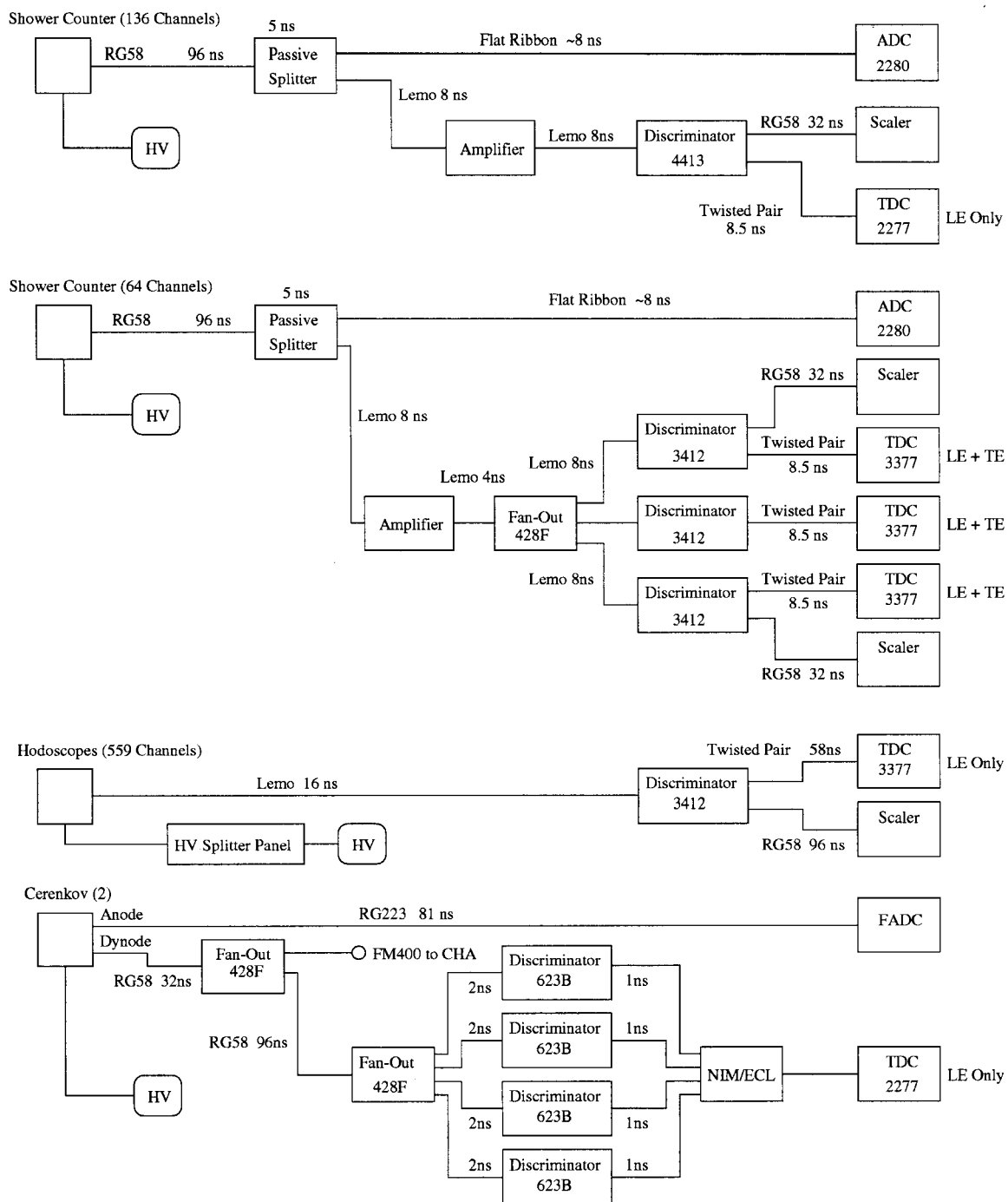


Figure 4.13. E154 electronics schematic for the 2.75° spectrometer branch.

side them which could be pulsed to generate a flash of light onto the phototube, mimicking true Čerenkov data. Similarly the shower counters contained a Xenon flash lamp, which when pulsed generated a small light pulse in each of the lead-glass blocks, mimicking a true shower signal. The hodoscopes were more difficult to test since they did not have a test signal generator mounted on the detectors directly. They used the test mode of the discriminators to generate an output from the discriminators, allowing the subsequent chain of cables and TDCs to be tested. During the experiment, each channel of each detector was monitored to make sure counts were being detected. Several 'dead' hodoscope fingers and lead-glass blocks were found this way.

4.5.1 Trigger Electronics

Due to the high event rate for the experiment, all modules were read out by the computer every beam pulse. Hence the trigger logic was relatively simple. A timing signal from the accelerator, termed A2N, was received and suitably delayed to generate the various gates required by the different electronics modules in the data stream. Unlike the acquisition electronics, the trigger logic was entirely in the counting house, and the eight individual gates were sent to the 2.75° spectrometer shielding hut via coaxial cables. The gates generated were a TDC start and a TDC stop, an ADC gate which spanned the time between TDC start and TDC stop, a start signal for the flash ADCs, and several diagnostic signals to run test equipment: the Xenon flash lamp, the LED pulser, and the discriminator test pulser. The E154 trigger electronics schematic is shown in Fig. 4.14.

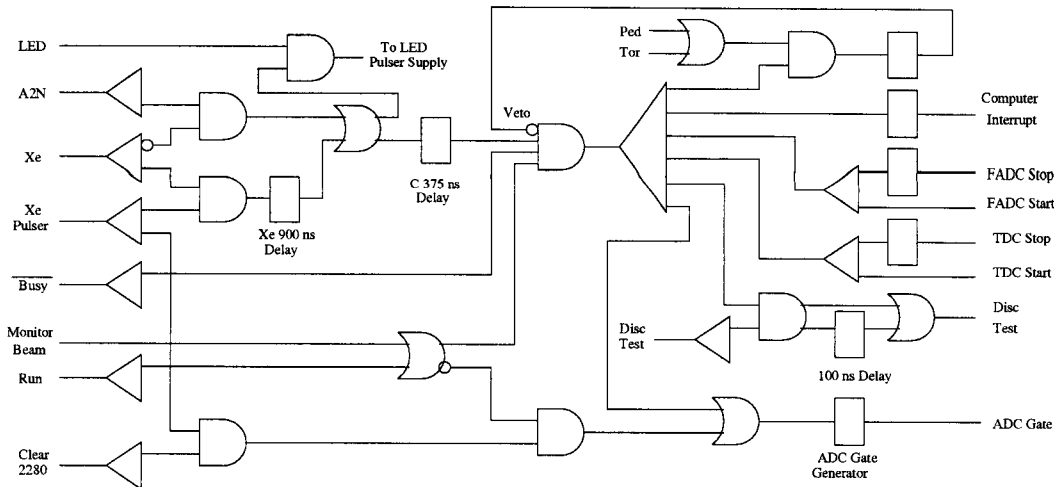


Figure 4.14. E154 trigger electronics schematic

4.6 Data Acquisition Systems

The high data rates expected for this experiment required a new data acquisition system to be designed. The acquisition system needed to be able to handle data rates of at least 1 Mbyte/sec. It also needed to be able to read electronics modules separated by large distances, and transfer the data to a remote tape system over a network. These requirements led to the development of a VME based data acquisition (DAQ) system, linked through reflective memory, TCP/IP, FDDI protocols. The complete system is described in detail in [77].

The heart of the system consisted of three VME crates interconnected through a reflective memory system. The reflective memory allowed all three VME controllers to share the same physical memory, and transfer data through it. With the long cables required between the remote crate near the spectrometers and the local crates in the counting house, the data rate through the reflective memory system was limited to about 1.4 Mbyte/sec – far below the design rating for the system of 2.5 Mbyte/sec, but well above the minimum required rate of 1 Mbyte/sec.

Since the majority of the electronics modules were contained in CAMAC systems, three VME-CAMAC interfaces were purchased, one for each of the two CA-

MAC branches servicing the two spectrometers, and one to operate the beam CAMAC crate in the counting house. These were VME modules which contained CAMAC controllers, allowing the VME system to operate the CAMAC branches. These modules could be operated in parallel, significantly improving the data rate, which was usually limited by the slow speed of the CAMAC bus.

The two 'local' VME crates were located in the counting house, and were responsible for controlling the overall DAQ system. One was primarily used for diagnostic purposes, while the other crate contained modules for accepting interrupts and sending the data over the FDDI link to the tape silo system for storage. This crate also interacted with online analysis processes which could request copies of the event data through the TCP/IP protocol.

4.6.1 Checkpoints

Checkpoints were short (30 second) breaks in the experiment, during which data which were not expected to vary substantially over many spills could be written to the data tape. Every run started and ended with a checkpoint, and for most of the experiment they were taken every five to ten minutes. Many items were included in the checkpoint list including the beam and target polarizations from the most recent measurement, all CAMAC crate voltages recorded by the low voltage monitoring system, all high voltage supply voltages recorded by the high voltage control system, many temperature and pressure transducer measurements, and all A-line related statistics recorded by the MCC control program. This information was never used in detail during the analysis, but was available to allow portions of runs to be utilized even if other parts of the run might be found to have problems with some system. The checkpoint information was used to determine the A-line magnet settings used during each run as part of the beam tune studies discussed

in section 3.6. Checkpoint data was routed through the VME based DAQ system via the TCP/IP network protocol.

4.6.2 Data Rates

The average data rate during E154 was about 500 kbytes/sec, corresponding to about 4 kbytes at 119 Hz. It ranged as high as 700 kbytes/sec, with high beam currents and noisy detectors. The limiting factors at the highest rates were the two spectrometer CAMAC branches, which could only transfer one 16 bit word every $2 \mu\text{s}$. The data size for each spill fluctuated significantly, ranging from a minimum of about 2 kbytes to a maximum of 12 kbytes. The maximum size was set by the capacity of the buffer for reading the data. Occasionally spills generated more data than could fit in the 12 kbyte buffer. This caused a 'truncation' flag to be turned on in the spill 'header', allowing the spill to be thrown out during the analysis phase. Truncations were monitored closely during the experiment. A truncation rate was calculated for every run, measuring the number of truncations of each helicity divided by the total number of spills. Every attempt was made both to keep the overall truncation rate as low as possible, and to ensure that the rates were the same for both the left and right helicities.

An additional problem related to the data rate occurred when the data size from each spectrometer CAMAC branch neared or exceeded 5000 bytes at 120 Hz. Under these conditions, the local and remote VME controllers could lose synchronization, and either start combining data from different spills, or get stuck in a 'race condition' where both controllers expected the other to clear the 'system busy' flag. These errors could be rectified by issuing a pause command from the DAQ control console, which reset each of the controllers to a 'waiting for interrupts' state.

4.6.3 Data Storage

A system of automated tape servers was used to store the data from the experiment, making most of the details of tape handling transparent. Six tape drives were available which could access any of 1,000 tapes in a 'silo', and either download the data to a disk file for access, or write disk files onto the tapes. During data acquisition a dedicated pool of 80 Gbytes of disk space was available to the experiment to buffer the data before being written onto the tapes. This provided some flexibility in the event of tape drive failures. Data was usually written onto the tapes within an hour of the run, so that the disk pool never became close to full.

After the experiment was completed, two copies were made of the full data set onto 8mm tapes. One set was taken to Caltech for their analysis program, and the other set was kept at SLAC.

CHAPTER 5

DATA ANALYSIS

5.1 Outline

The E154 data were simultaneously analyzed by two groups. One group remained at SLAC, while the other took a full copy of the raw data tapes to the California Institute of Technology (Caltech). There were two reasons for doing multiple analyses. First, eleven graduate students worked on this experiment and planned to use it with different emphases being placed on its various aspects for their dissertation topics. Second, two separate analyses provided the opportunity to perform additional internal consistency checks, thereby reducing the likelihood of mistakes. The Caltech analysis is described in detail in two thesis dissertations [78, 79]. Both analyses started with the same raw data from the experiment, but diverged with completely different shower counter analyses, slightly different Čerenkov treatments, and were run on different computers (DEC Alphas at Caltech, and IBM RS6000's at SLAC). In the end both groups arrived at essentially identical results, increasing our confidence that the procedures used were correct, and error free. Only the SLAC analysis, which the author of this thesis participated in, will be reported here.

The SLAC data analysis proceeded in two steps. In the first step, Čerenkov 'hits', hodoscope 'mini-clusters' and shower 'clusters' were identified in the raw data. All of these constructions were subsequently used to find particle 'tracks' in the spectrometers. Additionally, the wire array pulses were fitted to find the cen-

troid and size of the beam. This information, along with several other parameters, listed in section 5.3, was then saved on Data Summary Tapes (DSTs). The second stage of the analysis used the DST data to determine the asymmetries. Corrections to account for backgrounds, radiative effects, and the dilution factor were performed during this phase. Many systematic checks of individual systems were also performed using the DST data.

Splitting the analysis into two steps had several advantages over attempting to do everything at once. First, finding all Čerenkov hits, shower counter clusters, and tracks, plus fitting the wire array data typically took 25 to 30 hours on the IBM RS6000 computers. It was much more efficient to only do this once, and use the resulting track information in the subsequent analysis steps, than to redo the tracking every time a new effect needed to be investigated. With 40 computers running in parallel, it still took two and a half months to produce all the DSTs. Second, the volume of data stored on the data summary tapes was much smaller than on the raw data tapes, providing easier and quicker access for subsequent analysis tasks. A typical run, consisting of about 200,000 beam spills, contained roughly 830 Mbytes of raw data, which was typically condensed to about 200 Mbytes on the produced DST. Once the data summary tapes were available, a single run could be read off a DST and analyzed for asymmetries in about fifteen minutes.

5.2 Raw Data Analysis

Data from individual detector systems were analyzed separately, the exception being tracking, which used information from all of the detector systems. Each of the individual system analyses will be described, culminating in the tracking system in section 5.2.5. Analysis of the wire array data has been described previously in Section 3.7.1.4.

5.2.1 Čerenkov Analysis

The raw data from the Čerenkov detectors consisted of the flash ADC digitized waveforms. TDC times, which were provided as a backup for the flash ADCs, were not utilized in the SLAC analysis (see section 5.2.1.1). The digitized waveforms were analyzed to find the times, maximum voltages, and integrated charges of pulses. A typical waveform with several ‘hits’ is shown in Fig. 5.1

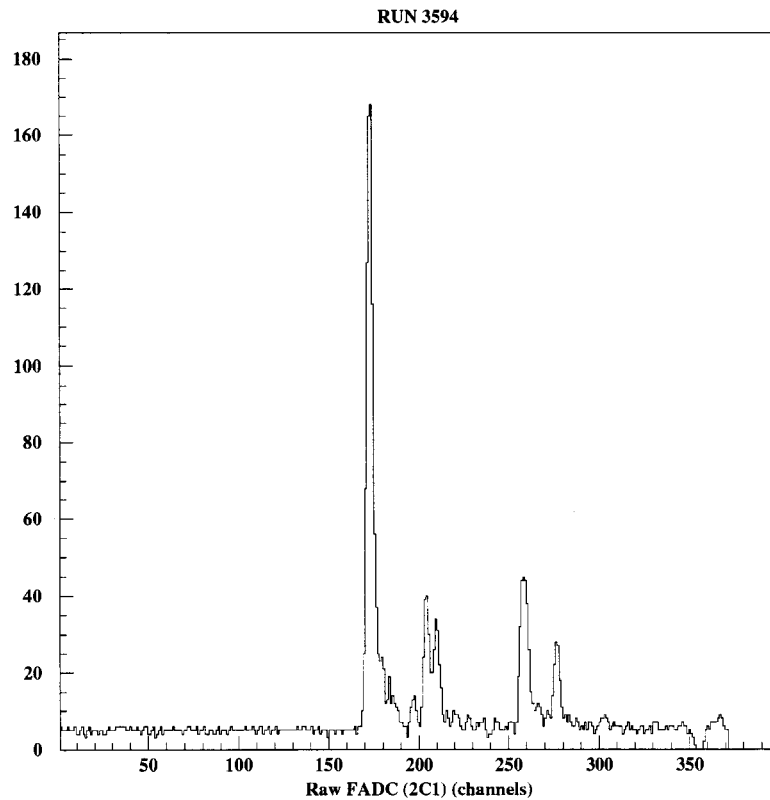


Figure 5.1. Typical Čerenkov waveform. The left axis is in units of FADC ‘voltage’ which is roughly equivalent to mV. The horizontal axis is the time into the spill, and has units of ns.

The raw FADC data consisted of a series of bytes representing the signal voltage in one nanosecond time slices. Pulses were identified in the raw waveform through the following algorithm: first, the derivative was calculated by finding the voltage difference between successive channels. Pulses were found by determining where the derivative was greater than a threshold value, which was optimized for each

individual Čerenkov detector to maximize the ratio of the electron signal to noise. The width of the pulse was determined by finding the corresponding negative part of the derivative. Next, a baseline (background) was determined by averaging channels that were not included in any pulses. This average baseline was then subtracted from the raw waveform to produce a baseline-subtracted waveform. Finally, the baseline-subtracted waveform was used to determine the start time for each pulse by fitting a straight line through three waveform points including the one immediately before the start of the pulse (identified in the previous step), and using the x-intercept of this fit as the pulse start time.

Before analyzing the next ‘hit’, the tail of the average waveform for the pulse preceding it was first subtracted from the data. The average waveform was simply a function of the integrated charge of the pulse, and was well determined from spills with only one hit. All succeeding pulses in the spill were handled identically. Note that a change in the algorithm to systematically shift the start times either direction would have been inconsequential, since it could be absorbed into the overall timing offset for the Čerenkov detector. The algorithm returned the start time, the peak voltage, and the integrated charge for every peak above threshold in the raw waveform.

An improved algorithm using Fourier transform methods [80] was tested recently, and found to be significantly better at resolving closely spaced hits in time. However, the technique was only developed after DST production, so it will not be discussed further.

5.2.1.1 Čerenkov Timing Error

Late in the analysis it was discovered that the Čerenkov pulse times had an anomalously wide distribution of about 1.3 ns when compared to the track times, whereas about 0.7 ns was expected from the phototube characteristics. The resolu-

tion of this problem involved the realization that the Flash ADC (FADC) clock was continuously running at 250 MHz. Thus, when the FADC ‘start’ signal arrived it could take as long as 4 ns before the FADC started performing conversions synchronized with its internal clock. [81]. Because of this non-synchronization, the ‘time’ of a given channel could shift randomly by as much as 4 ns. A software solution for this problem was created by using the backup TDC information to find the true start times for hits, and thus determine a timing offset for each spill.

The SLAC analysis group was already generating DSTs by the time this effect was discovered, and decided to ignore the problem, as the deterioration in the Čerenkov timing resolution was less than 1 ns. The Caltech group used the improved timing in their analysis, and found effectively the same overall results as the SLAC group. As a second check, a new set of DSTs was produced at SLAC in the spring of 1997, which included the Čerenkov timing correction. All of the runs on target PICARD were analyzed. The results differed only negligibly from the original DSTs, so the decision was made not to continue producing the new DSTs [82].

5.2.1.2 Čerenkov Pulse-Height Timing Correction

The Čerenkov algorithm described in section 5.2.1 was found to produce a skewed timing distribution which depended on the peak voltage of the Čerenkov pulse. This was compensated for with a simple correction of the form [83]

$$t_{cor} = t_{raw} + \frac{C}{\sqrt{V_{peak}}}, \quad (5.1)$$

where t_{raw} was the time found by the original algorithm, V_{peak} the peak voltage of the pulse, and t_{cor} the corrected time. The constant C was determined experimentally by fitting the pulse times relative to the track times.

5.2.1.3 Time-of-Flight Timing Correction

A final correction to the Čerenkov pulse times accounted for the propagation time of the Čerenkov light from the mirror surfaces to the phototube. The correction was normalized relative to a track at the geometrical center of each mirror, for which the correction was zero. Since this correction required tracking information, it was performed in the tracking routine described in section 5.2.5.

5.2.2 Hodoscope Analysis

The raw data from the hodoscopes consisted of the TDC signal start times from each scintillator finger. The TDC channels were mapped to finger number and plane number, with appropriate timing offsets subtracted to account for cable lengths, phototube delays, and geometrical position. All times were offset to find the ‘target’ time of the pulse, meaning the time at which a particle traveling at the speed of light would have been at the target. These timing offsets were determined iteratively by using the tracking system to compare expected times with actual times. The improvement in hodoscope timing resulted in improved track timing resolution, with final timing resolutions of ~ 1 ns being realized for most hodoscope fingers.

As with the Čerenkov time-of-flight timing correction, the measured hodoscope times required adjustments for the light propagation time between the track positions in each scintillator finger and the attached phototube. Since many of the fingers were quite long, the light propagation time resulted in timing shifts as large as 4 ns. Correcting the hodoscope times to account for the light propagation time required tracking information, so it was done by the tracking algorithm described in section 5.2.5.

5.2.3 Shower Counter Analysis

The lead glass shower counter data consisted of both charge (ADC) and timing (TDC) information. Multihit TDCs were used to measure both the start (leading edge) and the stop (trailing edge) times for each hit up to a maximum of 16 hits per block. However, only a single ADC measurement of the total charge collected from the photomultiplier tube over the full 250 ns spill duration was available for each block. The goal of the shower counter analysis program was to determine the time, position, particle type, and energy of each detected shower signal.

5.2.3.1 Cells and Energy Sharing

The first step of the shower counter analysis consisted of finding ‘cells’ of energy. A cell was defined as the energy deposited in a block at a given time. A single block could contain up to 16 cells spread out over time, the number being limited by the capacity of the TDCs.

Energy cells were found by using the TDC start and stop times to ‘share’ the single ADC energy measurement appropriately between multiple hits. For the case where only one TDC start-stop combination existed in a spill the energy was uniquely determined by the ADC measurement. However, in general, more than one hit was recorded in a given block over the duration of a spill. In this more complicated case there were two discrete possibilities for ‘sharing’ the single energy measurement between individual cells.

The first possibility occurred when multiple hits were spaced far enough apart in time for each individual pulse to be well resolved by the TDC(s). For resolved hits the energy of the cell was estimated using the length of time above each discriminator threshold as [84]

$$E(\Delta t) = E_{Th} \left[1 + \frac{1}{b} \left(e^{\Delta t/a} - 1 \right) \right], \quad (5.2)$$

where E was in GeV, E_{Th} was the discriminator threshold converted to GeV, Δt was the time difference between trailing and leading edges of the signal from the TDC, and a and b were constants determined by fitting to the actual waveform. A sketch of a typical waveform is shown in Fig. 5.2 showing three discriminator thresholds and the corresponding Δt measurements. Some channels were connected to three discriminator levels and some to only one as described in Chapter 4.

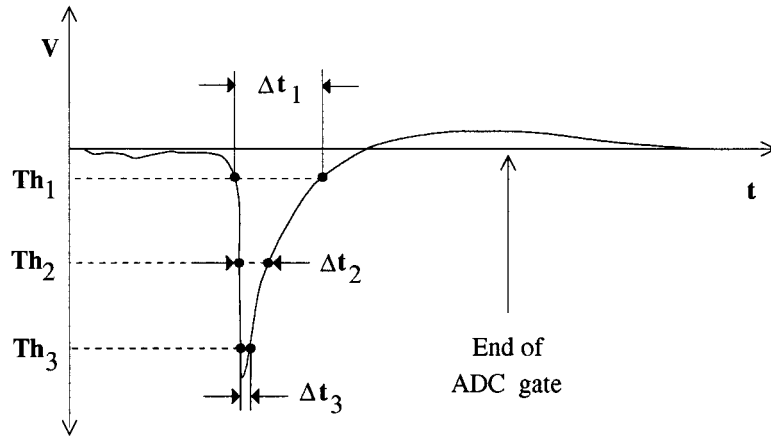


Figure 5.2. Sketch of a typical signal from a shower counter block as a function of time. The discriminator thresholds for three levels are shown along with the corresponding Δt measurements. The ‘overshoot’ above ground at the end of the pulse is also shown. The vertical arrow shows where the end of the ADC integration window (gate) occurs. For shower signals which happen later in the spill, less charge will be subtracted from the integral of the charge due to the overshoot, because the signal will spend less time above ground before the end of the measurement window.

The other possibility for sharing energies occurred when some of the cells were unresolved by the TDC(s), and labeled as ‘bad’. Bad cells occurred when the discriminator output pulse was either longer than 30 ns, or shorter than the minimum TDC resolutions of 9.5 ns for the LeCroy 3377 TDCs and 17 ns for the LeCroy 2277 TDCs. The 30 ns maximum was imposed to make the formula in Eq. (5.2) reliable.

The final step in generating energy ‘cells’ was to spread all available energy out amongst the cells according to the following algorithm: the total calculated energy

for ‘good’ cells, defined by Eq. (5.2), was summed to E_{tot} and compared with E_{ADC} , the total energy from the ADC measurement. If a block only contained ‘good’ cells, each cell’s calculated energy was scaled to the total available energy E_{ADC} as

$$E_{Cell} = \left(\frac{E_{Calc}}{E_{tot}} \right) \cdot E_{ADC}. \quad (5.3)$$

If a block also contained ‘bad’ cells, two procedures were followed depending on whether E_{tot} was greater than or less than E_{ADC} . For $E_{tot} < E_{ADC}$, each ‘good’ cell’s calculated energy was used directly, and the remaining energy, $E_{ADC} - E_{tot}$, was distributed equally among the ‘bad’ cells using

$$E_{Cell} = \left(\frac{E_{ADC} - E_{tot}}{N_{bad}} \right). \quad (5.4)$$

For $E_{tot} > E_{ADC}$, each cell’s calculated energy was scaled using Eq. (5.3), and the ‘bad’ cells received no energy.

It should be noted that while the energy resolution for ‘bad’ cells was quite poor, this was not particularly detrimental to the overall energy resolution for showers, because showers usually encompassed many blocks, most of which contained ‘good’ cells.

5.2.3.2 Building Shower Clusters

Once the individual cell energies and times were determined the next step in the shower counter analysis combined the cells into ‘clusters’. This was accomplished using a ‘cellular automaton’ algorithm which was modeled on biological principles. The cells were in a three dimensional space consisting of the x and y positions of the block containing the cell, and the time of the cell. A cell’s nearest neighbors were the eight blocks spatially surrounding the block containing the cell (see Fig. 5.3), and within 5 ns in time. Each cell was checked against its nearest neighbors, and defined as a ‘virus’ cell if it had the largest energy compared to its neighbors.

In other words, the virus cells were the set of local energy maxima. There were as many virus cells as showers in the counter.

The cellular automaton routine scanned through the cells, using ‘virus’ cells to ‘infect’ neighboring healthy cells, until no healthy cells remained. Each cell was checked: if it was already a virus cell, it was skipped. If it was healthy, all of its neighboring cells were checked to see if they were ‘virus’ cells. If a virus cell was found, it ‘infected’ the current cell with its virus. Once infected, a cell was considered ‘immunized’, meaning it could no longer be infected by any other virus cell. Infected cells received the index of the original virus which infected them, so blocks of infected cells could be grouped into ‘clusters’ whose infections stemmed from the same virus cell. This process is described in more detail in reference [86].

Once clusters were formed, the 2-dimensional ‘centroid’, average time, and first moments were calculated for each cluster. These values corresponded to the position, time, and ‘size’ measurements of the shower. The centroid was defined as the center-of-gravity of the energies in the 9 blocks surrounding and including the central block of a cluster (the original virus cell):

$$\bar{x} \equiv \frac{\sum E_i x_i}{\sum E_i}; \quad \bar{y} \equiv \frac{\sum E_i y_i}{\sum E_i} \quad (5.5)$$

for both the x and y dimensions, where E_i was the energy of the i^{th} cell, and x_i , y_i were the coordinates of the center of the block containing the i^{th} cell. The first moment, which was a measure of the transverse ‘size’ of the cluster, was calculated using [86]

$$\sigma_x \equiv \frac{\sum E_i (x_i - \bar{x})^2}{\sum E_i}, \quad (5.6)$$

$$\sigma_y \equiv \frac{\sum E_i (y_i - \bar{y})^2}{\sum E_i}, \quad (5.7)$$

and

$$\sigma_{xy} \equiv \frac{\sum E_i (x_i - \bar{x})(y_i - \bar{y})}{\sum E_i}. \quad (5.8)$$

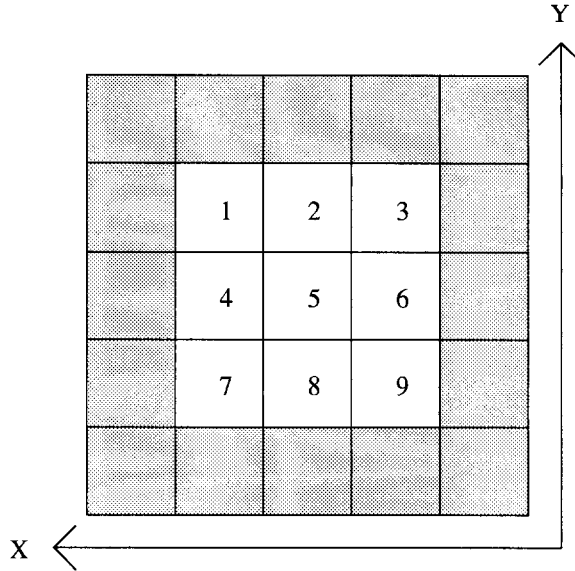


Figure 5.3. Beam's view of the central nine blocks of a cluster, surrounded by the sixteen 'second corona' blocks (shaded).

The shower counter cluster positions, times, and sizes determined in this fashion were used by the tracking system, and served as inputs to the neural network particle identification algorithm.

5.2.4 Shower Counter Neural Network

The heart of the shower counter analysis code was a neural network trained to distinguish between showers initiated by pions, and showers originating with electrons. A neural network was chosen because the problem consisted primarily of distinguishing between 'shapes' of showers. A feed-forward network with one hidden layer and 13 inputs was used to differentiate the two types of showers from each other. The inputs to the neural network were the energies of the 9 blocks of the cluster, the sum of the energies of the next surrounding layer of 16 blocks called the 'second corona' (see Fig. 5.3), the total energy (E_{total}) of the cluster, the ratio $E_{central}/E_{total}$, and the number of blocks comprising the cluster.

The neural net was trained on a very pure sample of pions and a pure sample of electrons obtained from special runs. It returned its determination of the particle type originating the shower as a number between -1.0 and +1.0, where -1.0 meant pions and +1.0 meant electrons. Its ability to determine pions was very good, so electrons were defined as not pions, and any output greater than -0.98 was considered an electron. The neural network was tested with a second set of pure electrons and pure pions, and subsequently used for all runs.

5.2.4.1 Timing Correction for Shower Energies

The energy measurement for shower clusters was found to have a modest dependence on the time [85]. This dependence was discovered by investigating the ratio of the shower counter energy to the track momentum determination (E/P) as a function of time. For high energy electrons the E/P value should be ~ 1.0 . The measured E/P ratios vs. time are shown for each spectrometer in Fig. 5.4. The time slices are 27 ns wide and the data is from run 2480. The fits shown in the figure are

$$\frac{E}{P}(t) = 0.707 + 1.65 \times 10^{-2} t - 1.82 \times 10^{-6} t^2 \quad (5.9)$$

for the 2.75° spectrometer, and

$$\frac{E}{P}(t) = 0.792 + 1.27 \times 10^{-2} t - 1.43 \times 10^{-6} t^2 \quad (5.10)$$

for the 5.5° spectrometer, where t is the TDC start time of the cluster.

The probable reason for this E/P time dependence was that the phototubes, which generated a negative pulse, overshoot ground and went positive at the end of each pulse. This behavior is shown in the shower signal sketch in Fig. 5.2. The result of overshooting ground was that pulses late in the spill integrated less signal above ground than earlier pulses. Thus late pulses were measured as having a larger signal than earlier ones, in agreement with the plots in Fig. 5.4.

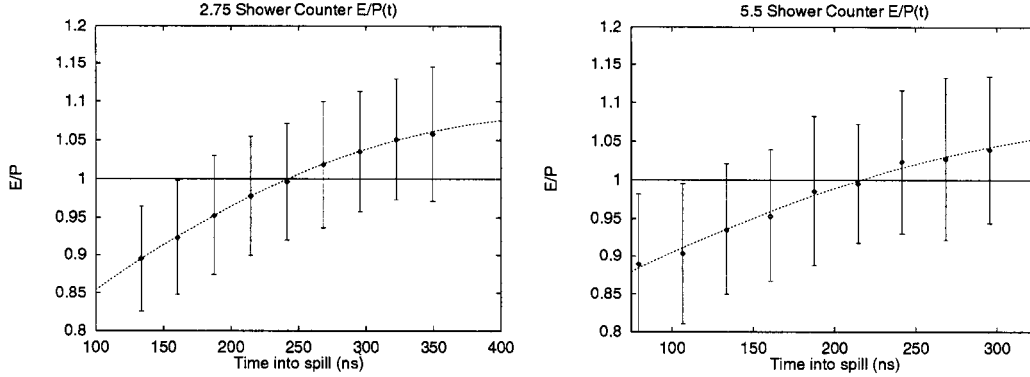


Figure 5.4. E/P as a function of time in the spill for the 2.75° spectrometer (left) and the 5.5° spectrometer (right). Values are taken from run 2480. The error bars show the standard deviation of each E/P distribution, and were not utilized in making the fits.

5.2.5 Tracking

The tracking system utilized the information from all of the detector elements to determine each detected particle's momentum and scattering angle, and to make a simple determination of its type using the Čerenkov detectors. This was a complicated task, not only because each spill typically contained between 15 and 25 particle tracks, which had to be identified, but also because many of the detector elements were quite 'noisy', producing extraneous 'hits' which masked the true particle signals. Fortunately, it was possible to use a number of cuts to limit the possible signals in any detector which could be caused by a specific particle. The algorithm is described below in general terms. More detail may be obtained from reference [87].

The tracking system defined four track 'classes' as shown in Table 5.1. These classes were exclusive, meaning no track could be a member of more than one class. Class I tracks were electron candidates, and class II tracks were pion candidates. Classes III and IV were used for diagnostic purposes such as determining timing offsets for the hodoscopes, and were not relevant to the asymmetry analysis.

Table 5.1. Track classes: all definitions include hodoscope hits.

Class	Definition
I	Shower Cluster, Čerenkov
II	Shower Cluster, No Čerenkov
III	No Shower Cluster, Čerenkov
IV	No Shower Cluster, No Čerenkov

The optics of the spectrometers were such that only a small swath across the shower counter surface area was kinematically accessible to electrons, a property which limited the number of tracks to be determined.

For simplicity, the times for all detected events were converted to their corresponding target times under the assumption that the responsible particles were traveling very near the speed of light. The conversion was performed using

$$\tau = t - z/c, \quad (5.11)$$

where τ was the time at the target, z the distance from the target to the detector element, and c the speed of light. The time t at the detector element was obtained from the TDC measurements after accounting for cable lengths and start signal delays.

Shower counter clusters falling within the electron acceptances of the spectrometers were identified, and used to specify an initial time for a track candidate. A small timing window of ± 5 ns around this track time was then searched for corresponding Čerenkov hits. If one or more Čerenkov hits were found, the track was changed from class II to class I, and the track time was changed to the average of the cluster and Čerenkov time(s).

Finally, the hodoscope TDC times were searched for hits falling within the narrow ± 5 ns window around the track time. Typically, many hodoscope hits were found due to the high event rate and noisy environment. To deal with this large number of hits, the front and rear packages of hodoscope planes (see Fig. 4.11) were

analyzed by finding mini-clusters of spatial coincidences between hodoscope fingers of different planes. To simplify the search, all planes of a package were projected onto a single z -position at the last plane of the package. Then the first two planes were searched for all overlapping combinations of fingers. Each overlapping pair was replaced by a rectangular area defined as a ‘mini-cluster,’ as shown in Fig. 5.5. For convenience the rectangles were not rotated, but kept aligned horizontally and vertically as shown. Then the next plane was searched for any hit fingers which overlapped either the previously found miniclusters, or hit fingers from the previous two planes. This process was repeated with each successive plane of the package, so that after the last plane was searched only a small number of mini-clusters remained.

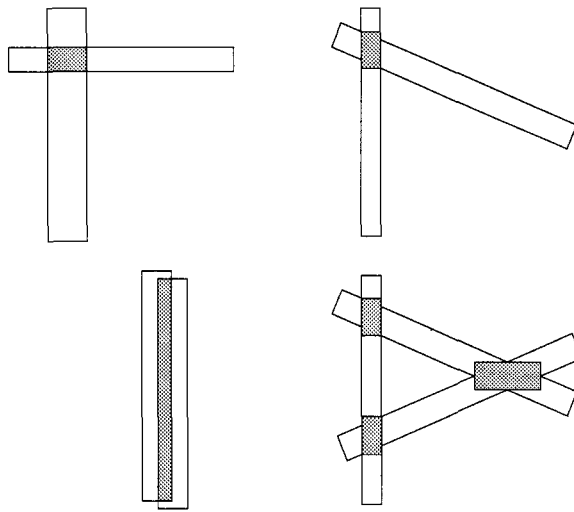


Figure 5.5. Examples of hodoscope ‘mini-clusters’ in the tracking system.

At this point tracks were constructed using the shower cluster positions and times, the Čerenkov times, and the hodoscope mini-cluster positions and times. Since there were no magnets between the detector elements in the spectrometers, all tracks through the detectors were straight lines. Multiple scattering effects in the detector elements were ignored. To improve performance, the fit was performed

in the time dimension first by minimizing

$$\chi^2 = \sum_i \left(\frac{\tau_0 - \tau_i}{\sigma(\tau_i)} \right)^2, \quad (5.12)$$

where τ_0 was the average time of the shower cluster and Čerenkov combination projected back to the target, τ_i were the target times of the various hodoscope miniclusters, and $\sigma(\tau_i)$ were the detector dependent resolutions for these time measurements. As the fit in time alone did not provide a unique determination of individual tracks, since several tracks could occur simultaneously at different locations, a maximum χ^2 was defined, and any mini-clusters outside this maximum value were removed from the track search set.

Then, the full fit was performed in both space and time dimensions. Five parameters were found: the line intercepts (x_0, y_0) , the slopes (Θ, Φ) , and the target time, τ_0 of the track. These were determined by minimizing

$$\chi^2 = \sum_i \left(\frac{(x_0 + z_i \Theta) \cos \theta_u + (y_0 + z_i \Phi) \sin \theta_u - u_i}{\sigma(u_i)} \right)^2 + \sum_j \left(\frac{\tau_0 - \tau_j}{\sigma(\tau_j)} \right)^2. \quad (5.13)$$

The angle, θ_u specified the dimension measured by the value u_i . For hodoscope planes, θ_u measured the angle between the orientation of the fingers and the vertical direction (because the position sensitivity of the hodoscopes was perpendicular to the finger direction.) Specifying the measured dimensions as u_i allowed the so-called u and v hodoscope planes, which measured the x and y dimensions simultaneously, to be included in a single formula.

As described in sections 5.2.1.3 and 5.2.2, a correction which accounted for the light propagation time between the track position and the detector phototube was made to the target times for both the Čerenkov and hodoscope hits. For the Čerenkov detectors, the nominal positions were the centers of the mirrors, and the correction was calculated using

$$\Delta\tau = \frac{1}{c} [D_{tp} - D_{mp}], \quad (5.14)$$

where the distance between the track position at the mirror and the phototube was

$$D_{tp} \equiv \sqrt{(x_0 + z_m \Theta - x_p)^2 + (y_0 + z_m \Phi - y_p)^2 + (z_m - z_p)^2}, \quad (5.15)$$

and the distance between the center of the mirror and the phototube was

$$D_{mp} \equiv \sqrt{(x_m - x_p)^2 + (y_m - y_p)^2 + (z_m - z_p)^2}. \quad (5.16)$$

The subscript m refers to mirror center coordinates, p to the the phototube coordinates, and 0 to the ‘target position’ in the straight line projection of the spectrometer coordinates pretending no magnetic optics were present. The two angles Θ and Φ were the track directions, or slopes, obtained from the track parameter fit described above.

The light propagation time correction for the hodoscope fingers was relative to the center of each finger. A phenomenological light propagation speed was determined for each individual finger, which varied between 135 and 213 mm/ns due to the varied geometries, internal reflection characteristics, and scintillator to photo-tube interfaces. As a reference, the index of refraction of the Bicron BC404 scintillator material used is 1.58, resulting in a light propagation speed of 190 mm/ns [87].

After making these corrections to the Čerenkov and hodoscope times, the combination of hits resulting in the ‘best’ track was determined. This was accomplished by calculating the time and spatial residuals, and looking at the χ^2 defined in Eq. (5.13). The maximum, χ_{max}^2 was set at 16 (8 for the Čerenkov hits which had no spatial content). The numbers were set so the maximum χ^2 per degree of freedom was slightly larger than one. The hit with the worst (largest) χ^2 was compared to χ_{max}^2 . If $\chi_{worst}^2 > \chi_{max}^2$, this hit was removed from the set of hit candidates. The entire track was discarded if either the number of hits in the hodoscope packages dropped below a minimum threshold of three (four in the 2.75° front package), or

one of the sums

$$\sum_{planes} |\cos \theta_u|, \quad \sum_{planes} |\sin \theta_u| \quad (5.17)$$

dropped below 0.5 for either of the hodoscope packages in a spectrometer. This requirement assured that both x and y projections were determined.

The full process, starting with determining new track parameters using the shower cluster, the Čerenkov hit(s) (for class one), and the remaining hodoscope miniclusters was then repeated. The fitting algorithm continued until either all hits' residuals were less than χ_{max}^2 , or the track candidate was dropped due to one of the two conditions stated above.

5.2.6 Tracking Performance

The tracking system efficiency was estimated from the ratio of the difference between numbers of shower counter clusters and tracks to the number of shower clusters, $(N_{cluster} - N_{track})/N_{cluster}$. This ratio actually yielded an inefficiency which, for electron clusters, was always less than 10%. So the tracking system was able to find tracks leading to over 90% of the clusters identified by the neural network as due to electrons.

The resolution of the track parameters found by the tracking system was estimated using data generated by Monte Carlo simulations of the spectrometers. A well developed GEANT simulation generated 'data' in the same format as true event data. The Monte Carlo data were analyzed as if they were real event data, and then compared with the original tracks [87].

The reconstructed track time resolution using the Monte Carlo data was found to be about 0.3 ns in both spectrometers. The momentum resolution was 2.4% in the 2.75° spectrometer and 2.7% in the 5.5° spectrometer. Finally, the angular resolutions for tracks were about 0.4 mr in both spectrometers for both angles.

5.3 Data Summary Tape Production

As described at the beginning of this chapter, data summary tapes were produced using the raw data analysis as described above. For each spill, enough information needed to be saved to calculate the asymmetries and run all the systematic studies desired. The beam information was mostly copied directly, since it did not require any computing time to determine, and was also relatively small in size. The exception was the wire array which underwent the fitting described in section 3.7.1.5. A complete list of the items saved on the DSTs is listed below:

- Spill number
- Run number
- A-line beam position monitors (3 BPM's, 1 Traveling wave monitor)
- Truncation flag (if data was truncated)
- Time slot
- Wire array flags (any ADC dropouts)
- Monitors (good spill, bad spill, SEM, lead-glass)
- Polarization (4 methods)
- Toroids
- Wire array centroids and widths (both dimensions)

Each spectrometer was analyzed independently, but the same set of information was saved in both cases:

- Truncation flag (if data overflowed buffer size)
- Number of tracks
- Number of Čerenkov hits in each tank
- Number of shower clusters
- Track information: for each track
 - Class
 - Number of hits comprising the track
 - Shower cluster number used

Number of Čerenkov hits used
 Čerenkov hit numbers used (each tank)
 Which hodoscope planes were hit
 Track time
 Track momentum
 Track angle Θ
 Track angle Φ
 Track target position (z)
 Track coordinates (x, y, z) at the target
 Track direction cosines

- Čerenkov information: for each hit
 - Integrated charge
 - Target time
 - Peak voltage
- Shower information: for each cluster
 - Number of blocks in cluster
 - Class (encodes possible problems generating cluster)
 - Pileup flag - if more than one hit/block
 - Edge flag - if cluster is centered in an edge block
 - Energy of 3×3 cells with TDC
 - Energy of cluster
 - Energy of each of the nine blocks of the cluster
 - Coordinates of cluster (x, y)
 - Neural network result for cluster

Data summary tapes were produced for all data runs numbered higher than 1321. Pedestal, toroid, and other calibration runs were skipped, but no other run selections were made at this stage. Once the DSTs were available, it was possible to analyze the saved information to generate asymmetries. It should be noted that many of the items saved on the DSTs were not needed for the asymmetry analysis directly, but were kept so systematic studies could be performed quickly with the available data.

5.3.1 Run Selection for the Asymmetries

Only runs after 1322 were analyzed. The earlier runs were not considered useful for the asymmetry analysis since many detector constants were still being determined, and systems changed frequently, while attempting to make everything work together. Of the remaining runs (1322 - 3788), many were special runs such as pedestal and toroid calibrations, reference cell runs for the dilution factor measurements, or Møller runs, and were excluded from the asymmetry analysis. Any run with logbook entries describing a problem was also removed from the list. Typical problems included things such as the power supply for the A-line failing, spectrometer magnet power supply crashes, high voltage supply failures for the detectors, bad pedestals in the ADCs, and a whole host of other possible problems. Whatever the cause, these sorts of runs were marked as 'bad', and were not used for the asymmetry determination.

Another type of problem which could exclude a run from the asymmetry determination was related to the beam quality. Problems with polarization measurement mismatches, charge asymmetries, and position asymmetries were investigated. The polarization mismatches meant one or more of the four methods (PMON, MACH, HV, and prediction) disagreed with the others. Runs where this occurred in more than a few spills were discarded as unreliable. If only a few spills exhibited problems these spills were cut (see Table 5.2).

The 'charge asymmetry', or difference between total incident charge for the two polarization states, was defined as

$$|A_{charge}| \equiv \left| \frac{(Q^\uparrow - Q^\downarrow)}{(Q^\uparrow + Q^\downarrow)} \right|. \quad (5.18)$$

A non-zero asymmetry could be caused by many factors, starting with the polarized source lasers behaving differently for the different polarization states. *A priori* this should not have mattered, since the incident charge was measured very accurately

for each spill. However, many systematic errors were minimized for equal intensities of left and right helicities. Because of this, it was important to try to minimize the ‘charge asymmetry’, and for the second half of the experiment it was typically kept at the 10^{-4} level per run. Runs with asymmetries greater than 5×10^{-4} , a total of 34 otherwise fine runs, were discarded [88].

Finally a cut was made on the beam ‘position asymmetry’ as measured by the wire array. This was defined as the difference between average centroid positions for the two helicities,

$$|A_{position_x}| \equiv | \langle x \rangle^\uparrow - \langle x \rangle^\downarrow |, \quad (5.19)$$

and

$$|A_{position_y}| \equiv | \langle y \rangle^\uparrow - \langle y \rangle^\downarrow |. \quad (5.20)$$

Runs outside the limits of $|A_{position_x}| \leq 0.004$ mm and $|A_{position_y}| \leq 0.005$ mm were excluded from the asymmetry determination, eliminating 33 runs [88].

The runs which were used for the final analysis are listed in Appendix A.

5.3.2 Beam Cuts

A detailed analysis of the data from the beam monitors described in Chapter 3 was performed with the goal of being able to set the analysis cuts on these detectors to reasonable levels. There were several ways of analyzing beam monitor data for this purpose. First, one could assume that the only effects of importance were those which altered the measured asymmetries, leading one to split the data into several bins for each of the beam monitors, and then investigate the differences in the resulting asymmetries for the different data sets. For example, the data could be split into two groups, depending on whether the wire array centroid position was greater than or less than the central value. Each of these two data sets could be used to determine the asymmetry, and the results compared. If a dependence was found, i.e. the two asymmetry measurements disagreed, this would be cause

for concern and require very careful cuts. Such a program was carried out for the good spill monitor, the bad spill monitor, the lead-glass monitor, the two toroids, and the wire-array. No dependence was found in any of these monitors which was correlated with helicity at a level which could be used to set cuts.

The second way of looking at the beam monitor data was to plot the number of detected electrons/incident electron as functions of the data in these monitors. If the ratio was not uniform, then cuts would be required to limit the analysis to regions where the ratio did not vary. When this program was carried out for each of the beam monitors, several slight dependencies were found, but nothing significant enough to require detailed cuts.

The third and final option for investigating beam cuts was to determine the average value and RMS deviation for the data in each of the monitors for each run. One could then require cuts at some number of standard deviations from the average, and be fairly confident that the beam characteristics would remain stable for the run. This was done with both tight ($\pm 1\sigma$) cuts, medium cuts ($\pm 3\sigma$), and loose cuts ($\pm 5\sigma$) for each of the beam monitors. Essentially the only difference between the results (both asymmetries and counts/incident electron) was in the number of electrons surviving the cuts to produce asymmetries. Since none of these cuts appeared to have any effect on the results of the analysis, they were left very loose. Only one cut actually mattered in the end, and that was the toroid cut requiring a minimum beam current. This cut eliminated the witness pulses. The final cuts used by the SLAC analysis are listed in Table 5.2.

5.3.3 Electron Definitions

The parallel and perpendicular experimental asymmetries of Eq. (2.100) were defined for ‘detected electrons.’ However, determining what was actually an electron was a fairly complicated process. High energy pions could mimic electrons in

Table 5.2. Beam cuts for the asymmetry determination. The units for the good and bad spill are ADC counts, the units for the toroids are 10^{10} electrons/spill, and the units for the wire array are mm. The only cuts of any real significance were the toroid cuts, which eliminated the witness pulses.

Monitor	Minimum	Maximum
Good Spill	0.0	2000.0
Bad Spill	0.0	2000.0
Lead Glass	no cut	no cut
Toroid 2	1.0	no cut
Toroid 3	1.0	no cut
Wire Array x	0.0	4.0
Wire Array σ_x	0.5	3.0
Wire Array y	-4.0	0.0
Wire Array σ_y	0.3	3.0
Polarization bit mismatches	N/A	N/A

most of the detectors. By varying the definition of what combination of detector signals constituted an electron, insight was gained into many of these backgrounds. Additionally, the optimum electron definition, which retained the true electrons while rejecting background events, was determined. The final electron definition used for determining the asymmetries is specified below:

- Beam cuts (see Table 5.2)
- Tracking cut (phase space in spectrometers)
- Class 1 track
- Both Čerenkov detectors responded with peak ‘voltages’ greater than 25 FADC units
- Neural net result > -0.98
- $0.8 < E/P < 1.2$
- $W^2 > 8 \text{ GeV}^2$ (Deep inelastic cut)
- $P > 9 \text{ GeV}/c$.

Other definitions were used for specific background and systematic studies. For example, to obtain a very pure electron sample, the Čerenkov threshold could be

increased to 100 in each detector. This limited the number of detected ‘electrons’, but essentially removed any pion backgrounds. Pure electron samples were used, among other things, for training and testing the neural network, and determining the shower counter energy resolutions. Relatively pure pion samples could be obtained by requiring class two tracks, and limiting the E/P ratio to less than 0.5. Pure pion samples were useful for investigating the pion asymmetry (see section 5.4.1), and training the neural network.

5.4 Asymmetry Corrections

To determine the longitudinal and transverse asymmetries associated with Deep Inelastic electron Scattering (DIS), several background processes had to be accounted for in the data set, and corrections made for additional non-background effects. The backgrounds which impacted the asymmetries were pion contamination, and charge symmetric or ‘positron’ contamination. The additional effects which altered the measured asymmetries from the pure DIS asymmetry desired were the electroweak correction, the dead-time correction, the ^3He correction, and the radiative corrections. Both of the background rates could be measured experimentally, as could the dead-time correction. The other effects, however, required some theoretical input, and were mostly calculated corrections which could not be determined from the data alone.

5.4.1 Pion Asymmetry

By far the largest background in the E154 data was due to pions. In the lowest x -bin the ratio of detected pions to DIS electrons was as high as 20:1. Fortunately, the spectrometer optics, detector systems, and data analysis were designed with the high background pion rate in mind, and were quite good at rejecting pions. Once

all cuts were taken, the number of pions contaminating the electron sample was reduced to a maximum of 3% in the lowest x -bin, and was negligible at larger x .

To deal with this contamination of the DIS electron asymmetry it was important to determine the asymmetry associated with the pions. Any value different from the DIS electron asymmetry either diluted or enhanced the measured DIS electron asymmetry.

By examining a large sample of pions, an asymmetry was formed using Eq. (2.101). It was determined that the pion asymmetry was consistent with zero over the measured x range, so the pion contamination could be treated as a slight dilution of the data in the low- x bins.

5.4.2 Positron Asymmetry

The largest contamination of the detected DIS electrons in the experiment was due to charge symmetric processes resulting in electron-positron pairs, primarily from pair production by high energy bremsstrahlung photons produced in the target. The electrons produced in this fashion were indistinguishable from the DIS electrons, and constituted a background which in the lowest x -bins reached as high as 15% of the number of DIS electrons.

The magnitude of the contamination was measured by reversing the currents in the spectrometer magnets, and counting the positrons. With the currents reversed, the detector signals were due entirely to e^+ with a π^+ background. The π^+ events were distinguished from the e^+ events in the usual way, allowing a good determination of the positron rate, and thus the background rate from non-DIS electrons. The asymmetry for this process was also investigated, and found to be consistent with zero over the measured x range.

In addition to determining the positron rates, the so called ‘positron runs’, where the magnet currents were reversed, were used to determine the pion contamination

rates. These runs were well suited for this measurement because the positron rate was so much smaller than the DIS rate, while the π^+ background rate was very similar to the π^- contamination rate in the DIS data. Thus the π^+ signal to noise ratio was much better in these runs, allowing a much more accurate determination of the overall π^+ rate in the data.

The π^+ rate was found by fitting a function to the E/P curve below 0.8, and extrapolating this function into the usual electron E/P region between 0.8 and 1.2. The contamination in the positron data was then the integral from 0.8 to 1.2 of the extrapolated function.

5.4.3 Dead-Time Corrections

Dead-time refers to the time during which the detector and electronics components are not sensitive to additional data because they are still processing data from a previous event. Because of the high rate environment, every effort was made to reduce these effects as much as possible. Additionally, the highly segmented nature of the detectors minimized the probability of multiple particles hitting the same detector element frequently enough to cause a significant correction. For these reasons the E154 dead-time corrections were negligible.

5.4.4 Electroweak Correction

In addition to virtual photon exchanges between the incident electron and the target nucleus, Z^0 particles may be exchanged (weak neutral current). While this is a very small effect at the relatively low Q^2 of this experiment relative to the Z^0 mass, it becomes noticeable for parity violating experiments. In our case, the parity change occurs between the two relative orientations of beam and target polarizations, specifically, the target polarization pointing *against* or *with* the beam momentum vector. In earlier experiments, the target polarization direction was

switched more frequently, and roughly equal amounts of time were spent in each orientation. However, for E154 there was concern about losing the target polarization during a direction switch, so not only was it not done frequently, but most of the data were taken with the target in the same direction (with the beam).

The electroweak effect modifies the formula in Eq. (2.101) for the asymmetry [89] to

$$A_{||} = \frac{[A_{raw} - P_b A_{EW}]}{f P_b P_t}, \quad (5.21)$$

where P_b (P_t) is the beam (target) polarization, f is the dilution factor, A_{raw} is the raw asymmetry, and A_{EW} is the electroweak asymmetry. To first order A_{EW} may be approximated by

$$A_{EW} \approx -10^{-4} Q^2 \{0.77[1 + 0.44 R_s(x)] + 0.11 Y\}, \quad (5.22)$$

where Y is a kinematical factor defined as

$$Y \equiv \frac{1 - (1 - y)^2}{1 + (1 - y)^2 - y^2 R / (1 + R)}, \quad (5.23)$$

and $y \equiv \nu/E$, $\nu \equiv E - E'$, and R is defined in Eq. (2.39). The factor

$$R_s(x) \equiv \frac{2s(x)}{u(x) + d(x)} \quad (5.24)$$

is a measure of the strange quark content in the nucleon, is not well known. As a rough estimate, $R_s(x > 0.2) = 0$ and $R_s(x < 0.2) = 0.5$ were used to determine A_{EW} , and subsequently in Eq. (5.21).

5.4.5 Radiative Corrections

The deep inelastic cross sections discussed in Chapter 2 were called Born or one-photon exchange cross sections. That was because the only Feynman diagram used to calculate the interaction between the incident electron and the target nucleon

was the one-photon exchange diagram shown in Fig. 2.1. It was argued in Chapter 2 that using only the first term in the perturbative expansion describing the interaction was a good approximation because the next diagram in the expansion was suppressed by a factor of $\alpha_{QED}^2 \approx 137^{-2}$. However, some of these additional diagrams do change the cross sections in significant ways. In particular, if the targets are thick, the incident electron can have many interactions with other atoms both before and after the nuclear scattering event. These interactions are termed ‘external’ radiative corrections. The radiative effects which alter the one-photon exchange interaction at the scattering vertex are called ‘internal’.

In the E154 experiment most of the usual radiative corrections for electron scattering cancelled because an asymmetry was being measured rather than a cross section. The only radiative corrections which alter the asymmetry are spin-dependent corrections. The spin-dependent corrections can be parameterized for the asymmetry directly as [90]

$$A_{Born} = A_{meas} + \Delta A_{RC}, \quad (5.25)$$

where A_{Born} is the asymmetry obtained from the one-photon exchange (Born) cross sections and was defined in Eq. (2.36), A_{meas} is the measured asymmetry of Eq. (2.101), and ΔA_{RC} is the spin-dependent radiative correction, which accounts for all processes, both internal and external, which can alter the asymmetry.

The radiative corrections to the asymmetries, $\Delta A_{\parallel}^{RC}$ and ΔA_{\perp}^{RC} were calculated for E154 using a simple target model and the prescription outlined in reference [91]. In the model, the E154 target cell was split into four regions along the beam axis, each of which had different material thicknesses before and after the scattering volume. There was no reason to segment the target further because the radiative corrections were such a small effect overall, and the systematic errors on the corrections were so large.

Systematic errors dominated the uncertainty on the radiative corrections as can be seen in Tables 5.3. These errors were due to the different models used for the corrections described in reference [91]. A full description of the sources of each error contribution can be obtained from reference [90]. The statistical errors listed in Table 5.3 are the widths of the Gaussian distributions of the corrections resulting from running the radiative correction program many times while varying the measured asymmetry points within a Gaussian distribution defined by the statistical errors on the measured points. The final radiative corrections, with the systematic and statistical errors, are presented in Table 5.3. When these corrections are compared to the A_{\parallel}^n values in Table 5.4, they are seen to be consistently smaller than the statistical uncertainty of A_{\parallel}^n .

Table 5.3. Radiative corrections and errors to both the parallel and perpendicular asymmetries for the two E154 spectrometers. Values in all columns except the first are multiplied by 100.

2.75° Spectrometer					
$\langle x \rangle$	$\Delta A_{\parallel}^{RC}$	syst. error	stat. error	ΔA_{\perp}^{RC}	syst. error
0.017	-0.366	0.132	0.053	0.024	0.151
0.025	-0.308	0.096	0.035	0.014	0.118
0.035	-0.251	0.063	0.023	0.004	0.089
0.049	-0.204	0.035	0.016	-.004	0.101
0.078	-0.157	0.020	0.011	-.009	0.111
0.122	-0.123	0.042	0.007	-.008	0.197
0.173	-0.101	0.058	0.004	-.004	0.220
0.240	-0.079	0.061	0.002	0.002	0.181
0.340	-0.058	0.045	0.002	0.008	0.074
0.424	-0.046	0.027	0.002	0.012	0.024
5.5° Spectrometer					
0.057	-0.328	0.061	0.029	0.018	0.065
0.084	-0.273	0.048	0.022	0.001	0.108
0.123	-0.237	0.080	0.015	-.007	0.236
0.172	-0.214	0.110	0.009	-.006	0.315
0.242	-0.185	0.122	0.005	0.001	0.312
0.342	-0.150	0.105	0.004	0.011	0.168
0.442	-0.123	0.091	0.004	0.019	0.053
0.565	-0.100	0.111	0.004	0.025	0.323

5.5 Systematic Studies

Many systematic studies were performed in order to better understand all the parts of the experiment, and to show that there were no major problems which were unaccounted for. Systematic studies of the beam parameters were discussed in section 5.3.2. Another systematic study involved separating the data into two parts depending on which direction the target polarization was pointing, upstream or downstream. The full asymmetry analysis was performed for each part separately, and the extracted structure functions compared. The results of this study are shown in Fig. 5.6. Within statistical errors, the two measurements agree, indicating that there were few systematic uncertainties correlated with target spin orientation, and that the electroweak correction was handled appropriately.

5.6 Combining Runs

The ^3He asymmetry was measured in each individual run. Since the target polarization varied greatly from run to run, it was important to combine the asymmetry results together rather than the counting rates. The parallel asymmetry was defined in Eq. (2.101). To account for the various corrections described above, Eq. (2.101) must be modified to

$$A_{\parallel}^{^3\text{He}}(x) = \frac{A_{raw}(x) - P_b A_{EW}(x)}{f(x) P_b P_t} + \Delta A_{\parallel}^{RC}(x), \quad (5.26)$$

where A_{raw} is the count rate asymmetry, A_{EW} is the electroweak correction, $\Delta A_{\parallel}^{RC}$ is the radiative correction, f is the dilution factor, P_b is the beam polarization, and P_t is the target polarization.

The ^3He asymmetries from many runs, determined using Eq. (5.26), were combined using a weighted average:

$$\bar{A}(x) = \frac{\sum A_i(x)/\sigma_i^2(x)}{\sum 1/\sigma_i^2(x)}, \quad (5.27)$$

$$\sigma_{\bar{A}}(x) = \sqrt{\frac{1}{\sum 1/\sigma_i^2(x)}}, \quad (5.28)$$

where $\sigma_i(x)$ was the statistical uncertainty associated with the asymmetry measurement.

5.7 The Neutron Structure Functions

To obtain the neutron structure functions, the neutron asymmetries were required. The neutron parallel and perpendicular asymmetries were calculated from the ^3He parallel and perpendicular asymmetries, which were obtained by averaging all the runs together. The conversion was done using the parameterization of Eq. (2.124),

$$A_{^3\text{He}} = 2\frac{F_2^p}{2F_2^p + F_2^n}p_p A_p + \frac{F_2^n}{2F_2^p + F_2^n}p_n A_n. \quad (5.29)$$

The various parameters were defined in Section 2.5. The unpolarized structure functions for the proton and neutron, F_2^p and F_2^n are well known, and parametrized as described in section 2.4. The neutron parallel and perpendicular asymmetries obtained in this fashion were then converted to the $A_1^n(x)$ and $A_2^n(x)$ asymmetries for the neutron using Eqs. (2.46) and (2.47). The experimental results for $A_1^n(x)$ and $A_2^n(x)$ are presented in Table 5.4. The $g_1^n(x)$ and $g_2^n(x)$ structure functions for the neutron were calculated from the neutron A_1 and A_2 asymmetries using Eqs. (2.103) and (2.104). The results of these calculations are presented in Table 5.5, and graphically in Figs. 5.7 and 5.8.

Table 5.4. The neutron A_1 and A_2 asymmetries with statistical and systematic errors for the combined spectrometers at measured Q^2 (assuming no Q^2 dependence).

$\langle x \rangle$	A_1^n	\pm stat	\pm sys	A_2^n	\pm stat	\pm sys
0.017	-0.058	0.019	0.018	0.03	0.07	0.01
0.025	-0.080	0.015	0.014	0.00	0.06	0.01
0.035	-0.078	0.018	0.011	-0.11	0.06	0.01
0.049	-0.086	0.016	0.010	0.10	0.06	0.01
0.081	-0.092	0.013	0.011	0.05	0.05	0.01
0.123	-0.106	0.014	0.012	0.05	0.06	0.02
0.173	-0.092	0.021	0.012	0.02	0.07	0.02
0.242	-0.112	0.028	0.020	0.05	0.12	0.04
0.342	-0.068	0.065	0.025	-0.05	0.24	0.08
0.441	-0.003	0.142	0.022	-0.29	0.50	0.04
0.564	0.100	0.294	0.039	-0.04	0.96	0.06

Table 5.5. The neutron g_1 and g_2 structure functions with statistical and systematic errors for the combined spectrometers at measured Q^2 (assuming no Q^2 dependence).

$\langle x \rangle$	g_1^n	\pm stat	\pm sys	g_2^n	\pm stat	\pm sys
0.017	-0.351	0.115	0.110	7.36	15.74	2.24
0.025	-0.374	0.071	0.065	0.15	7.19	0.98
0.035	-0.290	0.061	0.039	-7.90	4.91	0.96
0.049	-0.204	0.040	0.022	4.60	2.50	0.54
0.081	-0.137	0.021	0.016	1.97	1.12	0.33
0.123	-0.108	0.015	0.012	0.75	0.69	0.22
0.173	-0.061	0.014	0.009	0.19	0.54	0.14
0.242	-0.042	0.011	0.007	0.10	0.32	0.10
0.342	-0.017	0.011	0.005	0.02	0.25	0.09
0.441	-0.007	0.011	0.002	-0.13	0.22	0.02
0.564	0.003	0.008	0.001	-0.01	0.13	0.01

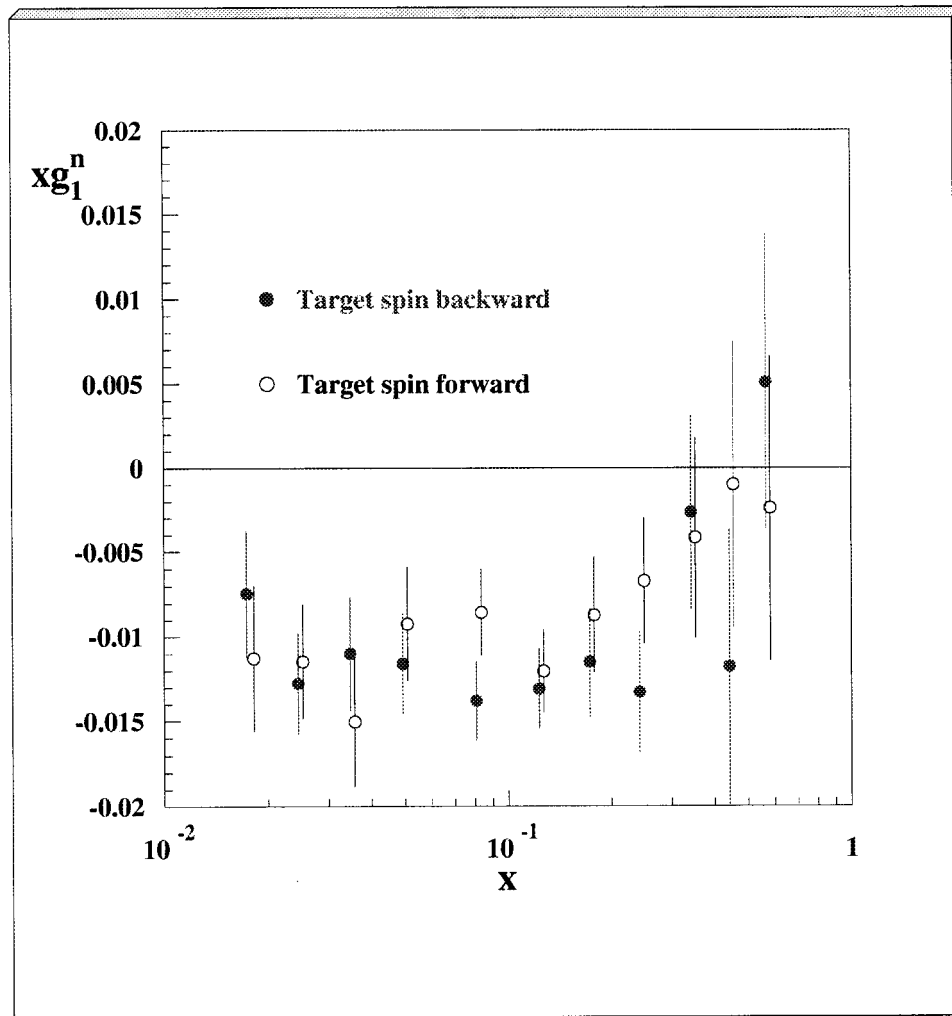


Figure 5.6. The neutron structure function determined from data where the target spin direction was downstream (forward) compared with the same determination from data where the target spin direction was pointing upstream.

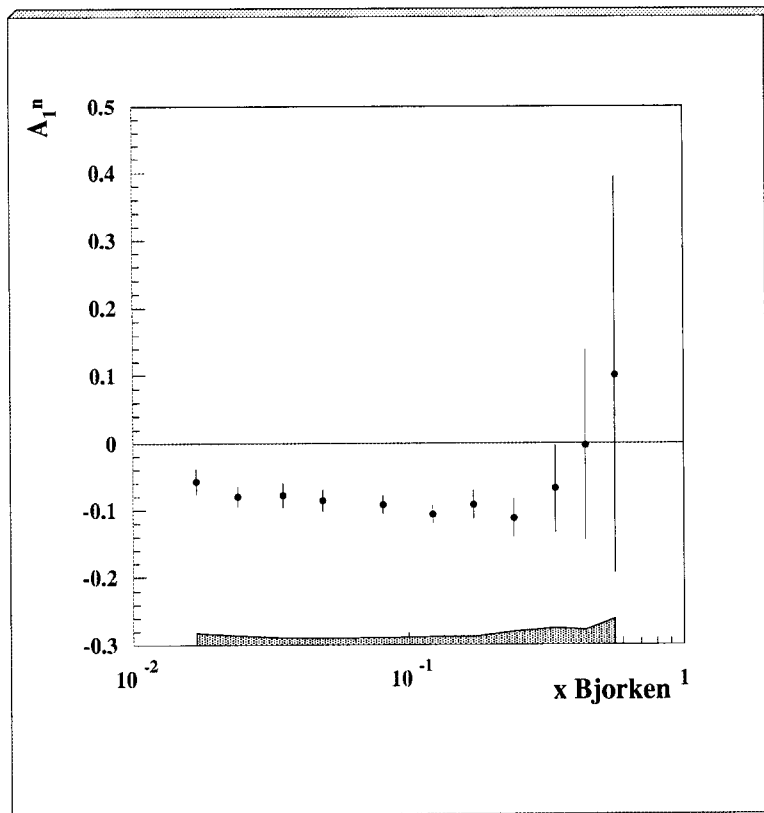


Figure 5.7. The neutron A_1 asymmetry. The error bars are statistical only, and the gray band at the bottom represents the size of the systematic uncertainty.

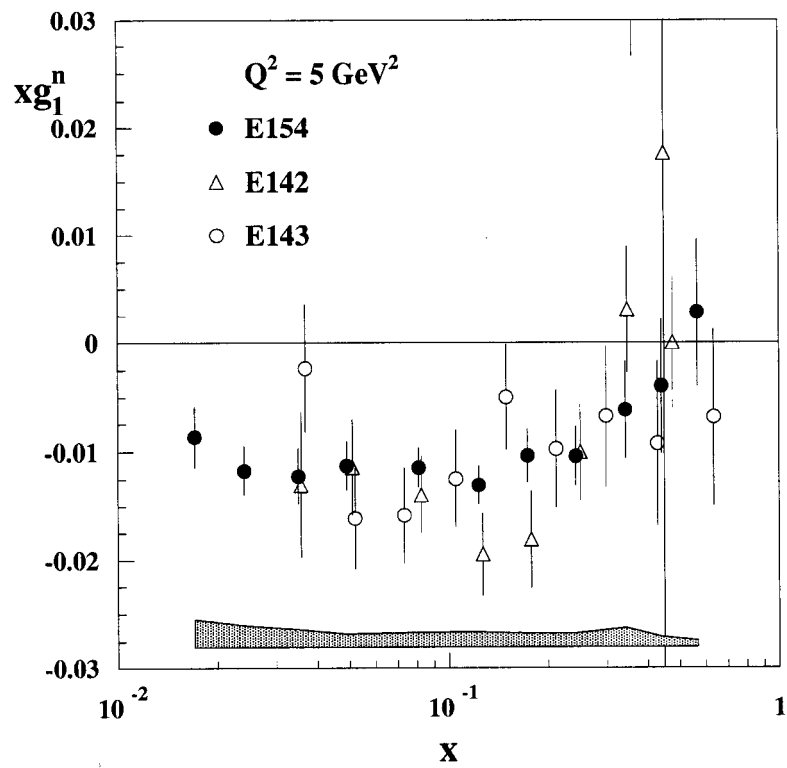


Figure 5.8. The neutron structure function $xg_1(x)$. The error bars are statistical only, and the gray band at the bottom represents the size of the systematic uncertainty.

CHAPTER 6

INTERPRETATIONS

In this chapter, the data resulting from the analysis of the E154 experiment will be compared with some of the theoretical predictions from the quark models of the nucleons. The main sum rule predictions for the polarized nucleon structure functions are the Bjorken [8], the Ellis-Jaffe [9], and the Burkhardt-Cottingham [19] sum rules described in section 2.3. These sum rules relate other experimental observables to integrals over all x of combinations of the structure functions. In order to compare the E154 measurements with these sum rule predictions, two things must be done to the data. First, the data must be evolved to a common value of Q^2 , and second, they must be extrapolated from the measured x range to the low and high x endpoints of 0 and 1.

6.1 Q^2 Evolution

In Chapter 2 an explanation was given for the need to evolve the measured structure function data to a common value of Q^2 , and two procedures were outlined which described how to perform the evolution. For the E154 data, the decision was made to follow the simpler of the two methods, where the ratio g_1^n/F_1^n is assumed to be independent of Q^2 [28]. The measurements in all x -bins were evolved to $Q^2 = 5 \text{ GeV}^2$, which was close to the average $\langle Q^2 \rangle$ of the E154 data set. The measured values of $g_1^n(x)$ evolved to $Q^2 = 5 \text{ GeV}^2$ are presented in Table 6.1. The

Table 6.1. The neutron structure function g_1 with statistical and systematic errors for the combined spectrometers evolved to $Q^2 = 5 \text{ GeV}^2$ assuming g_1^n/F_1^n is independent of Q^2 .

$\langle x \rangle$	g_1^n	$\pm \text{stat}$	$\pm \text{syst}$
0.017	-0.497	0.163	0.155
0.025	-0.481	0.092	0.083
0.035	-0.345	0.073	0.047
0.049	-0.228	0.045	0.025
0.081	-0.139	0.022	0.016
0.123	-0.105	0.014	0.012
0.173	-0.060	0.014	0.009
0.242	-0.043	0.011	0.007
0.342	-0.018	0.013	0.005
0.441	-0.009	0.014	0.003
0.564	0.005	0.012	0.002

$A_2^n(x)$ data were evolved in the same manner, but to a Q^2 value of 3.6 GeV^2 because the average $\langle Q^2 \rangle$ in the A_\perp data set was different from the A_\parallel data set.

The evolved data were then integrated to yield the ‘neutron integral’ over the measured x region:

$$\Gamma_{1_{meas}}^n \equiv \int_{0.014}^{0.7} g_1^n(x) dx = -0.036 \pm 0.004(\text{stat}) \pm 0.005(\text{syst}). \quad (6.1)$$

However, to compare the measured structure function integrals with the sum rule predictions, the contributions from the unmeasured regions,

$$\int_0^{0.014} g_1^n(x) dx, \quad \text{and} \quad \int_{0.7}^1 g_1^n(x) dx \quad (6.2)$$

must be determined.

6.2 The $x \rightarrow 1$ Extrapolation

The asymptotic form of $g_1^n(x \rightarrow 1)$ has been explored by Farrar and Jackson [93], and Brodsky *et al.* [94]. Using basic arguments and quark counting rules, the asymptotic form of the nucleon structure functions at large x is found to be

$$g_1^n(x \rightarrow 1) \sim C(1-x)^3, \quad (6.3)$$

or equivalently,

$$A_1^n(x \rightarrow 1) \sim 1. \quad (6.4)$$

Eq. (6.3) was used on the E154 data to extrapolate the structure function from the measured region to $x = 1$. The evolved $g_1^n(x)$ datum from the highest x bin was used to determine the constant of proportionality, and the function was then integrated to yield

$$\int_{0.7}^1 g_1^n(x) dx = 0.00012 \pm 0.00029 \text{ (stat)} \pm 0.00005 \text{ (syst)} \quad (6.5)$$

as the contribution to the neutron integral from the unmeasured high x region. It is seen to be nearly negligible compared to the measured region of the neutron integral.

6.3 The $x \rightarrow 0$ Extrapolation

In the past, experimental structure function data have always been extrapolated from the measured range to $x = 0$ using Regge theory. The asymptotic form specified by Regge theory is

$$g_1(x \rightarrow 0) \sim \beta x^{-\alpha}, \quad (6.6)$$

with α in the range $-0.5 \leq \alpha \leq 0$ [44]. A fit of this form is shown in Fig. 6.1. Only the three lowest x bins of the E154 data are fit successfully using the Regge form, which means the Regge behavior is not apparent until x is much smaller than the usual $x \sim 0.1$ used in the past for the onset of the Regge form. The Regge fit is also seen to not follow the trend of the SMC data at lower x .

Several authors have proposed other functional forms for the low x region. Bass and Landshoff [95] find a form consistent with the traditional Regge formulation for the iso-triplet contribution, but add a contribution from a two gluon process,

which yields an asymptotic form of

$$g_1^n(x) \sim \left(2 \ln \frac{1}{x} - 1\right). \quad (6.7)$$

Close and Roberts [96] have also investigated the low x behavior of the structure functions, and found another form based on the double log approximation (DLA) of QCD. The form of the structure function at low x in the DLA is

$$g_1^n(x) \sim [F_1]^{\sqrt{2}}. \quad (6.8)$$

Close and Roberts also discussed an asymptotic form obtained using a Pomeron exchange, which predicts the structure function to behave like

$$g_1(x \rightarrow 0) \sim a \ln \left(\frac{1}{x}\right). \quad (6.9)$$

The fact that there is so much disagreement over the asymptotic forms at low x was one of the reasons this experiment was performed, and certainly was the reason for extending the kinematic coverage to include values as low in x as physically possible using the SLAC accelerator.

The evolved E154 g_1^n data from the lowest three x bins were used to find the best fits for each of these additional functional forms. The resulting extrapolations are plotted along with the data in Fig. 6.1. The best fit to the E154 and SMC data is from an unconstrained power law of the form

$$g_1^n(x) \approx C (1/x^\alpha) \quad (6.10)$$

where α is determined to be 0.9 ± 0.2 . However, the integral from 0 to 0.014 of this function diverges when $\alpha=1$, so that no uncertainty can be associated with the integral using the power law form of the extrapolation.

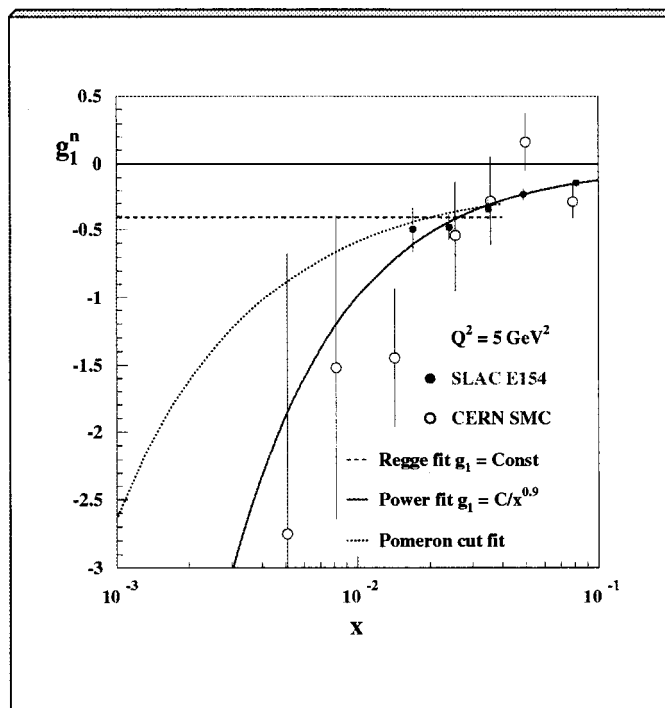


Figure 6.1. The low x extrapolations of the E154 data. Data from the SMC experiments are also plotted to show the trend of the world measurements at lower x .

6.4 Sum Rule Results

Because there is so much theoretical disagreement on the form for the low- x extrapolation, the E154 collaboration decided not to quote a result for the full integral from 0 to 1 of the $g_1^n(x)$ structure function. The published report [97] gives the integral in the measured region, and only estimates the contributions from the high x region.

6.4.1 Comparison to the Ellis-Jaffe Sum Rule

The integral can be compared with the Ellis-Jaffe sum rule prediction (described in section 2.3.2), even though the contribution $\int_0^{0.014} g_1^n(x) dx$ is omitted. This comparison is accomplished by plotting the integral as a function of x as shown in Fig. 6.2. At each value of x , the plot shows the integral from x to 1. This allows

Neutron integral

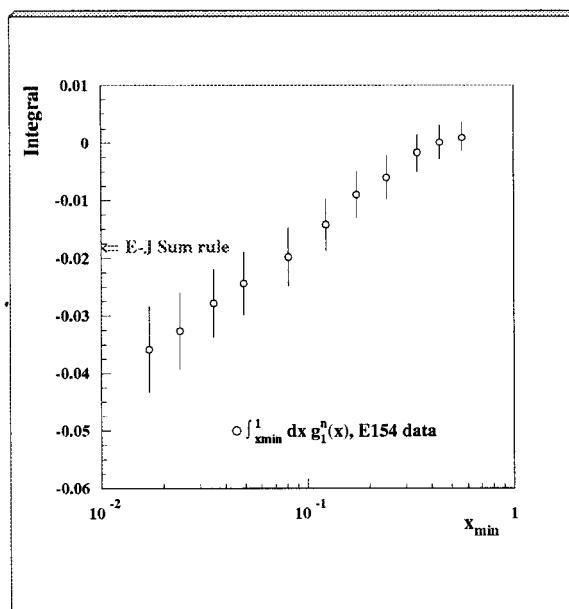


Figure 6.2. The integral of the neutron $g_1^n(x)$ structure function measurements as a function of x . Each plotted value is the integral from x to 1 of the measured data (with the extrapolation to $x = 1$ included).

the trend of the integral to be inferred from the plot. It is quite obvious from this figure that the Ellis-Jaffe sum rule is violated by several standard deviations. Although the extrapolation to low- x is uncertain, none of the asymptotic forms predict a sign change for g_1^n , so there is no way the unmeasured low x region could somehow bring the integral in line with the Ellis-Jaffe prediction. The theoretical prediction shown is for $Q^2 = 5 \text{ GeV}^2$ to match the data, with 3rd order QCD corrections applied (see section 2.3.2).

6.4.2 Comparison to the Bjorken Sum Rule

A comparison with the Bjorken sum rule prediction (described in section 2.3.1) requires knowledge of the proton $g_1^p(x)$ structure function. An average of the E143 [47] and SMC [45] data on the proton was used, again evolved (using g_1/F_1 independent of Q^2) to $Q^2 = 5 \text{ GeV}^2$. A plot similar to the neutron integral of Fig. 6.2 can

Bjorken Sum Rule

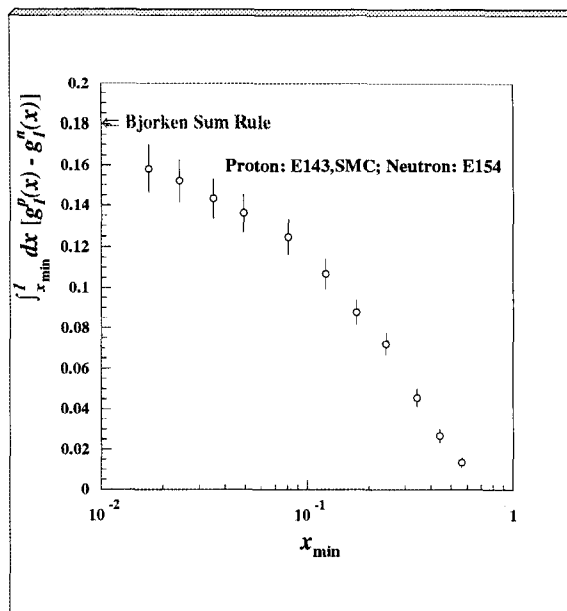


Figure 6.3. The integral of the difference between the neutron $g_1^n(x)$ and the proton $g_1^p(x)$ structure function measurements as a function of x . Each plotted value is the integral from that x to 1 of the measured data (with the extrapolation to $x = 1$ included). The proton data are from SLAC experiment E143, and the CERN SMC experiment for the low x values.

be made, and is shown in Fig. 6.3. It is not clear in this case what interpretations should be drawn from the plot. The integral is tending toward the predicted value, and ends about 10% short at $x=0.014$. It seems plausible that the unmeasured region could account for the deficit. Since the integrand in the Bjorken sum rule is the difference between the proton and the neutron structure functions, the low x extrapolation is less critical than it was for the Ellis-Jaffe sum rule. This is because both nucleons are predicted to have identical asymptotic forms, meaning that the difference will be somewhat independent of the form chosen. Nonetheless, without a definitive extrapolation to $x = 0$ which is supported by the data, the validity of the Bjorken sum rule cannot be stated unequivocally.

6.4.3 Comparison to the Burkhardt-Cottingham Sum Rule

The Burkhardt-Cottingham sum rule prediction may be tested with the E154 measurements of the neutron $g_2^n(x)$ structure function. The $g_2^n(x)$ data were much less precise than the $g_1^n(x)$ data because only a relatively small number of runs were taken with the target polarization in the transverse direction. Because the data are so imprecise it is difficult to draw many conclusions when they are compared to the theoretical predictions. The extrapolation of $x \rightarrow 1$ was done assuming $g_2(x \rightarrow 1) \sim (1 - x)^3$. The integral of the data is

$$\int_{0.014}^1 g_2^n(x) dx = 0.19 \pm 0.17 \text{ (stat)} \pm 0.02 \text{ (syst)}, \quad (6.11)$$

which is in agreement with the Burkhardt-Cottingham prediction of 0.

The $A_2^n(x)$ asymmetry data are plotted in Fig. 6.4 along with the \sqrt{R} positivity restriction described in section 2.3.3. The data are seen to lie well within the \sqrt{R} bounds.

The $g_2^n(x)$ data may also be compared to the parameterization of Wandzura and Wilczek,

$$g_2^{WW}(x) = -g_1(x) + \int_x^1 \frac{dx'}{x'} g_1(x'), \quad (6.12)$$

and found to be not inconsistent as shown in Fig. 6.5. The data deviate from g_2^{WW} between $x \sim 0.03$ and $x \sim 0.1$, but never by more than one standard deviation. The g_2^{WW} calculation in Fig. 6.5 was made using the E154 determination of $g_1^n(x)$.

Little more can be said about the g_2^{WW} parametrization because of the large statistical uncertainties in the measurements.

6.5 Spin Decomposition of the Neutron

The measured Bjorken and Ellis-Jaffe sum rule integrals are usually used to separate the nucleon spin contributions stemming from the different quark flavors.

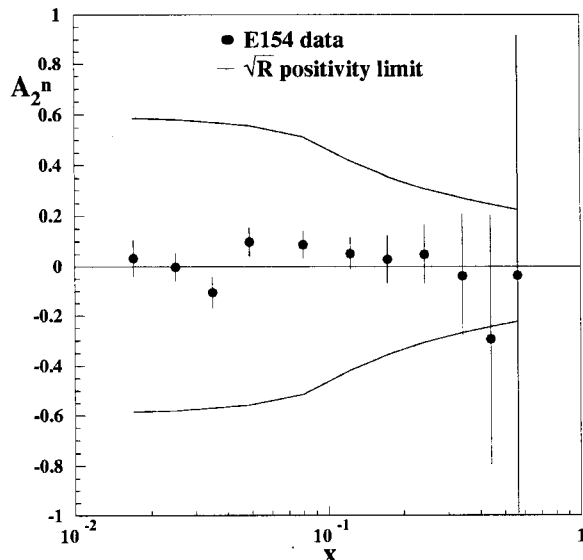


Figure 6.4. The neutron A_2 asymmetry, with the square root of R limit shown as the solid line.

There are two reasons why this was not done with the E154 data. First, because of the inability to accurately extrapolate the structure functions to $x = 0$, the neutron integral is incomplete, and second, the usual spin decomposition in terms of the quark flavor helicity contributions is not a complete set of basis states.

In the naive quark model, described in Section 2.1.5, the decomposition is well defined. However, the naive quark model is not able to account for the overt violation of the Ellis-Jaffe sum rule described in Section 6.4.1. Using the QCD-improved QPM, which allows for finite Q^2 corrections to be made to the sum rules, the gluon helicity contributions to the nucleon spin are nearly irretrievably intertwined with the quark helicity contributions.

6.6 Determining α_s

If the Bjorken sum rule is assumed to be valid, then the measured value of the integral can be used to determine the strong coupling constant, α_s , at the Q^2 of the measurement from the pQCD corrections. This has been done by El-

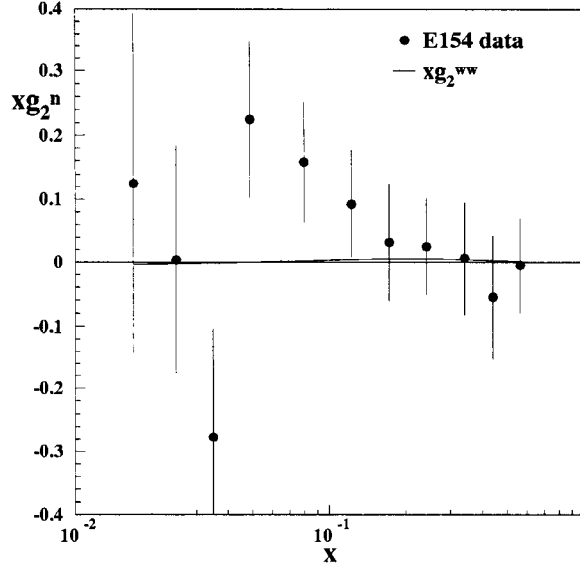


Figure 6.5. The neutron g_2^n structure function data measured in E154. The g_2^{WW} parameterization shown is calculated from the E154 g_1^n data.

lis and Karliner [98], who find $\alpha_s(2.5 \text{ GeV}^2) = 0.375_{-0.081}^{+0.062}$, which corresponds to $\alpha_s(M_Z^2) = 0.122_{-0.009}^{+0.005}$ using SMC and E143 data. This provides a novel technique for measuring the strong coupling constant at much lower Q^2 values than are usually available.

6.7 Conclusions

The data from E154 provided a much better determination of the neutron spin structure functions than was previously available, thus allowing higher precision comparisons to be made with the theoretical predictions of the Bjorken and Ellis-Jaffe sum rules. The Bjorken sum rule was found to be consistent with the data, but the Ellis-Jaffe sum rule prediction is several standard deviations away from the measured integral. Probably the most important discovery in the E154 data was that the usual prescriptions for extrapolating the structure functions to $x = 0$ do not work well.

6.8 The Future

Several other experiments to study the spin structure of the nucleons are either planned, or currently under way. SLAC experiment E155 took data on the proton and the deuteron in the spring of 1997, the results of which are still being analyzed. An extension for E155, called E155x has been approved at SLAC to make a precision measurement of the proton and neutron g_2 structure functions. It is scheduled to take data in early 1999. The sequence of SMC experiments concluded in 1996, although more publications are expected as their data continue to be analyzed. In the meantime the HERMES experiment at DESY has been running for several years now, and more structure function data should be published soon.

The lessons learned from E154 indicate that every attempt should be made in future experiments to measure the low x region as accurately as possible so a clear extrapolation scheme can be determined. This will involve measuring the structure functions with the statistical precision exhibited by the E154 data at much lower values of x than are currently accessible to high luminosity experiments. Such measurements are not likely to be accomplished soon, however, because of the limitations of the existing accelerator facilities. The Next Linear Accelerator, if and when it is built, will be well suited for these measurements by providing a high luminosity electron beam at energies in the 100's of GeV range, which will allow high statistics measurements of the spin structure functions at $x \sim 0.001$ and lower.

Study of spin in the nucleons has improved our understanding of the quark structure of matter. As with any scientific enterprise, when greater knowledge is obtained, more questions are able to be formulated. The field of spin structure physics has exhibited this trait clearly, as the emphasis has shifted from confirming the Bjorken sum rule to the desire to measure the gluon helicity contributions, and to learn about the low x behavior of the structure functions. Because of its ability

to precisely test models, the study of polarization degrees of freedom will continue to play an important role in the future of particle physics and our understanding of the quark structure of matter.

APPENDIX

RUNS USED IN THE ANALYSIS

Table A.2. Runs used for the asymmetry analysis from target DAVE

Target DAVE: runs used									
1329	1330	1331	1332	1333	1334	1335	1336	1337	1338
1339	1340	1341	1342	1343	1344	1345	1346	1347	1348
1351	1352	1353	1375	1377	1378	1379	1380	1381	1382
1383	1384	1385	1386	1387					

Table A.3. Runs used for the asymmetry analysis from target RIKER

Target RIKER: runs used									
1465	1466	1467	1468	1473	1475	1476	1477	1478	1479
1480	1481	1482	1483	1484	1485	1486	1525	1526	1528
1529	1549	1550	1551	1552	1553	1554	1555	1556	1557
1558	1559	1561	1564	1567	1568	1569	1570	1571	1572
1573	1574	1575	1576	1577	1578	1579	1580	1581	1583
1586	1588	1589	1590	1591	1593	1596	1597	1598	1600
1601	1602	1605	1607	1608	1609	1612	1613	1614	1615
1616	1617	1630	1634	1635	1636	1637	1638	1639	1640
1641	1642	1643	1644	1648	1649	1650	1651	1652	1653
1654	1655	1656	1657	1658	1659	1660	1661	1662	1663
1666	1667	1669	1670	1671	1673	1674	1675	1676	1678
1681	1682	1683	1691	1696	1697	1698	1699	1701	1706
1707	1710	1711	1712	1713	1714	1715	1716	1717	1720
1721	1722	1723	1724	1725	1726	1727	1728	1729	1730
1731	1732	1733	1736	1737	1738	1739	1741	1742	1747
1748	1749	1750	1751	1753	1754	1755	1756		

Table A.4. Runs used for the asymmetry analysis from target BOB

Target BOB: runs used									
1825	1826	1829	1831	1834	1835	1836	1837	1838	1839
1840	1841	1842	1843	1844	1849	1850	1851	1852	1853
1854	1863	1864	1865	1866	1867	1868	1869	1870	1871
1872	1873	1874	1875	1877	1878	1881	1882	1883	1884
1885	1886	1891	1892	1893	1894	1895	1896	1897	1898
1899	1902	1903	1904	1906	1907	1908	1909	1912	1913
1914	1926	1927	1933	1935	1937	1938	1939	1940	1941
1944	1945	1946	1947	1948	1954	1955	1956	1957	1958
1959	1960	1961	1962	1963	1968	1969	1970	1971	1972
1973	1977	1978	1979	1980	1981	1984	1985	1986	1987
1988	1991	1992	1993	1994	1995	1996	1997	1998	1999
2000	2003	2004	2005	2006	2007	2008	2009	2010	2011
2014	2015	2016	2017	2018	2019	2020	2021	2022	2023
2026	2027	2028	2029	2030	2031	2032	2033	2034	2037
2038	2039	2040	2041	2042					

Table A.5. Runs used for the asymmetry analysis from target SMC.

Target SMC: runs used									
2070	2071	2072	2073	2079	2080	2081	2082	2086	2093
2096	2097	2098	2099	2100	2101	2107	2108	2110	2111
2112	2113	2114	2115	2121	2125	2126	2130	2131	2132
2133	2134	2135	2136	2137	2138	2139	2140	2141	2142
2145	2146	2147	2148	2149	2150	2151	2152	2153	2154
2157	2158	2159	2160	2161	2162	2163	2164	2165	2166
2169	2170	2171	2172	2173	2174	2177	2178	2179	2180
2181	2185	2186	2187	2188	2189	2190	2191	2192	2193
2194	2195	2196	2202	2203	2204	2205	2206	2210	2212
2213	2214	2215	2216	2217	2218	2219	2220	2221	2222
2223	2226	2227	2228	2229	2230	2231	2233	2234	2235
2236	2237	2244	2246	2247	2248	2249	2250	2252	2253
2254	2255	2256	2257	2258	2259	2260	2261	2262	2272
2273	2274	2276	2277	2278	2288	2289	2290	2291	2292
2293	2294	2295	2296	2297	2298	2299	2302	2303	2304
2305	2306	2307	2308	2309					

Table A.6. Runs used for the asymmetry analysis from target GENERALS.

Target GENERALS: runs used									
2372	2376	2377	2378	2379	2380	2381	2384	2385	2386
2387	2388	2389	2390	2391	2395	2396	2397	2398	2399
2400	2401	2402	2405	2406	2454	2455	2456	2457	2458
2460	2461	2462	2463	2464	2465	2466	2467	2469	2472
2473	2474	2475	2476	2477	2478	2479	2480	2481	2482
2485	2486	2487	2488	2489	2490	2491	2492	2493	2494
2495	2496	2497	2499	2500	2547	2548	2551	2552	2553
2554	2555	2556	2557	2558	2559	2560	2561	2562	2563
2564	2565	2568	2569	2570	2573	2574	2575	2576	2577
2578	2579	2580	2581	2582	2583	2584	2585	2586	2587
2588	2591	2592	2593						

Table A.7. Runs used for the asymmetry analysis from target HERMES.

Target HERMES: runs used									
2649	2650	2651	2652	2653	2655	2658	2659	2660	2661
2662	2663	2664	2665	2666	2667	2668	2671	2672	2673
2674	2675	2676	2677	2682	2683	2684	2685	2686	2687
2688	2689	2690	2691	2692	2693	2697	2698	2699	2700
2701	2703	2704	2705	2706	2707	2708	2712	2713	2714
2715	2716	2717	2720	2721	2722	2725	2726	2727	2728
2729	2730	2731	2732	2733	2734	2735	2736	2737	2741
2742	2743	2744	2745	2746	2747	2748	2749	2750	2751
2754	2755	2756	2757	2758	2759	2760	2761	2762	2763
2764	2765	2766	2767	2771	2772	2773	2774	2775	2776
2777	2778	2779	2780	2781	2784	2785	2786	2787	2788
2789	2790	2791	2792	2793	2795	2798	2799	2800	2801
2802	2803	2805	2806	2807	2808	2809	2810	2811	2812
2813	2814	2815	2816	2819	2820	2824	2825	2826	2827
2828	2829	2830	2831	2832	2833	2834	2840	2841	2842
2843	2844	2845	2846	2847	2848	2849	2852	2853	2854
2855	2856	2857	2858	2859	2860	2861	2862	2866	2867
2868	2869	2870	2871	2872	2873	2874	2875	2876	2879
2880	2881	2882	2883	2884	2885	2886	2887	2888	2889
2890	2891	2892	2896	2897	2898	2899	2900		

Table A.8. Runs used for the asymmetry analysis from target PRELIMS.

Target PRELIMS: runs used									
2936	2937	2938	2939	2940	2941	2942	2943	2946	2947
2948	2949	2950	2951	2952	2955	2956	2957	2958	2959
2960	2961	2962	2965	2966	2967	2968	2969	2970	2971
2972	2975	2976	2977	2979	2980	2981	2982	2983	2984
2985	2986	2990	2992	2993	2994	2995	2996	2997	3000
3001	3002	3003	3004	3005	3006	3007	3010	3011	3012
3013	3014	3015	3016	3017	3020	3022	3023	3024	3026
3027	3028	3029	3030	3031	3032	3033	3034	3035	3038
3039	3040	3041	3042	3043	3044	3045	3046	3051	3052
3053	3054	3055	3056	3057	3058	3062	3063	3064	3065
3066	3067	3068	3069	3073	3074	3075	3076	3077	3078
3079	3080	3084	3085	3087	3088	3089	3091	3092	3093
3094	3095	3096	3097	3098	3099				

Table A.9. Runs used for the asymmetry analysis from target CHANCE.

Target CHANCE: runs used									
3146	3147	3148	3151	3152	3153	3154	3155	3156	3158
3161	3162	3163	3164	3165	3167	3168	3171	3172	3173
3175	3176	3180	3181	3182	3183	3185	3186	3187	3188
3189	3190	3193	3194	3195	3196	3197	3198	3199	3200
3201	3202	3203	3204	3205	3206	3208	3209	3210	3211
3212	3215	3216	3219	3220	3221	3222	3223	3226	3227
3229	3230	3231	3232	3233	3234	3235	3236	3240	3241
3242	3243	3245	3248	3249	3250	3251	3252	3253	3254
3255	3256	3257	3258	3259	3260	3261	3264	3265	3266
3267	3268	3275	3276	3277	3278	3279	3282	3283	3284
3285	3286	3287	3288	3289	3290	3291	3292	3293	3294
3295	3296	3297	3298	3299	3300	3301	3306	3307	3308
3309	3310	3311	3312	3313	3314	3325	3329	3330	3331
3332	3333	3334	3335	3337	3338	3339	3340	3341	3344
3345	3346	3347	3354	3355	3356	3357	3358	3359	3360
3361	3362	3365	3366	3369					

Table A.10. Runs used for the asymmetry analysis from target PICARD.

Target PICARD: runs used									
3460	3463	3464	3465	3466	3467	3468	3469	3470	3474
3475	3476	3477	3482	3483	3484	3485	3486	3487	3488
3489	3490	3491	3492	3493	3496	3497	3498	3499	3500
3501	3502	3503	3504	3505	3506	3507	3511	3512	3513
3514	3515	3516	3517	3518	3519	3520	3521	3522	3523
3524	3525	3526	3527	3530	3531	3532	3533	3534	3535
3536	3537	3540	3541	3542	3543	3544	3545	3547	3548
3549	3550	3551	3552	3553	3554	3555	3556	3557	3558
3561	3562	3563	3564	3567	3568	3569	3570	3571	3572
3573	3576	3577	3578	3579	3580	3581	3582	3583	3587
3588	3589	3590	3591	3592	3593	3594	3595	3596	3599
3600	3601	3602	3603	3604	3605	3606	3607	3608	3609
3610	3611	3612	3613	3614	3615	3616			

Table A.11. Runs used for measuring the positron background with the spectrometer magnet currents reversed. The target was PICARD.

Target PICARD: runs used for positrons									
3425	3426	3427	3428	3429	3430	3431	3433	3434	3435
3436	3440	3441	3442	3443	3444	3445	3446	3447	3448
3682	3683	3684	3685	3686	3687	3688	3689	3690	3691
3692	3693	3694	3695	3696	3699	3700	3701	3702	3703
3704	3705	3706	3709	3710	3711	3712	3713	3714	3715
3716	3717	3721	3722	3723	3724	3725	3726	3727	3728
3731	3732	3733	3734	3735	3736	3737	3740	3741	3742
3743	3744	3745	3746	3747					

Table A.12. Runs used for measuring A_{\perp} . The target was PICARD.

Target PICARD: runs used for A_{\perp}									
3620	3621	3622	3623	3624	3625	3626	3627	3630	3631
3632	3633	3634	3635	3636	3637	3639	3640	3641	3642
3643	3644	3647	3648	3649	3650	3651	3652	3653	3655
3656	3657	3660	3661	3662	3663	3664	3665	3666	3668
3669	3670	3754	3755	3756	3757	3758	3759	3760	3761
3765	3766	3767	3768	3769	3770	3771	3772	3773	3775
3776	3779	3780	3781	3782	3783	3784	3785		

BIBLIOGRAPHY

- [1] Gell-Mann, M., Phys. Lett. **8**, 214 (1965).
- [2] Bjorken, J.D., Phys. Rev. **179**, 1547 (1969);
Feynman, R.P., Phys. Rev. Lett. **23**, 1415 (1969);
Bjorken, J.D. and Paschos, E.A., Phys. Rev. **185**, 1975 (1969).
- [3] Bloom, E.D. *et al.*, Phys. Rev. Lett. **23**, 930 (1969).
- [4] Breidenback, M. *et al.*, Phys. Rev. Lett. **23**, 935 (1969).
- [5] SLAC E80: Alguard, M.J. *et al.*, Phys. Rev. Lett. **37**, 1258 (1976);
Alguard, M.J. *et al.*, Phys. Rev. Lett. **37**, 1261 (1976);
Alguard, M.J. *et al.*, Phys. Rev. Lett. **41**, 70 (1978);
Baum, G. *et al.*, Phys. Rev. Lett., **45**, 2000 (1980).
- [6] SLAC E130: Baum, G. *et al.*, Phys. Rev. Lett. **51**, 1135 (1983).
- [7] EMC: Ashman, J. *et al.*, Phys. Lett. B **206**, 364 (1988);
Ashman, J. *et al.*, Nucl. Phys. **B328**, 1 (1989).
- [8] Bjorken, J.D., Phys. Rev. **148**, 1467 (1966).
- [9] Ellis, J. and Jaffe, R., Phys. Rev. D **9**, 1444 (1974).
- [10] HERMES: Ackerstaff, K. *et al.*, Phys. Lett. B **404**, 383 (1997).
- [11] SMC: Adams, D. *et al.*, Phys. Rev. D **56**, 5330 (1997).
- [12] Particle Data Group: Barnett, R.M. *et al.*, Phys. Rev. D **54**, 1 (1996).
- [13] See for example: Gockeler, M. *et al.*, Nucl. Phys. Proc. Suppl. **49**, 250 (1996).
- [14] See for example section 6.6 of reference [16].
- [15] BCDMS: Argento, A. *et al.*, Phys. Lett. B **120**, 245 (1983); Phys. Lett. B **140**, 142 (1984).
- [16] Frauenfelder, H. and Henley, E.M., *Subatomic Physics; Second Edition*, Prentice-Hall, Inc., Englewood Cliffs, NJ 07632, (1991).
- [17] Aitchison, I.J.R. and Hey, A.J.G., *Gauge Theories in Particle Physics*, Adam Hilger Ltd., Techno House, Redcliffe Way, Bristol BSI 6NX, UK, (1982).

- [18] Gribov, V.N. and Lipatov, L.N., Sov. J. Nucl. Phys. **15**, 438 (1972); 675 (1972); Dokshitzer, Yu.L., Sov. Phys. JETP **46**, 461 (1977); Altarelli, G. and Parisi, G., Nucl. Phys. **B126**, 298 (1977).
- [19] Burkhardt, H., and Cottingham, W.N., Ann. Phys. **56**, 453 (1970).
- [20] Griffiths, D., *Introduction to Elementary Particles*, Harper & Row Publishers, Inc., 10 East 53rd St., New York, NY 10022-5299, (1987).
- [21] Pussieux, T. and Windmolders, R., DAPNIA-SPHN-95-10.
- [22] Halzen, F. and Martin, A., *Quarks and Leptons: An Introductory Course in Modern Particle Physics*, John Wiley & Sons, Inc. (1984).
- [23] Hey, A.J.G. and Mandula, J.E., Phys. Rev. D **5** 2610 (1972).
- [24] Hughes, V.W. and Kuti, J., Ann. Rev. Nucl. Sci. **33**, 611 (1983).
- [25] See for example: Shankar, R., *Principles of Quantum Mechanics*, Plenum Press, 233 Spring St., New York, NY 10013 (1980).
- [26] Kaur, J., Nucl. Phys. **B128**, 219 (1977); appendix B.
- [27] Feynman, R.P., *Photon Hadron Interactions*, W.A. Benjamin, Inc., Reading, MA (1972).
- [28] E143: Abe, K. *et al.*, Phys. Lett. B **364**, 61 (1995).
- [29] SMC: Adams, D. *et al.*, Phys. Lett. B **396**, 338 (1997); hep-ex/9702005.
- [30] E154: Abe, K. *et al.*, Phys. Lett. B **405**, 180 (1997).
- [31] The Particle Data Group, Phys. Lett. B **239**, 1 (1990).
- [32] Larin, S.A. and Vermaseren, J.A.M., Phys. Lett. B **259**, 345 (1991).
- [33] Kataev, A.L. and Starshenko, V.V., hep-ph/9405294.
- [34] Close, F.E. and Roberts, R.G., Phys. Lett. B **316**, 165 (1993).
- [35] Larin, S.A., Phys. Lett. B **334**, 192 (1994); Larin, S.A., van Ritbergen, T., and Vermaseren, J.A.M., Phys. Lett. B **404**, 153 (1997).
- [36] Wandzura, S. and Wilczek, F., Phys. Lett. B **72**, 195 (1977).
- [37] Song, X., Phys. Rev. D **54**, 1955 (1996).
- [38] Cortes, J.L., Pire, B., and Ralston, J.P., Z. Phys. C **55**, 409 (1992).
- [39] Doncel, M.G. and de Rafael, E., Nuovo Cimento **4A**, 363 (1971).
- [40] Whitlow, L.W. *et al.*, Phys. Lett. B **250**, 193 (1990).
- [41] Whitlow, L.W. *et al.*, Phys. Lett. B **282**, 475 (1992).

- [42] NMC: Amaudruz, P. *et al.*, Phys. Lett. B **295**, 159 (1992).
- [43] NMC: Arneodo, M. *et al.*, Phys. Lett. B **364**, 107 (1995).
- [44] Ellis, J. and Karliner, M., Phys. Lett. B **213**, 73 (1988).
- [45] SMC: Adeva, B. *et al.*, Phys. Lett. B **302**, 533 (1993);
 Adeva, B. *et al.*, Phys. Lett. B **320**, 400 (1994);
 Adams, D. *et al.*, Phys. Lett. B **329**, 399 (1994);
 Adams, D. *et al.*, Phys. Lett. B **336**, 125 (1994);
 Adams, D. *et al.*, Phys. Lett. B **357**, 248 (1995);
 Adeva, B. *et al.*, Phys. Lett. B **369**, 93 (1996);
 Adams, D. *et al.*, Phys. Lett. B **396**, 338 (1997);
 Adams, D. *et al.*, Phys. Rev. D **56**, 5330 (1997).
- [46] SLAC E142: Anthony, P.L. *et al.*, Phys. Rev. Lett. **71**, 959 (1993);
 Anthony, P.L. *et al.*, Phys. Rev. D **54**, 6620 (1996).
- [47] SLAC E143: Abe, K. *et al.*, Phys. Rev. Lett. **74**, 346 (1995);
 Abe, K. *et al.*, Phys. Rev. Lett. **75**, 25 (1995);
 Abe, K. *et al.*, Phys. Lett. B **364**, 61 (1995);
 Abe, K. *et al.*, SLAC-PUB-7242 (1996);
 Abe, K. *et al.*, Phys. Rev. Lett. **76**, 587 (1996).
- [48] Kawall, D.M., Ph.D. Thesis, Stanford University, Stanford, CA (1995).
- [49] Friar, J.L. *et al.*, Phys. Rev. C **42**, 2310 (1990).
- [50] Ciofi degli Atti, C. *et al.*, Phys. Rev. C **48**, R968 (1993).
- [51] Maruyama, T. *et al.*, Phys. Rev. B **46**, 4261 (1992).
- [52] Alley, R. *et al.*, Nucl. Instrum. Meth. A **365**, 1 (1995).
- [53] Young, C., E143 Technical Note #96, unpublished.
- [54] Neal, R.B., *The Stanford Two-Mile Accelerator*, Benjamin, New York (1968).
- [55] Farkas, D. *et al.*, SLAC-PUB 1453 (1974).
- [56] Decker, F.J. *et al.*, SLAC-PUB-7214 (1996).
- [57] Dupen, D.W., SLAC-62 (1966).
- [58] Wiedemann, H., *Particle Accelerator Physics*, Springer-Verlag (1993); Jackson, J.D., *Classical Electrodynamics*, John Wiley & Sons, Inc., New York, NY (1975); Eqs. 14.31 and 32.
- [59] Erickson, R. *et al.*, SLAC-PUB-5891 (1992).
- [60] Brown, K.L. *et al.*, *TRANSPORT Manual* SLAC-91, Rev. 2 (1977).
- [61] Carey, D.C. *et al.*, *TURTLE Manual* SLAC-246 (1982).

- [62] Stuart, L., E154 Technical Note #6, unpublished.
- [63] Mitchell, G. *et al.*, E154 Technical Note #40, unpublished.
- [64] Mitchell, G. *et al.*, E154 Technical Note #39, unpublished.
- [65] Vacuumschmelze GMBH, Hanau, Germany.
- [66] *CRC Handbook of Chemistry and Physics: 68th Edition* The Chemical Rubber Co. press, inc., Boca Raton, FL (1988).
- [67] Scott, G.G., *Rev. Mod. Phys.* **34**, 102 (1964).
- [68] E143 Technical Note #65, unpublished.
- [69] Scott, G.G. and Sturmer, H.W., *Phys. Rev.* **184**, 184 (1969).
- [70] Happer, W., *Rev. Mod. Phys.* **44**, 169 (1972).
- [71] Romalis, M. and Smith, T.B., E154 Technical Note #47, unpublished.
- [72] Smirnov, G.I., *Phys. Lett. B* **364**, 87 (1995).
- [73] Mo, L.W. and Tsai, Y.S., *Rev. Mod. Phys.* **41**, 205 (1969).
- [74] Zyla, P. and Averett, T.D., E154 Technical Note #43, unpublished.
- [75] Jackson, J.D., *Classical Electrodynamics*, John Wiley & Sons, Inc., New York, NY (1975).
- [76] Fernow, R.C., *Introduction to Experimental Particle Physics*, Cambridge Univ. Press (1986).
- [77] Anthony, P.L. and Zsalata, Z.M., SLAC-PUB-7201, 1996.
- [78] Kolomensky, Y., Ph.D. Thesis, University of Massachusetts, Amherst (1997).
- [79] Romalis, M., Ph.D. Thesis, Princeton University (1997).
- [80] Young, C., E154 Technical Notes #50 and #51, unpublished.
- [81] E154 Collaboration Meeting, Mar. 8, 1996, unpublished.
- [82] Reyna, D., Private Communication.
- [83] Young, C., E154 Technical Note #20, unpublished.
- [84] Incerti, S., E154 Technical Note #22, unpublished.
- [85] Staley, F., E154 Technical Note #19, unpublished.
- [86] Incerti, S., E154 Technical Note #30, unpublished.
- [87] Kolomensky, Y., E154 Technical Note #53, unpublished.

- [88] Kolomensky, Y., Olson, M., and Zyla, P., E154 Technical Note #55, unpublished.
- [89] Bosted, P.E., E154 Technical Note #29, unpublished.
- [90] Reyna, D., E154 Technical Note #52, unpublished.
- [91] Kukhto, T.V. and Shumeiko, N.M., Nucl. Phys. **B129**, 412 (1983).
- [92] Bevington, P.R., *Data Reduction and Error Analysis for the Physical Sciences*, McGraw-Hill, (1969).
- [93] Farrar, G.R. and Jackson, D.R., Phys. Rev. Lett. **35**, 1416 (1975).
- [94] Brodsky, S.J., Burkardt, M., and Schmidt, I., Nucl. Phys. **B441**, 197 (1995).
- [95] Bass, S.D. and Landshoff, P.V., Phys. Lett. B **336**, 537 (1994).
- [96] Close, F.E. and Roberts, R.G., Phys. Lett. B **336**, 257 (1994).
- [97] Abe, K. *et al.*, Phys. Rev. Lett. **79**, 26 (1997).
- [98] Ellis, J. and Karliner, M., Phys. Lett. B **341**, 397 (1995).